THE ANNALS OF DUNAREA DE JOS UNIVERSITY OF GALATI

Fascicle IX
METALLURGY AND MATERIALS SCIENCE

GUP

2011

Table of Content

CONTINUOUS FLUX THERMAL TREATMENTS FOR IMPROVING THE RESISTANCE AT ALTERNATE BENDING OF MEDIUM TO HIGH STRENGTH STEEL STRIPS

**Tiberiu Florian POTECAŞU[1], Octavian POTECAŞU[1],
Petrică ALEXANDRU[1], Francisco Manuel BRAZ FERNANDES[2],
Rui Jorge CORDEIRO SILVA[2]**

[1]Center of Nanostructures and Functional Materials, "Dunărea de Jos" University of Galaţi
[2]CENIMAT/Materials Science Department, Nova University of Lisbon, Caparica, Portugal
email: tpotecasu@gmail.com, opotec@ugal.ro

ABSTRACT

The research was focused on obtaining medium to high strength steel strips for strapping heavy products by applying continuous flux thermal treatments on common grades, cheap carbon steels. For steel strapping the behavior at alternate bending is an important issue, thus an objective of the research was to make sure that the treated products withstand a critical number of alternate bending cycles and further more an improvement of the resistance at alternate bending by applying thermal treatments in continuous flux was pursued.

The paper presents the results of the alternate bending test, SEM fractographs, optical analysis of the fracture surface and surface of the strip in the vicinity of the fracture surface after breaking by alternate bending using a stereo-microscope and optical analysis on etched and un-etched samples in transversal section along the rolling direction in the vicinity of the fracture surface using a metallographic optical microscope; for the following samples: the raw material in strain-hardened state, samples subjected to continuous flux quenching from 900°C and tempering by passing through the furnace maintained at 600°C, and samples subjected to quenching from 900°C and tempering by passing through the furnace maintained at 700°C.

KEYWORDS: carbon steel strips, continuous flux thermal treatments, resistance at alternate bending

1. Introduction

The research was focused on producing steel strips for strapping made from common carbon steels with improved mechanical characteristics by means of thermal treatments.

A good resistance at alternate bending is very important for steel strapping because in practice there are cases where, during transportation of the strapped cargo, as a consequence of stacking and poor road conditions, the strip can have a sliding motion around corners subjecting the material to alternate bending.

In this respect in this paper there are presented the effects on the resistance at alternate bending of the continuous flux thermal treatment of quenching from 900°C and tempering at 600°C for one minute and also of the continuous flux thermal treatment of quenching from 900°C and tempering at 700°C for one minute.

2. The raw material

The chemical composition of the steel used as raw material in the experiments is presented in Table 1.

Table 1. *Chemical composition of the steel used as raw material, [wt%]*

C	Si	**Mn**	P	S	Al	As	Ti
0.185	0.063	**1.350**	0.023	0.008	0.050	0.043	0.005
V	Cu	Ni	Cr	Mo	Nb	B	
0.001	0.012	0.027	0.031	0.002	0.001	0.0001	

The steel is cold-rolled with a thickness of 0.8 mm and cut in strips of 19 mm in width. The results of the tensile strength test done on raw material samples labeled B.0 are presented in Table 2. The samples were not machined for the tensile strength test because of their intended use as steel strapping; the values represent the average of three valid tests (broken in the mid-range of the sample between the grips).

Table 2. *Tensile strength test results for the raw material*

Sample	Section [mm x mm]	Rm [MPa]	A_{prop} [%]	A_{80mm} [%]
B.0	0.8 x 19	820	12	8

The Vickers micro-hardness, determined using the 500g weight, of the B.0 raw material samples is 275 HV – the value represents the average value resulting from 8 valid imprints.

At alternate bending at 90° in both directions over a 3 mm radius, the first visible cracks are observed after bending for 6 times and failure takes place after bending for 7 times. The images done with a stereomicroscope on B.0 raw material samples after breaking by alternate bending are presented in Figure 1 and Figure 2. In Figure 1, from the analysis of the aspect of the fracture surface it can be seen that cracks parallel to the surface of the strip with length in the fracture surface of 1 to 2 mm were formed, these are deep and wide, and are present along the whole width of the strip. These cracks do not necessary form a continuous network, but are present especially in the central area (thickness wise). The probable cause that leads to their formation is the strain hardened state of the material, and the presence of non-metallic inclusions flattened during the rolling process; the intergranular interfaces from the plastically deformed metallic mass, or the interfaces between metallic matrix and inclusions present a low degree of coherence and thus shear stress concentrators form with catastrophic effects. Regarding the aspect of the fracture surface towards the surface of the strip there can be seen areas with crystalline-shine aspect that suggest fragile breaking and also round-shape specific reflections that suggest ductile breaking.

a)
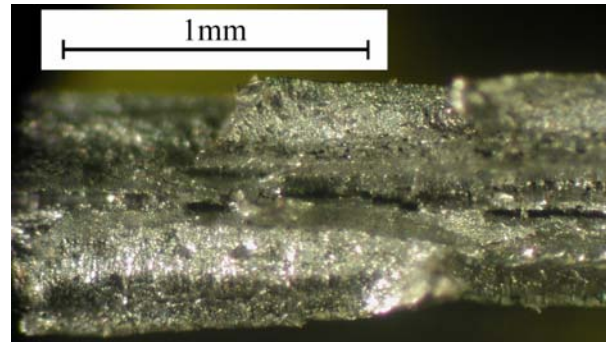
b)

Fig. 1. *The aspect of the fracture surface after breaking by alternate bending specific for type B.0 raw material samples. The images have been taken with a stereomicroscope; b) represents a detail from a).*

From Figure 2, it can be seen that the surface of the strip shows that important deformations took place at a microscopic level in all the bending affected region, not only in the immediate vicinity of the fracture surface.

Thus it is put into evidence the appearance of some oblique upsetting lines at an angle of approximately 7.5° from the normal to the edge of the strip. These lines have formed as a result of the stretching-compression cycles of the material from the surface of the strip.

The upsetting lines have lengths between 2 and 4.5 mm and are more clearly seen in areas with the shape of bands perpendicular to the edge of the strip; observations that suggest the concentration of the deformation forces in these areas. Even more, in the case of some of these horizontal bands cracks can be seen between adjacent upsetting lines. At a distance of approximately 5mm from the fracture surface another area can be observed where a partial fracture took place. Both of these fracture lines (the catastrophic fracture and the partial fracture) were formed by the coalescence of adjacent cracks developed between the upsetting lines.

The fracture line is irregular showing areas where the material detached between two oblique upsetting lines and got curved from the action of the stretching forces from the surface of the material prior to the catastrophic fracture, suggesting that, during the fracture process, important plastic deformations took place simultaneously with the formation of a great number of independent cracks. In this way, critical sections were created with a role of tension concentrators that ultimately lead to catastrophic failure.

a)

b)
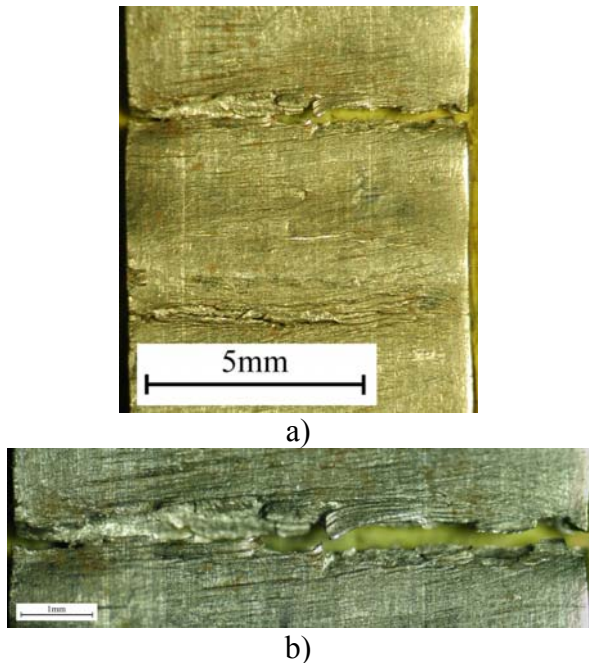
Fig. 2. The aspect of the surface of the strips after breaking by alternate bending, specific for type B.0 raw material samples. The images have been taken with a stereomicroscope; b) represents a detail from a).

In Figure 3, SEM details of the fracture surface are presented taken from an area close to the right edge of the fracture surface. The detail taken at x100 magnification covers the whole thickness of the steel strip.
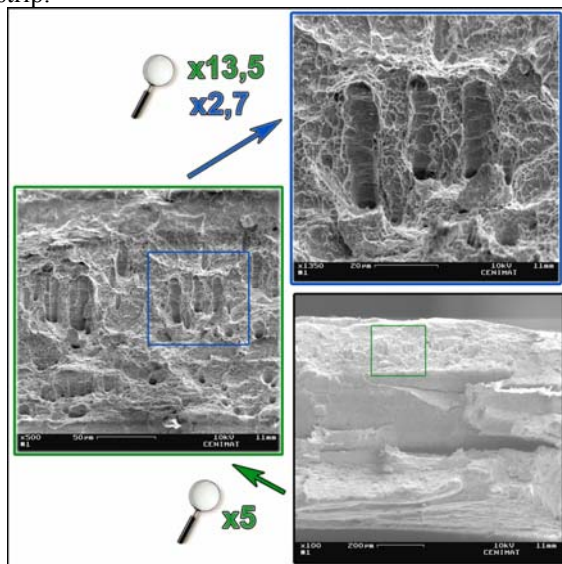
Fig. 3. The specific aspect of some details of the breaking surface after breaking by alternate bending for type B.0 raw material samples. Images taken with SEM.

As it was put into evidence in the pictures taken with the stereo-microscope, it can be seen that the fracture presents different aspects along the thickness of the strip. Thus, as also seen in the details taken at higher magnifications, in the upper part, the fracture surface presents characteristics specific for dimple rupture – these dimples are very shallow towards the surface of the strip indicating a mostly fragile rupture, towards the center, the dimples get more pronounced and are circular in shape indicating a mostly ductile rupture. On the surface of the strip areas indicating decohesive rupture at the interface between inclusions and the metallic matrix are also present – these are shaped as channels longitudinally oriented.

In Figure 4, a microstructure is presented realized on longitudinal section in the vicinity of the fracture section; the sample was not etched and the optical magnification was x200.
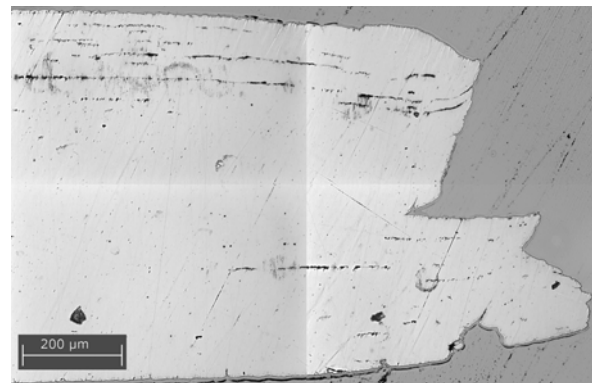
Fig. 4. Microstructure done in longitudinal section on the lamination direction, from the area adjacent to the fracture surface after breaking by alternate bending; microstructure characteristic for type B.0 raw material samples. The image was done on unattached sample by digital composition of 4 adjacent photos taken at x200 optical magnification.

Two interesting aspects can be observed in the image. Firstly, the presence of dark lines with a thickness of approximately 7-8 μm, parallel to the surface of the strip is observed. The study of the inclusions arranged in lines on samples not subjected to alternate bending showed that they have a thickness between 0.5 to 2 μm, exceptionally isolated polygonal formations can be observed that can go up to 4-5 μm. Thus it can be concluded that as a result of the alternate bending these lines are "thickened". In fact this "thickening" is the effect of the decohesive rupture that takes place at the interface between the inclusion lines and the metallic matrix. Secondly, the role of these longitudinal cracks in joining transversal cracks with catastrophic consequences is observed

from the contour of the fracture surface in this section.

3. The continuous flux thermal treatment installation

For the experiments, a laboratory installation was designed and built in order to apply continuous flux thermal treatments on the steel strips. The installation is presented in Figure 5 in a schematic representation showing its functional blocks, their placement and inter-relations.

The laboratory installation was connected to a computerized control and measurement system. The parameters that were subjected to computerized control were:

- temperature of the austenitizing furnace;
- the speed of the steel strip through the system;
- the temperature and pressure of the cooling water;

Also a device was used to set and maintain at a constant value the flow of the protection gas fed into the muffle of the austenitizing furnace.
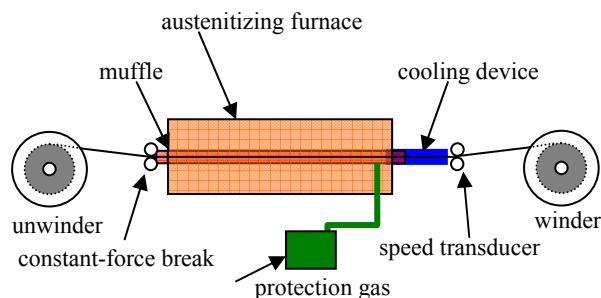
Fig. 5. *Schematic representation of the laboratory installation used for experimental research of continuous flux thermal treatments of steel strips.*

4. Experimental results

4.1. Continuous flux quenching from 900°C and tempering for one minute at 600°C

4.1.1. Presentation of the thermal treatment

The type B.1 samples were subjected to continuous flux quenching thermal treatment by heating for complete austenitization in the furnace maintained at 900°C. The steel strips' speed was maintained at 2 m/min which means that a finite section of steel strip passing through the furnace will be kept at the furnace's temperature for one minute.

The cooling for quenching was done by water jets at room temperature (20°C) and constant pressure.

After quenching, also in continuous flux the steel strip was subjected to the tempering thermal

treatment by passing through the furnace maintained at 600°C. The steel strips' speed, as the treatment was applied in continuous flux, was also of 2 m/min, thus the duration that a finite section of steel strip is maintained at the furnace's temperature is also of one minute. After the exit from the tempering furnace the steel strip was cooled with water showers.

In Figure 6 it is presented the result of the simulation which shows the variation of the temperature for a finite section of steel strip with the section of 0.8x19 mm while passing through the tempering furnace maintained at 600°C. In the figure, markers were introduced at 33 seconds when the temperature of the steel strip is estimated at 402°C and at the exit from the tempering furnace, at 60 seconds when the steel strip's temperature is estimated at 563°C.
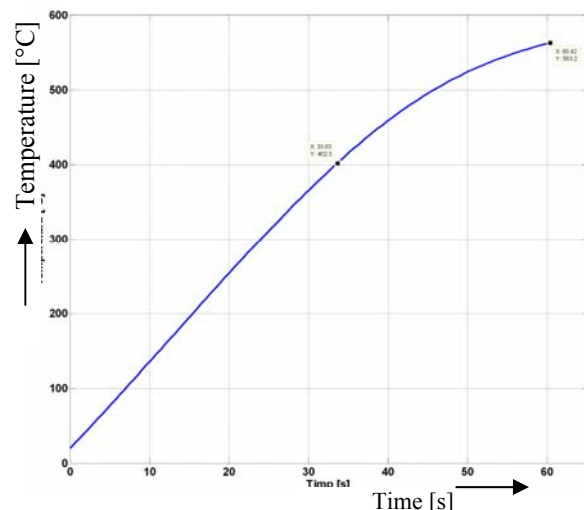
Fig. 6. *Simulation that shows the evolution of the temperature inside the steel strip as a function of time during the tempering of 0.8x19mm steel strip inside the furnace maintained at 600°C for one minute – type B.1 samples. Markers at: 33s-402°C and 60s-563°C.*

4.1.2. Mechanical properties

The results of the tensile strength test are presented in Table 3.

Table 3. *The tensile strength results for the samples treated by continuous flux quenching from 900°C and tempering at 600°C*

Sample type	Section [mm x mm]	Rm [MPa]	A_{prop} [%]	A_{80mm} [%]
B.1	0.8 x 19	814	16.4	10.6

It can be seen that the tensile strength is comparable to that of the raw material, but the breaking elongation is improved by 32.5%.

The Vickers micro-hardness, determined using the 500g weight, of the B.1 samples is 293 HV – the value represents the average result from 8 valid imprints.

4.1.3. Resistance at alternate bending

At alternate bending, the first cracks are observed after bending for 6 times and failure takes place after bending for 7 times. The results are the same with the ones obtained for the type B.0 raw material samples, even though the breaking elongation is significantly improved.

Fig. 7. *The aspect of the breaking surface after breaking by alternate bending specific for type B.1 samples subjected to quenching from 900°C and tempered for one minute in the furnace maintained at 600°C. The images have been taken with a stereomicroscope.*

The aspect of the fracture surface after breaking by alternate bending is presented in Figure 7. From the images it can be seen that the relief of the fracture surface has a preferential orientation parallel to the surface of the strip.

The way the light is reflected from the fracture surface is specific for light reflection from curved surfaces indicating a ductile fracture. Also some small conical craters are observed that indicate a local ductile rupture of cone-cup type.

Having dimensions larger than these craters, on the median area on the whole width of the strip, dark areas with a slightly rectangular shape can be noticed; these are arranged in rows, sometimes linked together by finer cracks reaching lengths of approximately 0.2 mm.

By their shape and distribution, these cracks indicate that they formed at the interface between inclusions and the metallic matrix during the alternate bending cycles, possibly contributing to the ultimate failure.

The relief on an overall view is irregular and presents shapes that indicate a flow of material, the rupture was mainly ductile.

Fig. 8. *The aspect of the surface of the strips after breaking by alternate bending, specific for type B.1 samples subjected to quenching from 900°C and tempered for one minute in the furnace maintained at 600°C. The images have been taken with a stereomicroscope.*

In Figure 8 the aspect of the surface of the steel strip in the vicinity of the fracture line after breaking by alternate bending is presented. In the images, it can be noticed that on the surface of the strip upsetting lines have formed as a result of the stretching-compression cycles of the material from the surface during the alternate bending. These upsetting lines are parallel to the fracture line. Also some finer upsetting lines can be observed; these later lines are inclined at approximately 14° from the normal to the edge of the strip. In the immediate vicinity of the fracture line cracks can be noticed between adjacent upsetting lines. Also, this kind of cracks formed between upsetting lines parallel to the fracture line, but much finer, can also be noticed in another area at approximately 4 mm in the rolling direction, relatively centered to the width of the strip. In the image showing the detail of the fracture surface it can be noticed how the material from the surface of the strip has some twisted and stretched prominences on both sides of the fracture line that indicate that the rupture has taken place by the propagation in profundity of some individual cracks, relatively aligned, starting from the surface of the strip, propagation that had the effect of concentrating the deformation tensions in the sections of material between these cracks, leading implicitly to the catastrophic failure, ductile by overload.

4.2. Continuous flux quenching from 900°C and tempering for one minute at 700°C

4.2.1. Presentation of the thermal treatment

The type B.2 samples were subjected to continuous flux quenching thermal treatment by

heating for complete austenitization in the furnace maintained at 900°C. The steel strips' speed was maintained at 2 m/min which means that a finite section of steel strip passing through the furnace is kept at the furnace's temperature for one minute.

The cooling for quenching was done by water jets at room temperature (20°C) and constant pressure.

After quenching, also in continuous flux the steel strip was subjected to the tempering thermal treatment by passing through the furnace maintained at 700°C. The steel strips' speed, as the treatment was applied in continuous flux, was also 2 m/min, thus the duration that a finite section of steel strip is maintained at the furnace's temperature is also one minute. After the exit from the tempering furnace the steel strip was cooled with water showers. In Figure 9 it is presented the result of the simulation which shows the variation of the temperature for a finite section of steel strip with the section of 0.8x19 mm while passing through the tempering furnace maintained at 700°C. In the figure, markers were introduced at 22s-404°C, 36s-602°C and at the exit from the tempering furnace: 60s-690°C. It can be seen that the radiative heat transfer gets more intense as the temperature of the steel strip at the exit is getting closer to the temperature of the furnace.
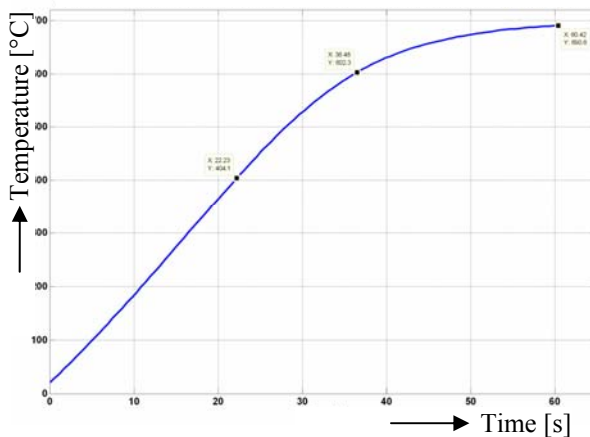
Fig. 9. Simulation that shows the evolution of the temperature inside the steel strip as a function of time during the tempering of the 0.8x19mm steel strip inside the furnace maintained at 700°C for one minute – type B.2 samples. Markers at: 22s-404°C, 36s-602°C, 60s-690°C.

4.2.2. Mechanical properties

The results of the tensile strength test are presented in Table 4.

Table 4: The tensile strength results for the samples treated by continuous flux quenching from 900°C and tempering at 700°C

Sample type	Section [mm x mm]	Rm [MPa]	A$_{prop}$ [%]	A$_{80mm}$ [%]
B.1.5	0.8 x 19	700	21.5	14.3

It can be seen that the tensile strength is reduced by 14% compared to that of the raw material, but the breaking elongation is improved by 78.8%.

The Vickers micro-hardness, determined using the 500g weight, of the B.2 samples is 235 HV – the value represents the average result from 8 valid imprints.

4.2.3. Resistance at alternate bending

At alternate bending, the first cracks are observed after bending for 8 times, and failure takes place after 11 alternate bending cycles.

In Figure 10 there are presented images taken with a stereomicroscope from the fracture surface after breaking by alternate bending. From the images it can be seen that the relief of the fracture surface is irregular, the height variations of the topographical formations are generally smooth and small. The way the light is reflected from the fracture surface indicates that the fracture surface is made out of small rounded surfaces which indicates that a flow of material took place, thus the rupture was mostly ductile. On the surface black dots are observed, especially in the median area from the thickness of the strip; these are of two different types. There are some small craters with circular shape suggesting a cone-cup ductile rupture and some dark areas with a slightly rectangular contour that suggests the presence of a crack parallel with the surface of the strip – these latter ones are sometimes grouped, forming cracks with lengths of 0.1 mm to 0.2 mm.
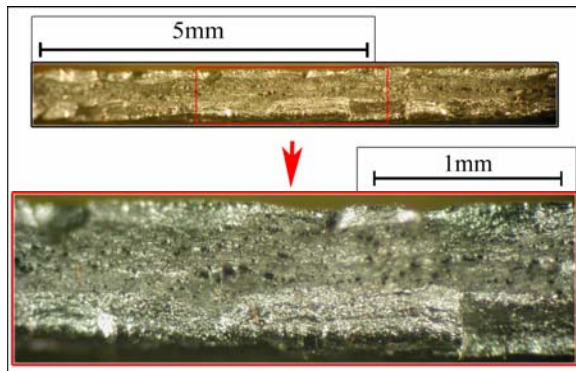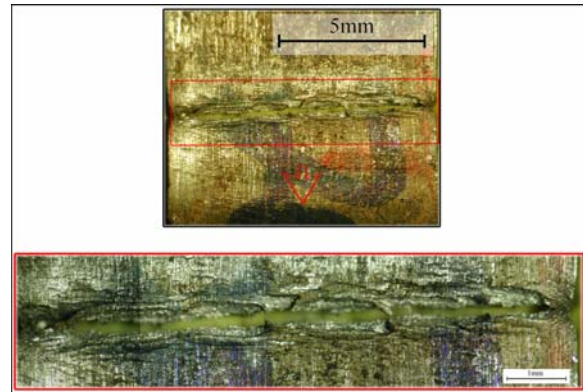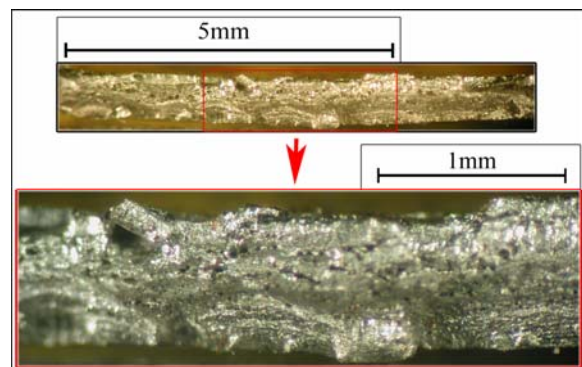

Fig. 10. The aspect of the breaking surface after breaking by alternate bending specific for type B.2 samples subjected to quenching from 900°C and tempered for one minute in the furnace maintained at 700°C. The images have been taken with a stereomicroscope.

In Figure 11 it is presented the surface of the steel strip in the vicinity of the fracture line after breaking by alternate bending; the images are taken with a stereo-microscope. It can be seen that on the surface of the strip cracks have been formed perpendicular to the edge of the strip in the whole area affected by alternate bending; generally the cracks are fine, but they get more pronounced in the immediate vicinity of the fracture line and in another area some 4 mm away from the fracture line in the rolling direction. The fracture line describes a straight line. In the immediate vicinity of the fracture line, deep cracks parallel with the fracture line can be observed. Also signs of material being pulled off between the opposite sides of the fracture line can be noticed; this suggests that, at the moment of the ultimate failure, some bridges still existed that maintained the continuity of the material. From all these observations it can be concluded that the rupture was caused by the development of cracks from the surface of the strip, perpendicular to the edge, cracks that had a role of stress concentrators on some critical sections, sections where the rupture was ductile by overloading.

triangle; this region has a uniform nuance and presents a generally featureless topography. The image from top-right shows a detail from this region taken at x1000 magnification. In this detail it can be noticed that the surface has a series of lines that ramify like rivers, lines characteristic to cleavage rupture – fragile rupture. Thus it can be said that this region represents a crack that formed in the material after strain hardening as a result of the alternate bending cycles. On the other hand, the detail taken at x500 magnification presented in the bottom-right image from Figure 12 is taken from the top-left region of the main image (taken at x120 magnification). In this second detail, the fracture surface has conical craters with different sizes and different depths, specific for ductile dimple rupture by overload. In some of these craters, at their bottom, a spherical carbide particle can be noticed – where the micro-void nucleated.

Fig. 11. The aspect of the surface of the strips after breaking by alternate bending, specific for type B.2 samples subjected to quenching from 900°C and tempered for one minute in the furnace maintained at 700°C. The images have been taken with a stereomicroscope.

The SEM details presented in Figure 12 explain very well the rupture mechanism involving the development of cracks from the surface of the strip followed by ductile rupture by overload. The main image taken at x120 magnification contains the whole thickness of the strip and is taken from a region close to the left edge of the fracture surface. In the image, it can be noticed that the fracture surface presents relatively large regions where the rupture took place by different mechanisms. There is one region which starts from the surface of the strip going towards the middle with a shape that can be approximated with a

Fig. 12. SEM details of the breaking surface after breaking by alternate bending characteristic for type B.2 samples subjected to quenching from 900°C and tempered for one minute in the furnace maintained at 700°C.

In Figure 13 there are presented a microstructure taken at x100 magnification and details from that main microstructure taken at x1000 optical magnification; the images are taken in the vicinity of the fracture surface in longitudinal section in the rolling direction, after breaking by alternate bending. Besides the fracture line, 3 cracks can be noticed that start from the surface of the strip towards the center, cracks that are presented in detail at x1000 optical magnification. One crack of this type is observed in the bottom-right region of the main image. It has a

depth of approximately 18 µm, it has a rectangular profile with a width of approximately 2 µm. It can be noticed that the crack stopped on a formation of free ferrite. Also in the bottom region, to the left, there is another crack starting from the surface of the strip towards to center. This crack has a depth of approximately 91 µm and has an irregular shape, with an opening at the surface of the strip of approximately 30 µm. Between this crack and the fracture surface there is a distance of approximately 74 µm, and the shape of the structural constituents in-between shows that the material was compressed. A third crack is located in the top side of the main image. It has a depth of approximately 37 µm and a width at the surface of the strip of approximately 24 µm.

The structural constituents located in the immediate vicinity of the vertical walls of the crack indicate that they suffered a deformation caused by the compression forces during the alternate bending cycles. The relatively large width of this crack and its shape – approximately rectangular – indicates that it formed during early stages of the alternate bending cycles, thus it had time to get wider by compressing the adjacent material. Also it can be noticed that the crack does not have a typical "V" shape profile, it is close to a "U" profile. This thing can be explained by the fact that the stretching forces caused by the bending cycles following the formation of the crack have stretched the material from the whole transversal section containing the crack.

The conclusion that rises from this observation is the fact that, as a consequence of the chemical inhomogeneity of the material, the propagation of the cracks started from the surface of the strip is stopped very efficiently by the islands of free ferrite, and even more they are not re-activated by the continuation of the destructive forces.

Regarding the profile of the fracture surface, from the images presented in Figure 13 it can be seen that the cracks that form at the interface between inclusions and the metallic matrix have an important role in the ultimate failure. These cracks lead to a step-like fracture surface profile, by linking cracks developed in transversal direction developed in different sections.

Depending on their depth and opening, it can be noticed that some of these cracks have formed during the early stages of the alternate bending cycles, some others have formed during the late stages of the alternate bending cycles and some have formed when the ultimate failure took place.

One of the cracks formed during the early stages of the alternate bending cycles is presented in detail in the image from top-left. The crack has a depth of approximately 114 µm and an opening at the fracture surface of approximately 23 µm. It can be noticed that the line of the upper wall of the crack describes a

sinuous profile in comparison to the profile of the lower wall of the crack which describes an arc with large radius.

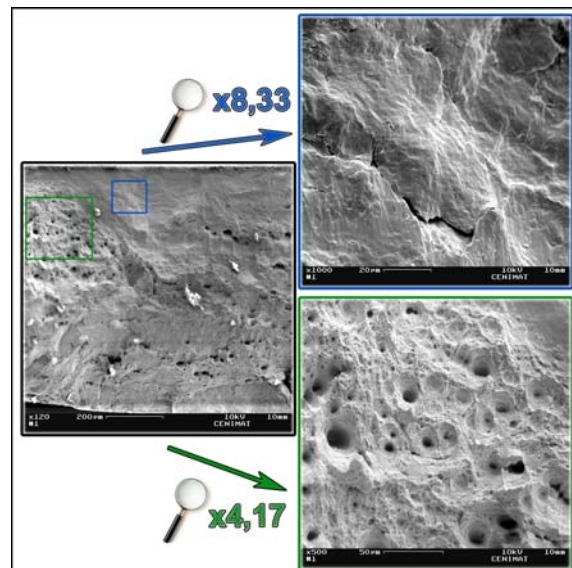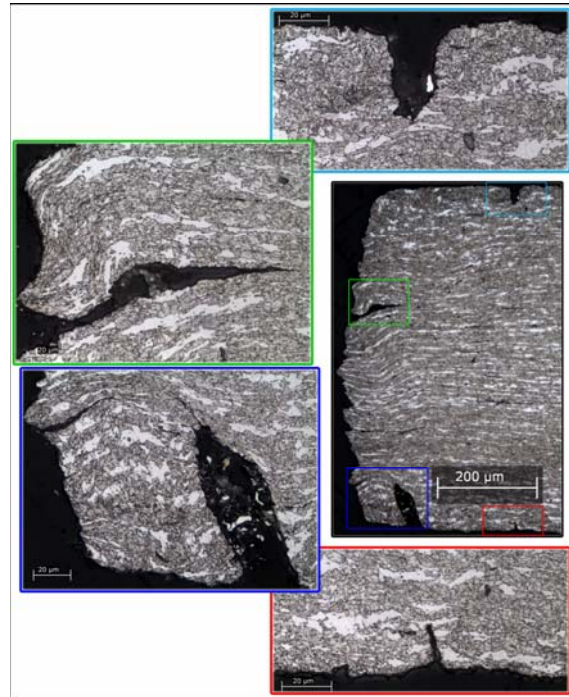*Fig. 13. Microstructures done in longitudinal section on the lamination direction, from the area adjacent to the breaking surface after breaking by alternate bending; microstructures characteristic for type B.2 samples subjected to quenching from 900°C and tempered for one minute in the furnace maintained at 700°C. Images done on etched sample with nital 5%, the main image was taken at x100 optical magnification and the details were taken at x1000 optical magnification.*

This difference is also observed in the texture of the microstructural constituents from the material in the upper side of the crack and respectively the lower side. Thus it can be concluded that the rupture in transversal plane took place in successive sequential steps delimited by the location of cracks parallel to the surface of the strip developed at the interface between inclusions and metallic matrix.

All of the above observations show the fact that the cracks parallel to the surface of the strip developed at the interface between inclusions and the metallic matrix and the cracks caused by strain-hardening due to the stretching-compression cycles, they both concur and have an important role in the rupture mechanism of the samples subjected to continuous flux quenching from 900°C and tempering for one minute at 700°C.

5. Conclusions

The steel strips that were in strain-hardened state, also used as raw material for the continuous flux thermally treated samples, showed an unfavorable behavior at alternate bending. Mainly because most of the destructive effects of alternate bending are located inside the material in the entire region affected by alternate bending, and only later, signs of destruction appear on the surface of the strip. The reason for that is the fact that the residual stress from the plastic deformation increases the risk of decohesive rupture at the interface between inclusions and the metallic matrix.

After applying the continuous flux thermal treatment of quenching from 900°C and tempering for one minute by passing through the furnace maintained at 600°C the tensile strength is similar to that of the raw material and the resistance at alternate bending also appears to be similar to that of the raw material in strain-hardened state. But there are considerably less cracks developed at the interface between inclusions and the metallic matrix; thus the damage inside the material with consequences on the tensile strength and elongation are reduced. Also signs of destruction due to alternate bending are more easily observed as the cracks started from the surface of the strip play a more important role in the fracture mechanism.

The resistance at alternate bending is significantly increased after applying the continuous flux thermal treatment of quenching from 900°C and tempering for one minute by passing through the furnace maintained at 700°C. The first cracks are observed after bending for 8 times compared to 6 times for the raw material and failure takes place after bending for 11 times compared to 7 times. Also the tensile strength is reduced down to 700 MPa and the A_{80mm} breaking elongation is increased up to 14.3%. The cracks started from the surface of the strip after strain hardening as a direct consequence of stretching-compression cycles during the alternate bending play an important role in the ultimate failure. The increase in resistance at alternate bending is explained by the fact that these cracks which started from the surface of the strips are stopped by the free ferrite formations occurred during the thermal treatment because of the chemical inhomogeneity within the material caused by the manganese content.

References

[1]. **Tiberiu Potecaşu, Octavian Potecaşu, Rui Jorge Cordeiro Silva**, *Straps of high resistance processed of steel with low carbon*, Metalurgia Internaţional, Vol XV, No. 4, 2010, pg. 50-53, ISSN 1582-2214;

[2]. **ASM Handbook**, Volume 12, *Fractography*, published in 1987 as Volume 12 of the 9th Edition *Metals Handbook (second printing 1992)*.

[3]. **Madeleine Durand-Charre**, *Microstructure of Steels and Cast Irons*, Springer-Verlag Berlin Hidelberg New York, ISBN 3-540-20963-8, Germany, 2004.

[4]. **H.K.D.H Bhadeshia**, *Bainite in Steels Transformations, Microstructure and Properties 2nd editon*, Cambridge University Press, ISBN 1-86125-112-2, UK, 2001.

[5]. **H. K. D. H. Bhadeshia**, *Interpretation of the Microstructure of Steels*, http://www.msm.cam.ac.uk/phase-trans/2008/Steel_Microstructure/SM.html

PRODUCING BIMETALS BY DIRECT MELTING OF THE BRONZE MACHINING CHIPS INTO STEEL SUPPORTS

Anişoara CIOCAN, Florentina POTECAŞU

Dunărea de Jos University of Galati
email: aciocan@ugal.ro

ABSTRACT

The bimetals can satisfy some requests of the working conditions impossible to be obtained using one single metallic material. The bimetallic pieces are obtained by the different production methods by covering of a steel support with the non-ferrous alloys layers. The possibility of bimetals producing by direct melting of the bronze machining chips into steel support is considered in this work. In this way the superior valorisation of the metallic scraps for obtaining bimetallic steel-bronze parts was studied. The recycling of the metallic wastes as final products with added value is possible to be achieved. In this paper the flow sheet for the bimetal manufacturing through this method was showed. Also the parameters that influenced the quality of bimetal were analysed. The quality of the bimetal was analysed in term of contact zone quality. The interface zone of two alloys was investigated through the methods of metallographic and microscopic analyses.

KEYWORDS: bimetals, recycling, bronze chips, steel

1. Introduction

In many industrial applications, the working surfaces of the parts are simultaneously exposed to a very different kind of stresses. In these types of working regime, the bimetallic materials can be used. These materials are obtained using the depositing process of one material, as layers with different thicknesses, on top of another material considered as a base. These metallic materials, also named bimetallic can satisfy some requests of the working conditions impossible to be obtained using one single metallic material.

The covered steels with non-ferrous alloys layers are an example and the bimetallic pieces are obtained through the different production methods. The bimetals are obtained by metallic layers deposition on the surface of the support parts.

The joining of the metallic layer on the solid support is determined by diffusion and thermal processes [1]. The metal deposition most is made on one or both surfaces of the solid support.

The thickness of covering layers is 8 – 20% of the support alloy.

The first data about the bimetals is early mentioned. In the published papers, it is shown that 1858 is the year when the first patent (USA Patent) for the obtaining of bimetal is mentioned.

For Germany, the researches for the production of the cladded steel sheets begin in the seventh decade of the XIXth century and a patent was realized. The first special industrial application for bimetals occurred in 1930.

This happened in USA and referred to the utilization of some steel sheets with nickel cladded for the construction of the tank wagon for the chemical products transports.

The production of the great quantity of the carbon steel sheets cladded with stainless steel starts around 1938 [2].

One method of obtaining the bronze layer added on the steel support for the bimetal manufacturing is through by welding process. For this is necessary to remelt the bronze wastes and to mould them in the form of bars. The gas-shielded arc welding process with wolfram electrode can be used for welding bronze on the parent steel [3, 4].

During the obtaining bimetal of through this method, a lot of problems are associated: the loss of metal is greater; the costs of labour and energy or materials are increased as well as the problems of environment protection are higher.

The present paper presents the researches for bimetal manufacturing from waste products.

To create a bronze layer on the steel surface, bronze machining chips were used. In this case the

chips waste of the bronze with aluminium complex alloyed with iron, nickel, manganese was used.

2. Experimentals research and materials

In the experimental work, steel samples as supports were used, Figure 1. In accordance with the complex work of this bimetal that was used as bearing parts (ability to carry heavy loads under friction conditions without excessive wear and resistance to corrosion), we used selected bronze chips in accordance with certain chemical compositions Table 1 [5, 6].
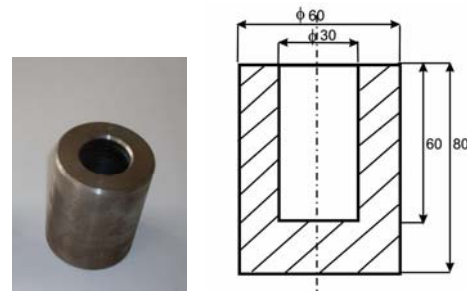
Fig. 1. Experimental steel sample used as steel support into the experimental research

Table 1. Chemical composition of the bronze

Elements, [wt%]	Al	Ni	Fe	Mn	Cu
Range expected	14-15	4-4.5	4-4.5	0.8-1.2	bal.
Chips	14.7	4.4	4.1	1.1	bal.

The fluxes with multiple actions were used: borax as neutral cover fluxes, glassy fluid cover flux, graphite as reducing flux containing carbonaceous materials and, copper-phosphorus metal mixed with bronze chips that are self-fluxing on copper-base metals [7]. A resistance furnace was used for heating the samples, Figure 2.

Fig. 2. Furnace used for melting the bronze chips into the steel support

The quality of bimetal is discussed in term of contact surface for both alloys (steel and bronze with nickel, iron and manganese). The structural aspects associated with the heating process were presented. An Olympus microscope Metallographic was used. Optical microscopy included standard methods for preparing samples.

2. Results and discussions

Although the method proposed for bimetal manufacturing is cheap and simple, this involves some problems. The main problems are associated with the quality and the properties of the bronze layer and the bronze chips. Other are associated with processes that accompany the copper alloys melting and joining the steel support. The first condition for a quality process refers to the properties of the recycled material. The success of any melting system depends on the physical characteristics and nature of the feedstock, therefore, the integration of durable, efficient pre-treatment is crucial in achieving full processing efficiency and hence, a high metal recovery. This is particularly important when recycling the machining chips, which have a high surface area per unit volume. Even small residues of water/oil soluble fluid will have a significant impact on metal recovery. Such contaminants interfere with the bronze and may lessen the joint strength or cause failure. For this reason, the first step of the flow sheet is the pre-treatment.

For good bronze melting into steel support are necessary small and uniform chips. The machining chips have various forms. The types of chips are categorised or subdivided into the following categories, Figure 3.

To obtain the uniform chip size, these are crushed. The cleaning can be considered to be a two-stage process. In the first process of the stage the centrifuge separation to minimize water and coolants is applied. Also the magnetic separation to eliminate ferrous parts is sometimes necessary. The second process of this cleaning stage is based on thermal processes. The goal is to remove the organic compounds from the surface of the chips by converting them into a gaseous state. This process requires a low temperature. Any water that is present within the chips will be vaporized. Then, at a higher

temperature is removed the carbon-based deposit that remains on the surface of the chips.

The second condition for a quality process refers to the physical and chemical processes that are developed in accordance with thermal conditions that occur during at the melting of the copper alloys chips and during the heating steel support.

a.

b.
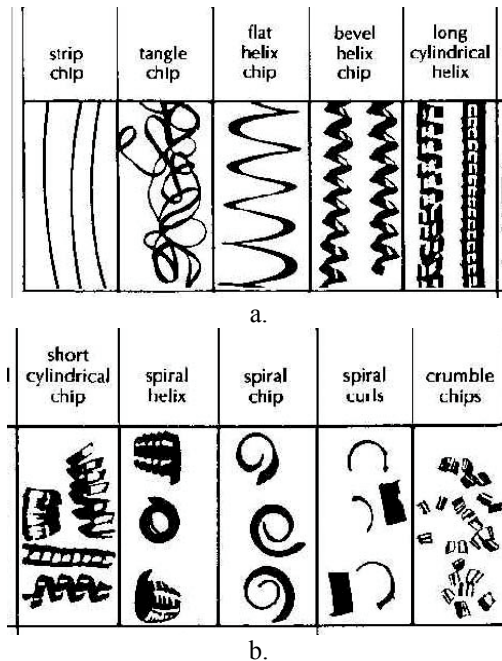
Fig. 3. *Chip forming classification: a - not desirable; b – good [8]*

Copper is considered a half noble metal but with a high solubility for oxygen in the liquid state. Generally an oxygen and hydrogen pick-up can lead to very negative effects on mechanical and physical properties of copper and copper alloys. These gases have a high solubility in liquid copper alloys that decreases sharply during solidification. This can lead to bubble formation, i.e. porosity in the solid material. Oxygen can also form cuprous oxide (Cu_2O) above its solubility level that immediately reacts with the moisture of the air forming water vapors. Dissolved hydrogen and oxygen (or Cu_2O) will react with water under extreme pressure in the lattice and will form cracks and lead to embrittlement [9].

Borax, as a neutral cover flux, is used to reduce metal loss by providing a flux cover. This melts at copper alloy melting temperatures to provide a fluid slag cover (borax melts at approximately 740^0C). The glassy fluid cover flux is used too. This flux agglomerates and absorbs nonmetallic impurities from the input material (oxides, machining lubricants, and so on). A reducing flux containing carbonaceous materials such as graphite is used. Its principal advantage lies in reducing oxygen absorption of the copper and reducing melt loss. Carbonaceous flux

material should always be used with copper alloys to avoid gaseous reactions with sulfur or hydrogen from contained moisture. Use was made of the copper-phosphorus metal mixed with bronze chips that are considered self-fluxing on copper-base metals. Some of these fluxes are mixed with bronze chips and some covered the input materials after their preliminary heating.

The steel samples were also heated before the filling with bronze chips and fluxes. The amount of flux used was established in accordance with its effect on the porosity and mechanical properties of the bronze alloy. This is more than 5% of metal charge.

Fig. 4. *Preparation of the samples before insertion in the heating furnace*

The heating temperature ensures only the melting of the bronze chips and also for the bronze bounding on the surface of the steel. The heating temperature is very important for obtaining a good adhesion of the bronze layer on steel surface. This was established in accordance with the thermal process that is developed in the samples.

The thermal regime should ensure the melting of the bronze, the superheating of this melt for developing the diffusion zone at interface with the steel support. Certainly, this was correlated with the Cu-Al binary diagram and with the influence of other elements (iron, nickel and manganese) that are present in the aluminium bronze composition. After heating, the samples were maintained at optimum temperature and then were slowly cooled together with the furnace.

The experiments were carried out at different work temperatures between 1200 and 1300^0C. The experimental part shows that heating of the samples at 1200^0C cannot ensure a complete melting of the bronze chips, Figure 5.

Fig. 5. *Bronze chips incompletely melted often being heated at 1200^0C*

The choice of 1300^0C as optimum temperature is confirmed by the experimental samples, Figure6.
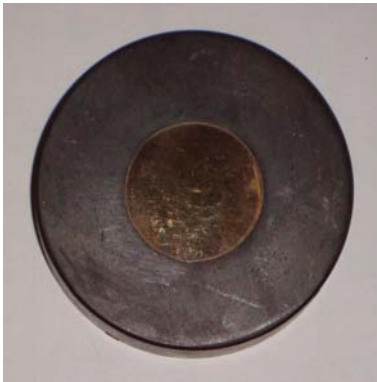
Fig. 6. *Good adherence of bronze on the steel surface for the bimetal sample obtained at 1300^0C, slowly cooled with the furnace (surface after exposure to metallographic attack)*

At the surface of the support steel, the aluminium bronze with nickel, manganese and iron was adhered to obtain the bimetal. The appearance of the joint zone shows that the process was conducted with optimum parameters. The surface layer had no defects such as oxide films, or porosity, Figures 7 and 8. The bonding takes place during heating and melting processes. In this way, with participation of diffusion processes good bimetals can be manufactured.

Fig. 7. *Aspect of bimetal at interface (100X without exposure to metallographic attack)*

The microstructural analysis shows that the interface layer formed by micro-melting and diffusion is very fine and uniform.

The transition area has a thickness of approximately 50µm and it resulted from the mass transfer processes developed between the two materials.
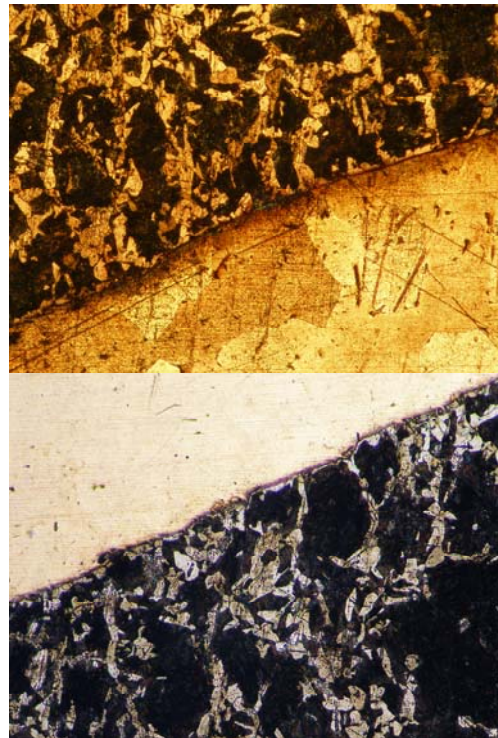
Fig. 8. *Microstructure of bronze and steel support after exposure to metallographic attack (100X)*

For comparison with the technology used for the production of similar bi-metals obtained by welding, it can be said that, in the case of the bi-metal obtained through the plating of bronze onto the steel support [4], the transition area is more extended, of approximately 150µm and it results from the diffusion processes caused by the high temperatures developed during welding and thermal treatment, respectively the concentration gradients between the two alloys (Figure 9).

Fig. 9. *Microstructure of bimetal after exposure to metallographic attack (X200)*

The optimal performances regarding the behavior during exploitation of the bi-metals can be obtained only by knowing, and respectively, by controlling of the composition and microstructural transformations, both for the constitutive materials and the diffusion area developed at their interface.

4. Conclusions

The recycling of the chips usually presents many difficulties [10, 11]. Firstly, the metal chips can be classified in the category of hazardous waste because they have residues of water/oil soluble fluid with significant impact on metal recovery. The generation of pollutants is considerable. In the method proposed in this paper, some of these negative problems are suppressed. On the other hand, the metal losses at remelting are higher.

The direct melting of the bronze chips into steel supports for the bimetal manufacturing is possible. It is a cheap and simple solution to transform the machinery wastes as final products that can meet the requirements in industrial applications. The important factors that influenced the manufacturing process are the dimension of the chips and the cleaning. Also, heating and the melting parameters correlate in accordance with the physical and chemical properties of materials most. Especially, all of these have specific features in respect to the materials utilised, the manufacturing processes and the bimetal applications.

References

[1]. **Popovits, D., Subu, T**.- *Bimetale,* Editura Facla, Timişoara, 1982.

[2]. **Radu, T., S. Constatinescu, S., Balint, L**. – *Materiale metalice rezistente la coroziune,* Editura F.M.R., Bucureşti, 2004.

[3]. **Ciocan, A., Bratu, F.-** *Chemical and structural changes for bimetallic materials obtained by the welding process*, The Annals of Dunarea de Jos University of Galati, no. 2, 2005, p.15-22.

[4]. **A. Ciocan, A., Potecasu, F., Drugescu, E., Constantinescu, S.** - *Characterization of the Diffusion Zone Developed in a Bimetallic Steel-Bronze at Interface*, Materials Science Forum; Trans Tech Publications LTD Switzerland, UK, USA III, 2010, Vols. 636-637, pp 556-563.

[5]. **Campbell, H**. - *Aluminum bronzes alloys. Corrosion resistance guide*, Publication 80, Copper Development Association, U.K., pp.1-27, July 1981, www.cda.org.uk.

[6]. *** - *Aluminium Bronze alloys for industry*, CDA Publication No.83, 1986.

[7]. **Ciocan, A.** - *Scraps Recycling. Technology for Processing and Valorization of Copper Scraps,* Editura Fundaţia Ştiinţifică Metalurgia Română, Bucureşti, 2004;

[8]. *** - *Standard test method of evaluating machining performance of ferrous metals using an automatic screw/bar machine*, ASTM E618, American Society for Testing and Materials, Philadelphia, USA.

[9]. **Oprea, Fl**.- *Teoria proceselor metalurgice,* EDP, Bucureşti, 1966.

[10]. **Gronostajski, J., Chmura, W., Gronostajski, Z**. - *Phases created during diffusion bonding of aluminium and aluminium bronze chips*, Journal of Achievements in Materials and Manufacturing Engineering, Volume 19 ISSUE 1 November 2006, p.32-37

[11]. **Copper Development Association**, *Cost-Effective Manufacturing Machining Brass, Copper and its Alloys*, Publication TN 44, October 1992 – Revised for inclusion on CD-Rom, May 1994

INFLUENCE OF THE NANOPARTICLES SIZE ON THE PERMEATION PROPERTIES OF THE POLYMERIC MEMBRANES

Stefan BALTA[1,2], Lidia BENEA[1], Bart Van der BRUGGEN[2]

[1]Department of Environmental and Material Engineering, University Dunarea de Jos, Galati, Romania
[2]Department of Chemical Engineering K.U.Leuven, Belgium;
email: stefan.balta@ugal.ro, lidia.benea@ugal.ro

ABSTRACT

In this study, polyethersulfone (PES) membranes blended with zinc oxide nanoparticles (ZnO) were manufactured by diffusion induced phase inversion in N-Methyl-pyrrolidone (NMP) as solvent and deionized water as coagulant, in view of increasing the properties of the polymeric membranes. Neat PES membranes were modified by dispersing ZnO nanoparticles with two different sizes in a PES casting solution. Four different concentrations of nanoparticles was studied between 0.035 to 1 wt.% for four different concentration of PES (25, 27, 30 and 32 wt.%). The influence of the ZnO nanoparticles size on the permeation performances of PES/ZnO membranes were investigated with contact angle and filtration experiments. The results show an important improvement of the neat membranes properties, permeability and flux, by adding ZnO nanoparticles with two different size even at a smaller concentration, less than 0.5 wt.%. The influence of the nanoparticles size is obvious, decreasing the nanoparticles size, the permeation properties of the polymeric membranes increase.

KEYWORDS: nanofiltration, ZnO nanoparticles, membrane synthesis

1. Introduction

Polyethersulfone is one of the most common polymers used in nanofiltration (NF). PES membranes are applied in the treatment of wastewater in industry [1-3] and in the production of drinking water [4-5] because they have a high retention of multivalent ions and organic molecules with a molecular weight above 300 Da. One of the main problems of the nanofiltration is the fouling phenomenon, this is attributed to the organic adsorption on the membrane surface. Membrane fouling leads to diminished the membrane performance, seriously deficient production, and excessive operating costs [6,7]. Because of the fouling, the dyes rejection [8-10] and the permeation properties [11-13] of the membranes decrease due to a higher hidrophobicity of the membrane surface. Membrane fouling depends on the membrane characteristics [14-17] and on the filtration mode (cross-flow or dead-end filtration) [18].

In view of improving the fouling resistance and other properties of polymeric membranes like permeation, thermal stabilities, and mechanical properties, many types of nanoparticles have been used to prepare composite membrane recently, and their application fields have covered microfiltration [19,20], ultrafiltration [21–27], gas separation [28,29], as well as pervaporation [30].

The composite membranes are in general prepared by dispersing the nanoparticles in the casting solution and prepare the membrane via phase inversion [31-37] or by dipping the prepared membrane in a suspension with nanoparticles [38, 39]. The advantage of the first method is that the nanoparticles are more stable in the polymer matrix in comparison with the second method but with a lower efficiency of the nanoparticles use.

The effects of nanoparticles as additive on the preparation of polyethersulfune (PES) blend nanofiltration membranes were investigated in terms of water pure flux and hydraulic membrane resistance (permeability). In this study, a polyethersulfune (PES) membrane was modified by dispersing two different nano-sized zinc oxides particles in a PES solution with N-Methyl-pyrrolidone (NMP) as solvent.

2. Experiment

2.1 Materials

The support layer, Viledon FO2471, for the membrane manufacturing was obtained in Freudenberg (Weinheim, Germany). The polymer

used was Polyethersulfone, provided by Solvay (Belgium) and like solvent was chosen 1-Methyl-2-pyrrolidone (NMP, 99.5%). ZnO nanoparticles, and it was provided by Sigma-Aldrich (St. Louis, MO).

2.2 Membrane preparation

Neat Polyethersulfone membranes and blended with ZnO nanoparticles were manufactured at different concentrations of polymer (25, 27, 30 and 32 wt.%) and nanoparticles with two different size, 50nm and 80 nm, in N-Methyl-pyrrolidone as solvent using the phase inversion induced by immersion precipitation. Four different concentrations of ZnO nanoparticles, for both sizes, were used: 0.250, 0.500, 0,750, and 1 wt.%. The casting solution was obtained by adding ZnO nanoparticles into the solvent and mixed through mechanical stirring at 200 rpm and room temperature. After three hours the polymer was added to the solution and stirred for 24 hours at 40^{0}C and 500 rpm. A thin film of the polymer solution with a thickness of 250 μm was cast on a polyester support with a filmograph (K4340 Automatic Film Applicator, Elcometer) in an atmosphere with relatively controlled air humidity, at room temperatures. After casting the membrane was immersed in a non-solvent coagulation bath for precipitation. After 15 minutes, to remove the excess of solvent, the membrane were repeatedly washed and stored in distilled water. For every type of membrane, two different solutions were made and from every solution three membranes was manufactured and tested to obtain the true values of retention and permeation properties of the membranes.

2.3. Water contact angle

To study the hydrophilicity/hydrophobicity of the membranes was used a Drop Shape Analysis System DSA 10 Mk2. On the cleaned and dry membrane surface was placed a distillate water droplet of 2 μl and the contact angle between the membrane surface and the droplet was calculated (figure 1). The final value of the contact angle for every type of membranes was the average 21 measurements, seven determinations for three different membranes.
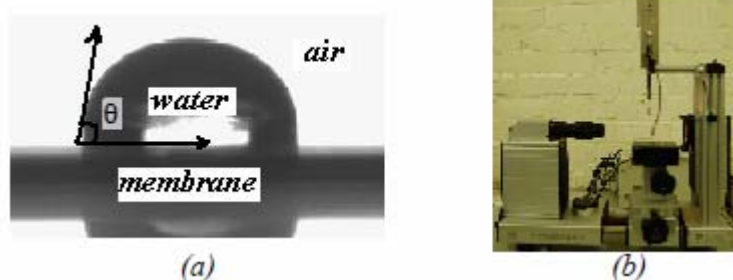
Fig. 1. Contact angle measurements: (a) the principle and (b) the setup

2.4. Filtration experiment

To determine the pure water flux, have been tested all the membranes for a long time in a cross flow installation (figure 2b). In all experiments the temperature was 24 °C and the applied pressure was 8 bars. The membranes surface area was 0.0059m^2 and the time for every experiment was 24 hours.
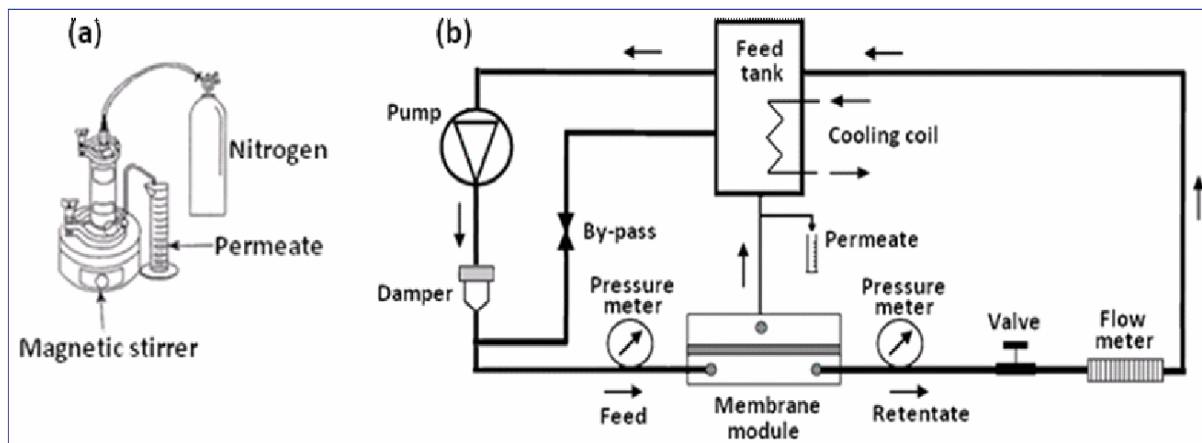
Fig. 2. Filtration equipment: a) dead-end and b) cross flow

The pure water flux and permeability of the prepared membranes were studied using a dead end filtration device (figure 2b).

All experiments were made at the room temperature at desirable pressure on the Sterlitech HP4750 Stirred Cell to keep a homogeneous solution inside of the dead end device. The pressure was realized with a nitrogen cylinder with a pressure regulator, connected to the cell. A wide range of membranes were tested, five samples for six different membranes.

The final results are the average of 30 experimental values. The solution volume was 250 ml and the permeate was collected in a graduate cylinder. The pure water flux was determined at 10 bar pressure and the time was measured at every 5 ml of permeate.

To determine the pure water permeability (PWP), the water flux (J_w) was measured at six different pressure (ΔP) from 5 to 20 bar. The PWP was calculated by the following equation:

$$PWP = \frac{J_w}{\Delta P}$$

(1)

3. Results and discussions

3.1. Pure water flux and permeability

It was observed that the polymer concentration has a negative influence on the permeation properties of membranes. Increasing the concentration of PES the pore size decrease and in consequence the pure water flux (figure 3) and permeability (figure 4) decrease. Membranes with 25% of PES have a good permeability but because of the weaker mechanical resistance, they have an important instability of flux in time. For 30 and 32% of PES the improvement is not so evident in comparison with membranes at smaller concentration of polymer. For this reason and because of the membranes instability at 25% of PES, the membranes at 27% were chosen for future studies.
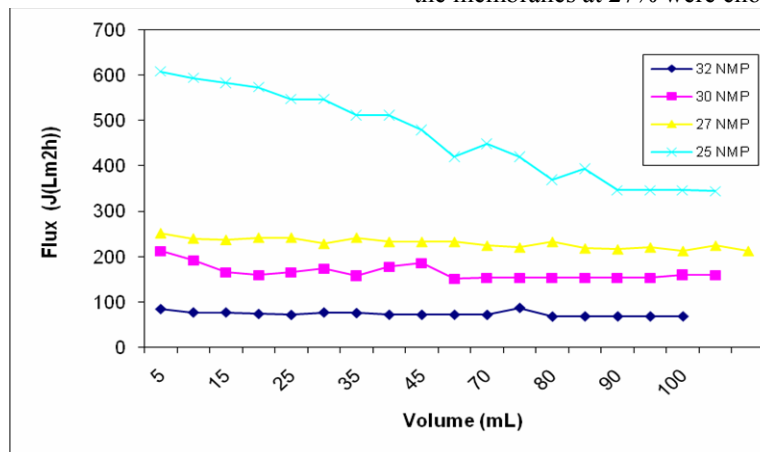
Fig. 3. *Pure water flux of neat membranes at different concentrations of PES*
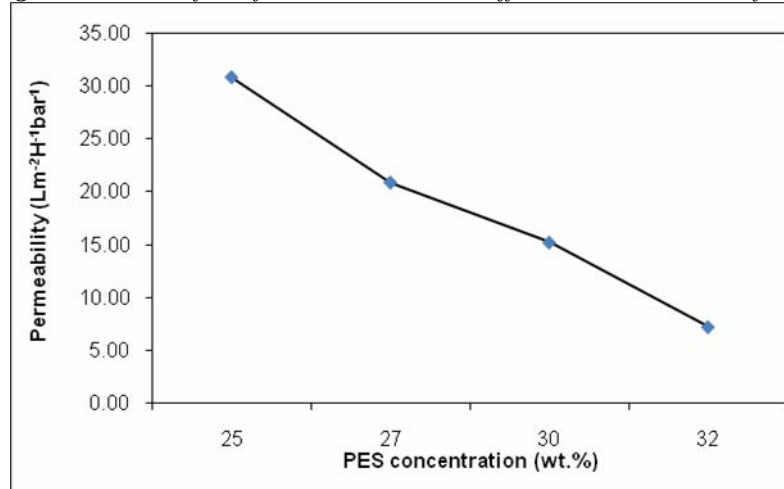
Fig. 4. *Permeability of neat membranes at different concentrations of PES*

The addition of a small amount of nanoparticles with 80nm size, 0.250 wt.%, increases both pure water flux and permeability.

Decreasing the nanoparticles size until 50nm, the permeability and pure water flux increase.
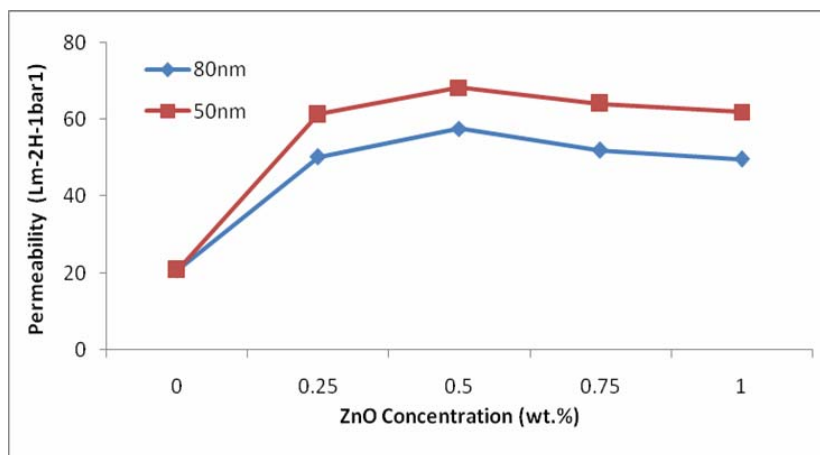
Fig. 5. Permeability of blended membranes with different size of nanoparticles
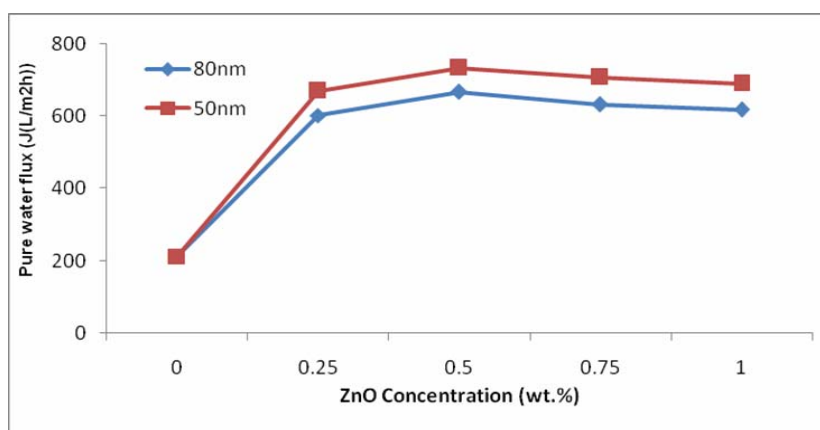
Fig. 6. Pure water flux of blended membranes with different size of nanoparticles

The comparison of the results for different sizes of nanoparticles shows the same tendency of the permeability (figure 5) and pure water flux (figure 6) but with an important improvement.

For example the permeability for the membranes with a concentration of 0.250 wt.% of nanoparticles increases from 50.25 for membranes with nanoparticles of 80 nm size up to 61.35 for membranes with nanoparticles of 50 nm size.

These results show an important influence of the nanoparticle size on the permeation properties of the polymeric membranes.

3.2. Hydrophilicity and contact angle

To study the membrane surface hydrophobicity a contact angle experiment was done, knowing that the membranes with a hydrophilic surface have a low contact angle [35].

Figure 7 shows the values of the contact angle for neat and blended membranes at different concentrations and sizes of the nanoparticles. The results show that membranes hydrophilicity increases when id added nanoparticles and in the same time it increases if the size of the nanoparticles decrease. In concordance with permeability the ZnO blended membranes are more hydrophilic than neat PES membranes.

Nanoparticles in comparison with polymer have a higher affinity to water, this can be an explanation for the increases of permeability by addition of nanoparticles.

It can be concluded that in comparison with other types of nanoparticles where the concentration has an important impact on the porosity [30, 36, 37], the concentration of ZnO nanoparticles does not have an important influence. For a large range of concentrations, the porosity is similar.
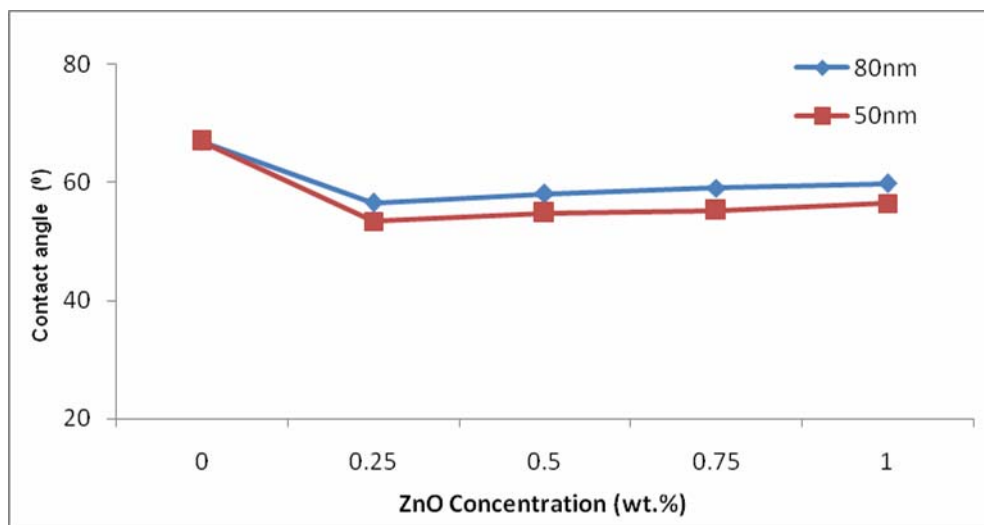
Fig. 7. Contact angle at different nanoparticle sizes and concentration

4. Conclusions

Neat and ZnO blended membranes were prepared via phase inversion by dispersing the ZnO nanoparticles in the PES casting solution. A systematic study of the influence of the polymer and ZnO nanoparticles size and concentration was carried out. Various experiments such as permeability and contact angle were utilized.

ZnO blended membrane showed lower flux decline and a better permeability compared to neat polymeric membrane due to a higher porosity of the ZnO membranes.

The size of the nanoparticles has an important influence on the permeation properties of the membranes. Decreasing the size of the nanoparticles the permeability and pure water flux of the membranes increase.

Acknowledgements

References

[1]. **L. De Florio, A. Giordano and D. Mattioli,** *Nanofiltration of low-contaminated textile rinsing effluents for on-site treatment and reuse*, Desalination 181 (2005) 283–92.

[2]. **G. Cornelis, K. Boussu, B. Van der Bruggen, I. De Vreese, C. Vandecasteele**, *Nanofiltration of nonionic surfactants: effect of molecular weight cut-off and contact angle on flux behaviour*, Ind Eng Chem Res 44 (2005) 7652–7658.

[3]. **C. Tang, V. Chen,** *Nanofiltration of textile wastewater for water reuse,* Desalination 143(2002) 11–20.

[4]. **IC. Escobar, AA. Randall, SK. Hong,** *Removal by Nanofiltration: Full and Bench-Scale Evaluation,* J Water Sup Res Technol Aqua 51 (2002) 67–76.

[5]. **A. Matilainen, R. Liikanen, M. Nystrom,** *Enhancement of the natural organic matter removal from drinking water by nanofiltration,* Environ Technol 25 (2004) 283–91.

[6]. **E. Matthiasson, B. Sivik,** *Concentration polarization and fouling*, Desalination 35 (1980) 59.

[7]. **D.E. Potts, R.C. Ahlert, S.S.Wang,** *A critical review of fouling of reverse osmosis membranes,* Desalination 36 (1981) 235.

[8]. **B. Van der Bruggen, M. Manttari, M. Nystrom**, *Drawbacks of applying nanofiltration and how to avoid them: A review*, Sep Pur Tech 63 (2008) 251–263

[9]. **B. Van der Bruggen, L. Braeken, C. Vandecasteele,** *Flux decline in nanofiltration due to adsorption of organic compounds,* Sep Pur Tech 29 (2002) 23–31

[10]. **L D. Nghiem, PJ. Coleman, C. Espendiller**, *Mechanisms underlying the effects of membrane fouling on the nanofiltration of trace organic contaminants,* Desalination 250 (2010) 682-687.

[11]. **L. Braeken, R. Ramaekers, Y. Zhang, G. Maes, B. Van der Bruggen, C. Vandecasteele** *Influence of hydrophobicity on retention in nanofiltration of aqueous solutions containing organic compounds* . J. Membr. Sci. 252 (2005) 195-203.

[12]. **JM. Arsuaga, MJ. López-Muñoz, A. Sotto,** *Correlation between retention and adsorption of phenolic compounds in nanofiltration membranes,* Desalination 250 (2010) 829-832

[13]. **L. Braeken L, K. Boussu K, B. Van der Bruggen B, C. Vandecasteele**, *Modeling of the adsorption of organic compounds on polymeric nanofiltration membranes in solutions containing two compounds*, Chemphyschem 6 (2005) 1606-1612.

[14]. **J.M. Laine, J.P. Hagstrom, M. Clark, M. Mallevialle,** *Effects of ultrafiltration membrane composition,* J. Am. Water Works Assoc. 81 (1989) 61–67.

[15]. **M. Elimelech, X. Zhu, A.E. Childress, S. Hong,** *Role of membrane surface morphology in colloidal fouling of cellulose acetate and composite aromatic polyamide reverse osmosis membranes,* J. Membr. Sci. 127 (1997) 101–109.

[16]. **C. Jucker, M.M. Clark**, *Adsorption of aquatic humic substances on hydrophobic ultrafiltration membranes,* J. Membr. Sci. 97 (1994) 37–52.

[17]. **J. Cho, G. Amy**, *Interactions between natural organic matter and membranes: rejection and fouling*, Water Sci. Technol. 40 (9) (1999) 131–139.

[18]. **D.B. Mosqueda-Jimenez, R.M. Narbaitz, T. Matsuura,** *Membrane fouling test: apparatus evaluation*, J. Environ. Eng. ASCE 130 (1) (2004) 90–98.

[19]. **H.Q. Lu, L.X. Zhang, W.H. Xing, H.T. Wang, N.P. Xu,** Mater. Chem. Phys. 94 (2005) 322.

[20]. **A. Bottino, G. Capannelli, V. D'Asti, P. Piaggio**, Sep. Purif. Technol. 22 (2001) 269.

[21]. Y.N. Yang, H.X. Zhang, P. Wang, Q.Z. Zheng, J. Li, J. Membr. Sci. 288 (2007) 231.

[22]. Y.N. Yang, P. Wang, Q.Z. Zheng, J. Polym. Sci. Part B: Polym. Phys. 44 (2006) 879.

[23]. L. Yan, Y.S. Li, C.B. Xiang, Polymer 46 (2005) 7701.

[24]. X.C. Cao, J. Ma, X.H. Shi, Z.J. Ren, Appl. Surf. Sci. 253 (2006) 2003.

[25]. L. Yan, Y.S. Li, C.B. Xiang, X.D. Shun, J. Membr. Sci. 276 (2006) 162.

[26]. P. Jian, H. Yahui, W. Yang, L. Linlin, J. Membr. Sci. 284 (2006) 9.

[27]. Y.N. Yang, P. Wang, Polymer 47 (2006) 2683.

[28]. Y. Kong, H.W. Du, J.R. Yang, D.Q. Shi, Y.F. Wang, Y.Y. Zhang, W. Xin, Desalination 146 (2002) 49.

[29]. G. Clarizia, C. Algieria, E. Drioli, Polymer 45 (2004) 5671.

[30]. M. Sairam, M.B. Patil, R.S. Veerapur, S.A. Patil, T.M. Aminabhavi, J. Membr. Sci. 281 (2006) 95.

[31]. Y.N. Yang, H.X. Zhang, P. Wang, Q.Z. Zheng, J. Li, *Effect of TiO$_2$ nanoparticles on the surface morphology and performance of microporous PES membrane,* J. Membr. Sci. 288 (2007) 231.

[32]. L. Yan, Y.S. Li, C.B. Xiang, *Preparation of poly(vinylidene fluoride)(pvdf) ultrafiltration membrane modified by nano-sized alumina (Al$_2$O$_3$) and its antifouling research*, Polymer 46 (2005) 7701.

[33]. X.C. Cao, J. Ma, X.H. Shi, Z.J. Ren, *Effect of TiO$_2$ nanoparticle size on the performance of PVDF membrane*, Appl. Surf. Sci. 253 (2006) 2003.

[34]. L. Yan, Y.S. Li, C.B. Xiang, X.D. Shun, *Effect of nano-sized Al$_2$O$_3$-particle addition on PVDF ultrafiltration membrane performance* J., Membr. Sci. 276 (2006) 162.

[35]. P. Jian, H. Yahui, W. Yang, L. Linlin, Preparation of polysulfone–Fe$_3$O$_4$ composite ultrafiltration membrane and its behavior in magnetic field, J. Membr. Sci. 284 (2006) 9.

[36]. Y.N. Yang, P. Wang, *Preparation and characterizations of a new PS/TiO$_2$ hybrid membranes by sol–gel process,* Polymer 47 (2006) 2683.

[37]. C.M. Wu, T.W. Xu, W.H. Yang, *Fundamental studies of a new hybrid (inorganic–organic) positively charged membrane: membrane preparation and characterizations,* J. Membr. Sci. 216 (2003) 269.

[38]. T.H. Bae, I.C. Kim, T.M. Tak, Preparation and characterization of fouling-resistant TiO$_2$ self-assembled nanocomposite membranes, J. Membr. Sci. 275 (2006) 1.

[39]. M.L. Luo, J.Q. Zhao, W. Tang, C.S. Pu, *Hydrophilic modification of poly(ether sulfone) ultrafiltration membrane surface by self-assembly of TiO$_2$ nanoparticles* Appl. Surf. Sci. 249 (2005) 76.

METHOD AND PROCEDURE FOR CHECKING THE ACCURACY OF THE SCAN-INDEXING SYSTEM OF THE NDT-UT EQUIPMENT FOR IMMERSION TECHNIQUE

[1]Alexandru GIURA,[1]Alexandru STANCIOIU,
[1]Petrişor GAGIU,[2]RAUL Novac
[1]S.C. ALRO S.A. Slatina
[2]"Dunărea de Jos" University of Galati
email: agiura@alro.ro; astancioiu@alro.ro

ABSTRACT

This paper deals with the proposal of a method and procedure to verify the accuracy of the scanning-indexing system of the NDT-UT facility for immersion technique, using comparison with a plate of aluminum alloy plate, processed as a test plate

KEYWORDS: transducer, ultra-sounds, flat bottom hole, test plate, immersion technique, encoder, DA converter, coupling.

1. Introduction

In the non-destructive testing of aluminum alloy plates, using ultrasounds, there are generally used two techniques, i.e.: contact ultrasonic testing where the ultrasonic transducer is brought into physical contact with the controlled material and immersion ultrasound control where the ultrasonic transducers move near the material being controlled while this is immersed in the working fluid, which is called coupling.

The coupling used in immersion technique is generally water which has undergone demineralization treatment, mechanical filtration of particles, corrosion inhibitor treatments (sometimes this treatment may be absent) and ultraviolet sterilization treatments or other methods. Also the coupling temperature is monitored and controlled to ensure consistency of the utilization properties.

Ultrasonic nondestructive testing facility, using the immersion technique, features high accuracy and is productive for materials with big dimensions. In order to move ultrasonic transducers throughout the surface of the material to control and to be able to identify and accurately store the coordinates of defects, a so called scanning and indexing system is needed to ensure the required accuracy.

This system, present in all nondestructive ultrasonic immersion technique facilities is mostly automatic and can move the transducers in the horizontal plane formed by X and Y axes of the facility. Being responsible for detecting the coordinates of the defects found by the transducers,

one might seriously question the accuracy of the measurement provided by that system, both onto the scanning direction (longitudinal axis X) and onto the indexing direction (transverse axis Y). Therefore specifications such as [2] and [3] contain acceptance criteria as regards its maximum permissible error, ie ± 2.5 mm for both X axis and Y axis. Obviously, to show compliance with this requirement it is necessary to evaluate the measurement accuracy of the scanning - indexing system

The metrology issue of assessing the accuracy of the measurement, in general, and that associated to scanning – indexing systems, in particular, raises a number of technical difficulties and additional costs. In this context, this paper proposes a practical method and procedure for assessing the accuracy of scanning and indexing to satisfactorily overcome these difficulties.

2. Difficulties and costs

To solve the problem posed by the necessity of knowing the accuracy of scanning and indexing, it is necessary first to identify the main difficulties which arise in this problem.

A first category of problems to be solved is related to setting a budget of uncertainty associated with scanning and indexing respectively, the budget including factors which cause significant errors in determining the X and Y coordinates (see Chapter 5) [1], [4]. Another category of issues raised in determining the accuracy of scanning and indexing

refers to the formulation of a working procedure able to cover the budget of uncertainty. All these elements require specific expertise of the specialists who perform the assessment of accuracy, an expertise which is generally not available in any organization that operates NDT-UT-immersion facilities. That is why generally specialized laboratories or manufacturers resort to this type of equipment.

The costs associated with scanning and indexing accuracy assessment are according to the authors' experience, quite high. An example could be the cost calculated from the necessary measurement points. Thus, a number of measuring points is about 40, and if the charges applied from the list of the official rates of the Romanian Bureau of Legal Metrology, the entire cost of the assessment would be about 2,000 Ron (650 USD) for each installation. If this check is run quarterly, its annual cost may rise to 8,000 RON (2,600 USD).

Where accuracy assessment should be conducted by a provider outside the country, these costs would double, exceeding 5,000 USD annually for each facility inspected. This cost would add the other costs of verification for such a facility, adding an extra effort to support the operating costs. Hence, any effort to solve the problem of assessing the accuracy of scanning and indexing by the metrological department of the organization that operates one or more immersion ultrasound inspection facilities presents a real practical interest.

3. Description of the scanning – indexing system

The figure 1 below illustrates the operating logic of the ultrasound inspection system type USL SCM 12X.
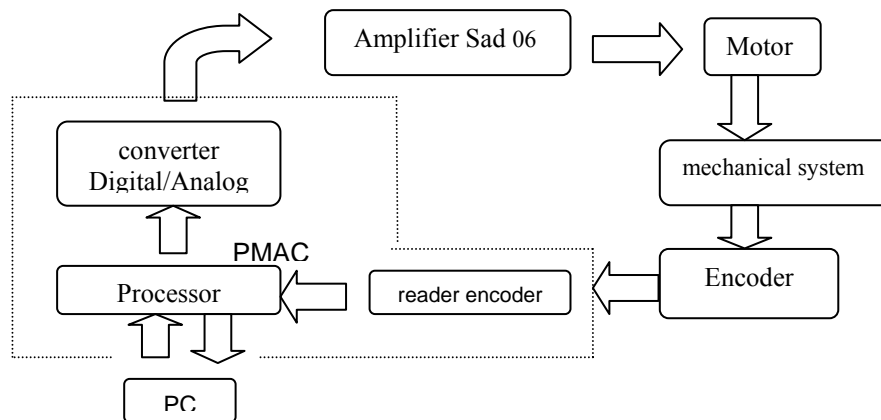
Fig. 1. *Block diagram of scanning –indexing system of the facility - type USL*

Fig.2. *Head transducers, seven unfocused transducers (rectangular) and a focused transducer (circular shape)*

Fig. 3. *Test plate for verifying the accuracy of the scan-indexing system*

The mechanical system allows the movement over X, Y and Z axes. During the inspection of the product (aluminum alloy plate), Z axis position of the transducers head remains constant and is determined by ensuring a certain water path of the ultrasound waves. Moving the transducers head is transmitted by the operator through commands to the PC through a specialized software. The PC sends the command to the digital-analog converter, and the analog signal is sent to the amplifier which drives the electric motor. The rotational movement of the electric motor is converted into translational motion by the mechanical system by means of a pinion-rack mechanism for the X axis, respectively screw-nut mechanism for Y and

Z axes. The position of the transducers head along the axes is measured by the encoders attached to each traveling mechanism. The encoders send the signal under the form [no. pulses / mm] to an encoder reader that processes information for the processor. The processor compares the value of the traveling command with the value received from the encoder and decides whether the reading head has arrived to the prescribed destination or not. Also, if the transducer head detects a discontinuity in the material being controlled, its coordinates are stored by the PC based on the value calculated from the signal of the encoder.

4. Describing the method of assessing the accuracy of the scanning indexing system

From the metrology viewpoint, the scanning-indexing system is part of the equipments for measuring „lengths", a range widely approached by the specialists, but whose conventional methods used for the calibration of „classical" measuring equipment become useless because of the features resulted from the particular combination of dimensional aspects and the ultrasonic transducer issues and also the big system size. To overcome the technical difficulties detailed in Section 2, the authors propose a specific method and procedure for checking the compliance with the applicable requirements[3], and which are characterized by simplicity, very low implementation costs and, last but not least, the reduced measurement uncertainty. The proposed method is based on the evaluation of errors by means of which the transducers system of the facility identifies a specific location of coordinates (X, Y) defined/measured by the mechanical system of the facility traveling within the ultrasonically investigated range, thus combining the electrical-mechanical system measurement performance to travel and identify the scanning head position (see Fig. 2) with the performance of the transducers system to accurately locate a specific disruption of the material being inspected. The novelty introduced by this method is to embed both systems - displacement / measurement system and transducers system - into the whole scan-indexing system.This approach is accounted for by the fact that the final target of the scan-indexing system is to accurately (±2.5 mm, conf. [2], [3]) identify the position of each disruption found in the product under investigation.

5. Budget of uncertainty associated with the method proposed

Preliminary consideration on the budget of uncertainty; the sources of error related to the components of the uncertainty budget associated with the proposed procedure are as follows:

1. errors contained in the coordinate information (i_{iX}, i_{iY}) – such errors shall be assessed by coordinate measurements carried out during the investigation procedure;

2. errors due to operator (i_{op}) – fall within the concept of repeatability and reproducibility;

3. errors of indication (i_{ind}) – they are due to the limited number of decimals as reported by the measurement and the corresponding inherent rounding;

4. errors due to mechanical gears (i_{mec}) – they are due to the order of rack- gear wheel clearance provided by the construction of the scanning-indexing system;

5. errors of positioning (i_{poz}) – refer to the positioning of the transducer head the bottom plate hole whose coordinates are being determined and are influenced by the ratio of hole size and actual size of the ultrasound beam;

6. errors of calibration/standard (i_{etalon}) – they are introduced by the uncertainty known to each dimension represented by the standards used to verify the test plate. The amount of uncertainty is reflected in the standards certificates or in those of the coordinate measuring machine (CMM) which served as reference for the transmission of measuring units;

7. errors due to temperature variation (i_{term}) – the temperature variation determines, by expansion /contraction, dimensional modifications of the test plate. Out of the error sources listed above, i_{ix} and i_{iy} are included into the measurements carried out for inspection purpose, while the error due to temperature variation within the working space is of the order $\alpha_t \Delta_t$, where the heat expansion coefficient for Al $\alpha_t = 23,6 \mu m/(mK)$, and the temperature in the working space is kept within the limits $15° \div 25°C$, which, combined with a maximum plate size of 2500 mm, corresponding to an error not exceeding 0.3mm.

As regards the positioning error i_{poz}, this is a possible error to locate the defect center - which is the order of the defect radius considered, namely 0.6 mm for the minimum defect corresponding to the inspection class A [3]. Errors i_{mec} due to the gear clearance of the scan-indexing system can be assessed as no greater than 10% of the tooth thickness measured on the division diameter, this value being considered no more than 0,4 mm. The error due to the operator must be dissociated from the error to equipment and therefore will not be included into the uncertainty budget of the scanning- indexing system.

The total error for the measurements in the X and Y axes is given by equations (1) and (2).

$$E_X = l_{ix} - l_S + L_S \alpha \Delta t + \delta_{i\,poz} + \delta_{i\,mec} + \delta_{i\,ind} \qquad (1)$$

$$E_y = l_{iy} - l_S + L_S \alpha \Delta t + \delta_{i\,poz} + \delta_{i\,mec} + \delta_{i\,ind} \qquad (2)$$

Table 1 provides briefly the corresponding uncertainty budget equations (1) and (2).

Table 1. *Budget of uncertainty for the scan-indexing system*

Size V_i	Estimate value v_i	Standard Uncertainty $u(v_i)$	Type of Distribution	Sensitivity coefficient c_i	Contribution to uncertainty $u_i(y)$	Type of assessment
i_X	$\overline{i_X}$	s_X	normal	1	$s_X\, c_i$	A
i_Y	$\overline{i_Y}$	s_Y	normal	1	$s_Y\, c_i$	A
i_{etalon}	l_{etalon}	0.006 [mm]	rectangular	-1	0.006 [mm]	B
i_{term}	0	2.04 [K]	triangular	2.5 [m] X 23.6 [µm/mK]	0.120 [mm]	B
i_{poz}	0	0.346 [mm]	rectangular	1	0.346 [mm]	B
i_{mec}	0	0.115 [mm]	rectangular	1	0.115 [mm]	B
i_{ind}	0	0.029 [mm]	rectangular	1	0.029 [mm]	B

In the last column of this table it is indicated the type of evaluation, according to [4], by means of which each component of the budget is estimated.

Thus, the type of assessment A involves determining, by statistical calculations, the standard deviation of that error while for type B the value of the standard uncertainty value is estimated based on the characteristic values and the type of statistical distribution of the error.

6. Description of work procedure

The procedure that makes it possible to implement the method described in Section 3 uses an aluminum alloy plate - similar to products currently under examination with ultrasounds - which was highly accurately processed to become a test plate (see figure 3).
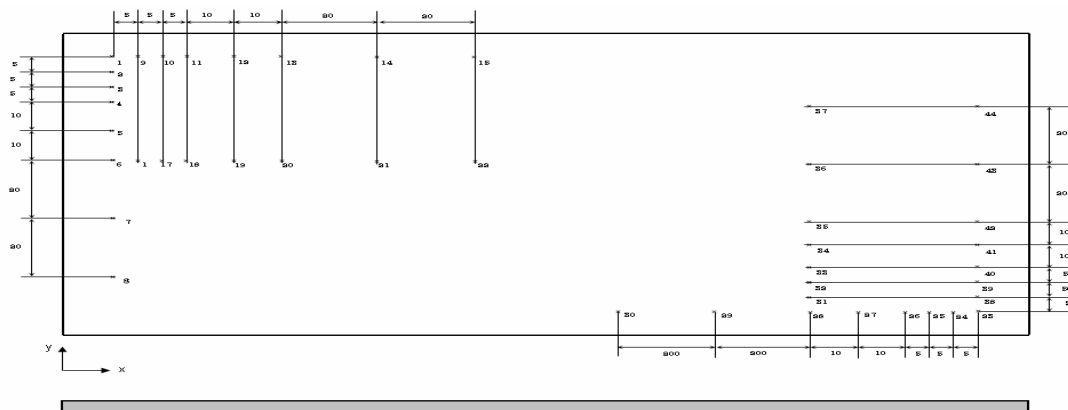
Fig. 4. *Test plate, sized length x width x thickness = 2231mm x 1169mm x 40mm.*

The processes referred to are meant to make discontinuity as flat-bottomed hole (FBH) to the established positions with an accuracy much higher than it is to be evaluated. If the accuracy specified for scan-indexing system is ± 2.5 mm and the coordinate values are provided by the scan-indexing system with a resolution of 0.1 mm, the test card processing with an accuracy of ± 0.01 mm was considered satisfactory. The test plate processing consisted of a series of flat-bottomed holes, arranged in rows and columns, the distances between rows and columns evenly distributed over the measurement range of

scanning and indexing system. These holes are the calibration points needed to assess the accuracy of the scanning – indexing. Processing is done by drilling and boring on a machine tool with a numerical coordinate control (CNC), the depth of the holes being 20 mm and their diameter of 1.2 mm. The choice of the diameter of 1.2 mm corresponds to FBH defect type with maximum size allowed for class A of inspection [4]. Measuring distances between holes is performed by a coordinate measuring machine (CMM) whose measurement accuracy is defined by an expanded uncertainty value of max. ± 0.01 mm. Following these measurements a certificate of calibration for the test plate is drawn up.

After drilling the holes, they are clogged with epoxy resin to prevent water penetration, so as to prevent damage by corrosion of the inner surface of the discontinuity thus created. Test plate is shown in Figure 4. Test plate is immersed into the water tank of the facility to be scanned. The scanning process takes place automatically and includes the defects coordinates as detected by the scanning head.

After completion of the scan, the report is printed, recorded in the facility computer which contains coordinates of all defects detected during the scan operation. These data are compared with the standard values of the calibration of the test plate and the measurement error is obtained by comparing the standard value of the measured value.

6.1. Determining the measuring accuracy

To determine the measuring accuracy it is calculated:

1. The arithmetical average of the errors from the measurements made on each axis of movement X and Y, denoted E_X and E_Y.

2. The standard deviation of the errors obtained by measurements on each movement axis X and Y, denoted s_X and s_Y is calculated.

s_x = standard deviation of the errors from the measurements made on X axis, as expressed by relation (3):

$$s_x = \sqrt{\sum_{i=1}^{n}(x_i - E_X)^2/(n-1)} \qquad (3)$$

s_y = standard deviation of the errors from the measurements made on Y axis, as expressed by relation (4):

$$s_y = \sqrt{\sum_{i=1}^{n}(y_i - E_Y)^2/(n-1)} \qquad (4)$$

3. Calculation of standard uncertainty of the measurement performed with scanning-indexing system for each axis of movement X and Y, denoted by u_x and u_y, where:

$$u_x^2 = s_x^2 + u^2_{ietalon}(x) + u^2_{iterm}(x) + u^2_{ipoz}(x) + u^2_{imec}(x) + u^2_{iind}(x) \qquad (5)$$

$$u_y^2 = s_y^2 + u^2_{ietalon}(y) + u^2_{iterm}(y) + u^2_{ipoz}(y) + u^2_{imec}(y) + u^2_{iind}(y) \qquad (6)$$

4. Calculation of expanded uncertainty of measurement performed with scanning-indexing system for each axis of movement X and Y, for a 95% confidence level, denoted by U_x and U_y by relations (7) and (8):

$$U_X = 1.96\ u_x \qquad (7)$$
$$U_Y = 1.96\ u_y \qquad (8)$$

Note: The accuracy of scan-indexing system is characterized by an extended uncertainty to determine the errors calculated from direct comparison between the test plate and the scan-indexing system.

The inspection conclusion is that the scan-indexing system is „accepted" if U_X < 2.5mm and if U_Y < 2.5mm.

If the calibration result is "rejected" it shall be determined the root cause and necessary corrective actions are taken to satisfy the accuracy requirement.

7. Example of calculation

To give an example, it will be considered verifying the accuracy of the scan-indexing system presented in Section 3, using the proposed procedure.

In this regard, Tables 2 and 3 are used for measurements on the X and Y axes.

The tables are filled in as described below:

- in the first column of tables 2 and 3 it is recorded the point on the test plate that is considered conventional origin for the test points in column 3

- in the second column of Tables 2 and 3 it is recorded the movement axis for which inspection is carried out

- in column 3 of Tables 2 and 3 it is recorded the points where measured lengths are compared to the standard ones.

- in column 4 of Tables 2 and 3 it is recorded the values measured by the scan-indexing system between the points recorded in the 3rd column

- in column 5 of Tables 2 and 3 it is recorded the standard values from measuring the test plate by means of the coordinate measuring machine (CMM).

- in column 6 of Tables 2 and 3 it is recorded the errors values calculated by discounting the standard value from the measured value.

- in column 7 of Tables 2 and 3 it is recorded the values of the extended uncertainty obtained by multiplying the standard uncertainty by 1.96.

It is calculated the arithmetic average of the errors obtained from the measurements made on X axis:

$$E_X = 0.012 \text{ mm.} \qquad (9)$$

Table 2. *Values of the measurements carried out for X axis*

Conventional origin point	Inspected axis	Length between points	Measured value [mm]	Standard value [mm]	Error [mm]	Extended uncertainty [mm]
1	X	1÷16	50.00	50.00	0.00	1.166
		16÷17	50.00	49.97	0.03	
		17÷18	50.00	49.99	0.01	
		18÷19	100.00	99.98	0.02	
		19÷20	100.00	99.96	0.04	
		20÷21	200.00	199.98	0.02	
		21÷22	200.00	199.99	0.01	
		5÷9	50.00	50.00	0.00	
		9÷10	50.00	49.98	0.02	
		10÷11	50.00	49.97	0.03	
		11÷12	100.00	99.98	0.02	
		12÷13	100.00	99.97	0.03	
		13÷14	200.00	199.96	0.04	
		14÷15	200.00	199.97	0.03	
23		29÷30	200.00	199.99	0.01	
		28÷29	200.00	200.01	-0.01	
		27÷28	100.00	100.02	-0.02	
		26÷27	100.00	100.01	-0.01	
		25÷26	50.00	50.00	0.00	
		24÷25	50.00	50.00	0.00	
		23÷24	50.00	50.02	-0.02	

It is calculated the arithmetic average of the errors obtained from measurements made on the Y axis:

$$E_Y = -0.003 \text{ mm.} \qquad (10)$$

It is calculated the standard deviation of the errors obtained from the measurements made on X-axis, expressed by relation (3)

$$s_X = 0.018 \text{ mm.} \qquad (11)$$

Table 3. *Values of the measurements taken on Y axis*

Conventional origin point	Inspected axis	Length between points	Measured value [mm]	Standard value [mm]	Error [mm]	Extended uncertainty [mm]
1	Y	1÷2	50.00	50.00	0.00	1.156
		2÷3	50.00	50.00	0.00	
		3÷4	50.00	49.99	0.01	
		4÷5	100.00	100.00	0.00	
		5÷6	100.10	100.05	0.05	
		6÷7	199.90	199.94	-0.04	
		7÷8	200.00	200.00	0.00	
		23÷38	50.00	50.01	-0.01	
		38÷39	50.00	50.02	-0.02	
		39÷40	50.00	50.00	0.00	
		40÷41	100.00	99.98	0.02	
		41÷42	100.00	100.04	-0.04	
		43÷44	200.00	199.98	0.02	
		37÷36	200.00	199.99	0.01	
23		36÷35	200.00	199.98	0.02	
		35÷34	100.00	100.04	-0.04	
		34÷33	100.00	100.03	-0.03	
		33÷32	50.00	49.99	0.01	
		32÷31	50.00	50.01	-0.01	
		31÷27	50.00	50.01	-0.01	

It is calculated the standard deviation of the errors obtained from the measurements made on *Y* axis, as expressed by relation (4):

$$s_Y = 0.023 \text{mm} \qquad (12)$$

The standard uncertainty for the measurements made on X axis is expressed by relation 5:

$$u_x^2 = 0.018^2 + 0.006^2 + 0.170^2 + 0.346^2 + 0.115^2 + 0.029^2 = 0.144 \, [\text{mm}^2] \quad \text{or} \quad u_x = 0.380 \, [\text{mm}]. \qquad (13)$$

The extended uncertainty for the measurements made on X axis is expressed by relation 7:

$$U_x = 1.96 \, u_X = 1.96 \times 0.380 \, [\text{mm}] = 0.745 \, [\text{mm}] < 2.5 \, [\text{mm}] \qquad (14)$$

It follows that the scan-indexing system meets the accuracy requirement for the movement axis *X*.

The standard uncertainty for the measurements made on Y axis is expressed by relation (6):

$$u_y^2 = 0.023^2 + 0.006^2 + 0.170^2 + 0.346^2 + 0.115^2 + 0.029^2 = 0.144 \, [\text{mm}^2] \quad \text{or} \quad u_y = 0.380 \, [\text{mm}]. \qquad (15)$$

The extended uncertainty for the measurements made on *y* axis is expressed by relation (8):

$$U_y = 1.96 \, u_Y = 1.96 \times 0.380 \, [\text{mm}] = 0.745 \, [\text{mm}] < 2.5 \, [\text{mm}] \qquad (16)$$

It follows that the scan-indexing system meets the accuracy requirement for the movement axis *Y*.

8. Conclusions

The proposed method and procedure have a number of features that were highlighted, at least in terms of key issues, in Sections 2-7 of this paper. Thus, a number of conclusions may be drawn with respect to the method and procedure proposed herewith.

a).The budget of uncertainty associated with the proposed method is richer than the usual one in that it includes the source of errors due to detection of calibration points by the ultrasonic transducers.

b).The procedure is based on measuring the relative position of calibration points, thus avoiding the additional uncertainties related to the origin of the facility axes system.

c).The performance obtained by applying the procedure is influenced by the accuracy of the location of the test plate in the immersion tank, parallel to the facility coordinate axes. In practice, this positioning is achieved by exploiting the constructive elements of the immersion platform and is corrected by making a preliminary scan of the test plate, after which the plate outline is visible on the facility screen.

Location correction is performed so that the contour of the plate test is straight (not stepped) and clear (no shadows).

d).The costs incurred by the proposed procedure are limited to cost of test plate, the labor of scanning, uncertainty calculation and editing the verification certificate. Given that the test plate can be made from a scrapped plate for discontinuities and other internal defects that more often than not, organizations that operate such equipment have the processing capacity required, these costs are much lower than those of verification by an external provider.

e).The proposed procedure and the results of its implementation have been considered acceptable by all NADCAP auditors and all customers who assessed it on the occasion of the audit at ALRO SA Slatina.

Summarizing the foregoing, it can be stated that the proposed procedure and implicitly the method this is based on, are simple and reasonably accurate, practical and inexpensive, which recommends then for industrial practice.

References

[1]. **Taylor, Barry, N, Kuyatt, Chris E**.- NIST Technical Note 1297, *Guidelines for Evaluating and Expressing the Uncertainty of NIST Measurement Results,* National Institute of Standards and Technology, Gaithersburg, Edition 1994.

[2]. * * *, AC 7114-3 Rev. E - *Nadcap audit criteria for nondestructive testing facility ultrasonic survey,* Performance Review Institute, 2009.

[3]. * * * , AMS-STD 2154 - *Inspection, Ultrasonic, Wrought Metals, Process For,* SAE International, 1998 (Reaffirmed 2005)

[4]. * * * , SR ENV 13005, *Ghid pentru exprimarea incertitudinii de măsurare,* Asociația de Standardizare din România (ASRO), 2003.

[5]. * * *, EN 12668-3 - *Non-destructive testing - Characterization and verification of ultrasonic examination equipment - Part 3: Combined equipment,* European Committee for Standardization, 2000.

[6]. **Picu, M., Tudose, C., Picu, A**. - *Factori care influențează rezultatele examinărilor ultrasonice*, 6th COMEFIM Conference on Fine Mechanic and Mechatronic, COMEFIM'6 2002, Romania, Brasov, 10-12 October 2002.

TRIBOLOGICAL PROPERTIES OF COMPOSITE MATERIALS OBTAINED USING ELECTRODEPOSITING

[1]**Raul NOVAC,** [1]**Petrica ALEXANDRU,** [1]**Alina CANTARAGIU,**
[2]**Alexandru STĂNCIOIU**
[1]"Dunărea de Jos" University of Galati
[2]S.C. ALRO S.A. Slatina
email: raul_novac@yahoo.com

ABSTRACT

The resistance to abrasive wear of composite materials obtained using electrodepositing in nickel and copper matrix was studied. The samples containing composite layers of graphite in copper matrix, titan dioxide and zirconium dioxide in nickel matrix were subjected to the wear process using a pin-disc type testing machine.

KEYWORDS: composite coating, tribological properties

1. Introduction

The tribology concept refers to the interaction between two or more bodies with one or more surfaces in contact, with or without macroscopic relative motion, in order to transmit normal or tangential forces. The process of friction-wear is a complex one, producing modifications in the geometry and structure of the superficial layers that are in contact with each other; this phenomenon leads to losses of material reducing the precision and the efficiency of machines and tools. In the automotive industry there are many parts affected by the wear which leads to the replacing of the traditional materials with composite materials (table 1).

Table1. *The use of composite materials in the automotive industry [1]*

System	Components	Improved Properties
Engine	Piston head; valve; piston bolt; rod; bearings	Resistance to high temperatures; weight; wear
Housing	Gearbox bearings	Weight; wear
Brake	Brake Disc	Weight; wear
Suspensions	Strut	Rigidity; resistance to wear

Good tribological properties are also seen in the case of composite coverings with metallic matrix obtained using electrodepositing; in the case of these composite materials the properties of the metallic matrix are improved by adding the disperse phase that is under the form of powder.

2. The experimental method

We studied the tribological behavior of many samples made using electrodepositing.

Table 2. *Characterization of samples depending on the nature of matrix and dispersed phase*

Sample	Matrix	Dispersed phase, (DP)	DP in the composite layer (%)	Layer thickness (μm)
G 25	copper	graphite	5	19
G40	copper	graphite	6	20
T35	nickel	TiO_2	11	18
T67	nickel	TiO_2	12	20
Z21	nickel	ZrO_2	7	30
Z45	nickel	ZrO_2	8	35

We deposited TiO_2 and ZrO_2 in nickel matrix and graphite in copper matrix. The size of the TiO_2 and ZrO_2 dispersed phases was 2-5µm and 8-15µm for graphite. All the electrodeposits were made on a copper basis.

The technological scheme was the following one: *Electrodepositing, Drying, Punching, Degreasing, Abrasive wear resistance testing.*

Fig. 1. *The microstructure of the sample G 40 before the wear testing (the basis is made of copper, matrix of copper and graphite is the dispersed phase)*

Fig. 2. *The microstructure of the sample T67 before the wear testing(the basis is made of copper, matrix of nickel and TiO_2 is the dispersed phase)*
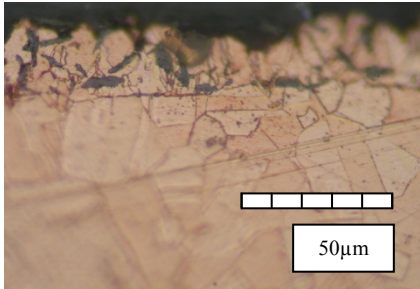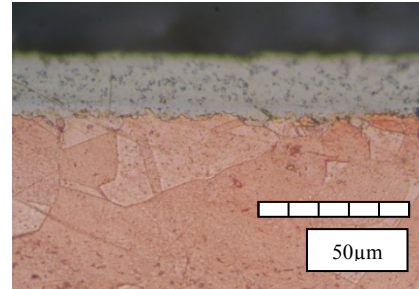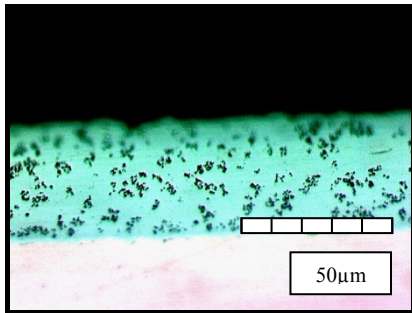

Fig. 3. *The microstructure of the sample Z45 before the wear testing (the basis is made of copper, matrix of nickel and ZrO_2 is the dispersed phase)*
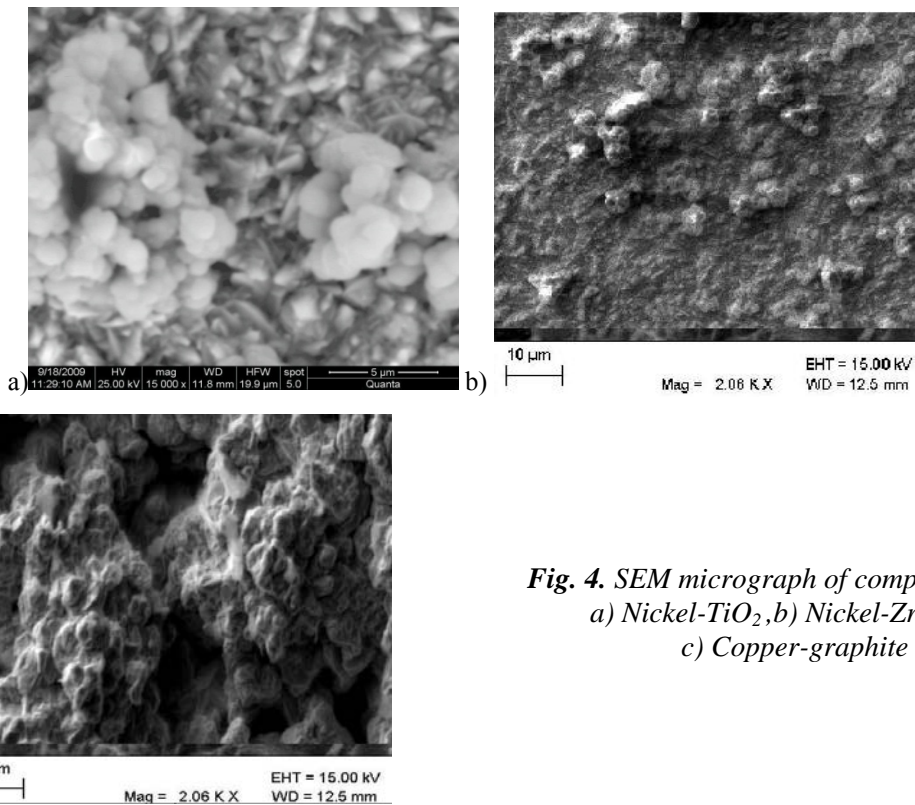

a)

b)

c)

Fig. 4. *SEM micrograph of composite layers: a) Nickel-TiO_2 ,b) Nickel-ZrO_2 and c) Copper-graphite*

2.1 Abrasive wear resistance testing

The machine used in order to check the abrasive wear resistance is a pin-disc type one. The sample is introduced in a puncher that presses with a certain force upon a rotating disc covered with abrasive paper (600 granulation). The sample executes a spiraling motion on the disc with the help of a mechanism. All the samples were pressed against the disc with the same force and have traveled the same distance. At the end of the testing the mass loss of each sample was measured. The variation of the mass was established by weighing with a scale with the precision of 1×10^{-3} grams.
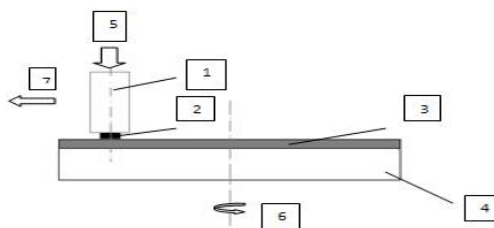
Fig. 5. *The scheme of the abrasive wear resistance testing machine: 1. puncher, 2. sample, 3. abrasive paper, 4. metallic disc, 5. pressing force, 6. the rotation movement of the disc, 7. the movement of the sample on the disc.*

3. Results and discussions

For the wear testing we used samples with a disc shape with a diameter of 10 mm. The pressing force was made using the weight of the puncher, respectively 126 grams. The length of the distance traveled trough each sample was 7.5 m. We used samples obtained by the electrodepositing on a copper basis. We have measured the mass of the sample before and after the wear testing. The results are presented in table 3 and figure 6.

Table 3. *The variation in mass of the samples after the wear testing*

No.	Sample	Δm (g/m)
1	G25	0.0014
2	G40	0.0011
3	T35	0.00096
4	T67	0.00092
5	Z21	0.00073
6	Z45	0.00069
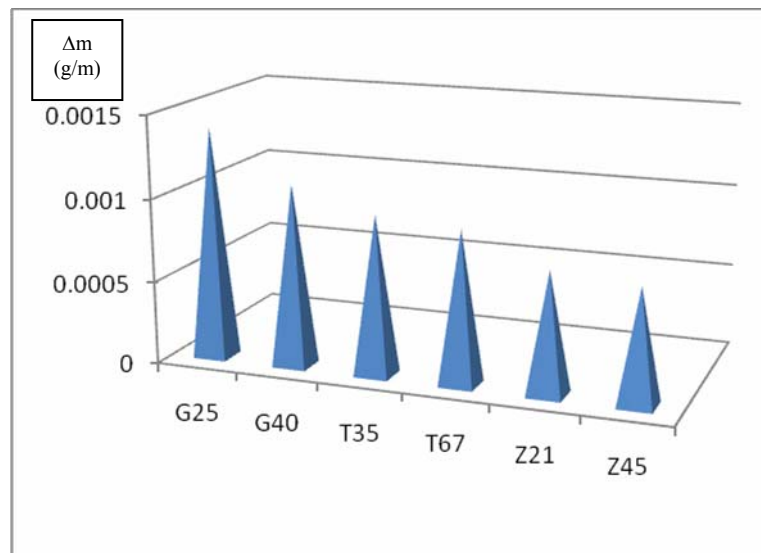
Fig. 6. *The variation of the mass of the samples according to the depositing type*

It can be noticed that the nickel- ZrO_2 layer have the best wear resistance. The wear resistance of each layer depends on the percentage of embedded particles and micro-hardness of the particles.

4. Conclusions

The paper presents some results obtained following an extensive experimental research program on the application of technology for the composites by electrodeposition. Single layers were deposited into a matrix of copper and nickel using copper as a support and TiO_2, ZrO_2, graphite as the dispersed phases. The nickel + ZrO_2 samples (Z45, Z21) have shown the best resistance to wear; more intense wear was noticed in the case of the samples T_{67} and T_{35} (Ni+TiO_2) and the maximum wear was in the case of the samples G_{40} and G_{25} (Cu + graphite). Different

wear behavior can be explained by the fact that deposited layers have different micro-hardness; matrices are also different (nickel with higher wear resistance than copper).

References

[1]. C.Stefanita, Eng.M. Mangra - *Actual tendencies in the usage of composite materials in the automotive industry*, 8th International Conference Targu-Jiu, May 24-26, 2002, "Constantin Brâncusi" University, Engineering Faculty;

[2]. O. Mitoseriu, E.Drugescu, F. Potecasu, L. Benea, G.Carac - 1998, *Composite Coatings Obtained by Sedimentation Co-deposition During Copper, Cobalt* and Iron Electroplating - International Journal Materials and Manufacturing Processes, Vol XI, pages 417-422;

[3]. S.R. Saifulin - *Physical Chemistry of Inorganic Polymeric and Composite Materials*, Ellis Horwood Ltd. London, New York, 1992;

[4]. J.P. Celis - *Developments and future challenges to science and technology in the field of tribo-corrosion*, Proc. Eurocorr 2005, The European Corrosion Congress, 4-8 September 2005, Lisbon, Portugal;

[5]. A. de Vooys, J.P. Celis - *Tribological and electrical performance of composite nickel and copper coatings as connector material on steel strips*, Appliance Manufacturing, pages: S. 48 ff., jan. 2004.

THE JOHNSON-MEHL-AVRAMI MODEL APPLIED TO MARTENSITIC KINETICS IN AUSFORMED COOPER BASED SHAPE MEMORY ALLOY

CARMELA GURAU[1], GHEORGHE GURAU[1],
Francisco Manuel BRAZ FERNANDES[2]
[1]Faculty Metallurgy, Materials Science and Environment, "Dunărea de Jos" University of Galaţi, Romania,
[2]CENIMAT/Materials Science Department, Nova University of Lisbon, Caparica, Portugal
email: gheorghe gurau@ugal.ro

ABSTRACT

CuAlNi shape memory alloys which are used as sensors and actuators have also been investigated recently as materials for medicine devices. This study shows the influence of the thermo – mechanical treatments in CuAl13Ni4 shape memory alloy on martensitic transformation kinetics and microstructures. While maintaining a constant 20% degree of deformation, deformation temperature was varied between 800˚C and 1000˚C. The alloy was investigated by differential scanning Calorimetry (DSC) and optical microscopy. The validity of JMA model to the kinetics analysis was checked. The changes in the microstructure and kinetic transformations have been linked to the evolution of the rolling temperature that introduced high density dislocations in initial phase and changes fraction and interaction between the $\beta_1{}'$ (18R) and $\gamma_1{}'$ (2H) martensite coexisting in this shape memory alloy.

KEYWORDS: shape memory alloys, medicine devices, deformation

1. Introduction

Shape memory alloys belong to a class of so called smart material due to their unique properties of remembering the initial and cold shape. The shape modification is accounted on reversible, thermo-elastic transformation of the martensite. The martensitic transformation is a solid state heterogeneous transformation, produced not by diffusion but by atom displacement over smaller distances than the diffusion jump. Cu based SMAs, especially Cu-Al alloyed with Ni or Mn are commercially available. The temperatures characteristic to the martensitic transformations inside CuAlNi alloys are within the range -200 to +200 ˚C and depend on the content of Ni and Al. Cooper based systems were once the most attractive for industrial applications because of less difficult melting, cast and composition control, better stability of the two-way shape memory and not at least because of their lower costs as compared with the most popular Ti-Ni SMAs [1]. CuAlNi shape memory alloys have also been investigated recently as materials for medicine devices [2]. The main reason for studying the kinetics of thermo - mechanical treated cooper based SMAs

comes from engineering, from necessity to produce those alloys as finished products with defined memory proprieties and also good mechanical characteristics. Thermo – mechanically treatments provide ways to achieve those properties. Also sensor and actuator applications, in many cases, require high transformation temperatures and good thermal stability. Thermo-mechanical treatments represent a set of operations of plastic deformation, heating and cooling – made in certain sequence – and as a result of the final structure of the metallic material take place in a high density of lattice defects, associated with plastic deformation. In the case of SMA, the thermo-mechanical treatment involves plastic deformation of austenite (β). Through this plastic deformation at heating are introduced certain defects which will cause the change of the martensitic transformation parameters [3-4]. This study shows the influence of crystallization kinetics of the thermo – mechanical treated CuAl13Ni4 shape memory alloy.

2. Experimental research

The research program has used extruded wires of 4 mm in diameter, Cu Al Ni shape memory alloy

prepared by classical methods at Dunarea de Jos University of Galati. The extruded samples of 4 mm diameter have been heated in a vertical furnace type Nabertherm for 30 min. at 850 ˚C. The samples have been introduced into the furnace at the solubilization temperature. After heating they have been hot rolled on a double reversible rolling mill. Those samples have been hot rolled in tree successive passes up to 2.6 mm thickness. The specimen had been thermo-mechanically treated at 1000˚C, 950˚C, 900˚C, 850˚C, 800˚C and has been deformed with 20% deformation degree and cooled in the same conditions. The samples were noted as A1, A2, A3, A4 and A5.

The plastic deformations were done on a duo reversible rolling mill, home made, in one pass. The heating furnace was placed in front of the rolling mill.

The sample route has been protected by the ceramic tube.

The loss of heat through radiation is limited, aspect that posed more problems as the rolled sample thickness decreased. The rolling cylinders were preheated with methane gas burner.

The high thermo-mechanical treatment domain limits for the Cu Al Ni alloy were fixed according to the melting temperature and the minimum temperature was chosen to have no cracks in the sample.

$800˚C \leq T < T_{melting}$

The ausforming temperature was chosen in near high and low domain limit where the austenite is stable.

After rolling the subsequent quenching is essential. It can be considered that the alloy leaves the rolling mill at about the same temperature at which it entered to do adiabatic heating.

2.1 Analysis by Differential Scanning Calorimetry

The samples were analyzed by DSC. Differential Scanning Calorimetry was used to characterize the thermal effects associated with the direct and reverse martensite transformation. For DSC measurement were used small pieces weighting less than 0.100 g.

The differential calorimetric experiments were performed by means of SETARAM 92 instrument in air at a heating and cooling rate of 10˚C/min between -50˚C and 200˚C.

The cooling treatment was acted by using liquid nitrogen. Endothermic and exothermic peaks on DSC profiles were taken from two consecutive thermal cycles. Prior to the investigation the specimen was etched in 1:1 HNO3 solution in water.

The attack was seen as necessary for removing distortions that cut the oxide layer.

The martensite and austenite start and finish temperatures (Ms, Mf, As, and Af) were obtained using the base line method.

2.2 Microstructure characterization method

Optical specimens were prepared using standard methods. A color solution Klemm's III was used to etch CuAlNi alloys.

An Olympus microscope with digital image analysis system was employed to study martensite morphology and to characterize the thermo-mechanical effect on the microstructure.

3. Results and discussion

DSC measures the amount of energy absorbed or released by a sample when it is heated or cooled, providing quantitative and qualitative data on endothermic (heat absorption) and exothermic (heat evolution) processes. DSC methods are quite popular for crystallization kinetics analysis where nucleation and growth mechanisms are involved. The crystallization behavior is determinated by kinetics parameters. Jhonson-Mehl-Avrami (JMA) model is valid for isothermal and isochronal transformation. In non isothermal cases the validity is enssured by a rate transformation which depends exclusively on temperature and the degree of deformation, but not on the thermo mechanical history [5].

This paper aims at setting temperature limits at which, the martensitic transformation taking place in the ausformed samples the JMA model can be applied. Germination and growth were studied by Jhonson-Mehl-Avrami model:

$$y = 1 - e^{-kt^n} \tag{1}$$

Where: y is the transformed volume fraction, k is the reaction rate constant, independent of time but temperature dependent and related mechanism of constant transformation ($k=k_0e^{-E_a/RT}$, t the transformation time, n called Avrami exponent, a constant related to the behaviors of nucleation and growth). The transformation fraction y in a giving time during isochronal transformation is determined by measuring the corresponding partial area of the endothermic and exothermic DSC processed peaks.

The above equation becomes:

$ln (1-y)=-kt^n$ respectively $ln [-ln (1-y)]=ln k+n lnt.$

$$\tag{2}$$

The value of Avrami exponent n and the reaction constant k can be calculated from the slope straight line obtained by plotting $ln(-ln(1/1-y))$ vs. $ln(dt)$. While maintaining a constant degree of deformation, deformation temperature was varied between 800˚C and 1000˚C. The DSC processed plots are illustrated in Fig.1.

There is a good stability of critical points with a slight downward trend by the upper interval temperature chosen (Fig.2.). The critical temperature point martensite finish ranges around 80˚C flourishing trend of increasing rolling temperature at 1000˚C. By ausforming at 900˚C, the critical point M$_s$ undergoes a significant decrease compared to samples thermo-mechanically treated at other temperatures, the breakpoint value was located at 67˚C.

The critical transformation points austenitic finish remains stable at about 160˚C, for all the samples plastically deformed with 20% and quenched subsequently.
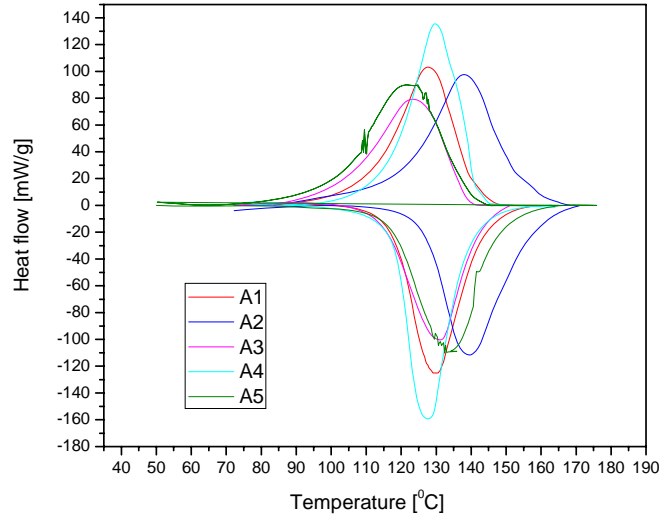
Fig.1. *The DSC curves for thermo mechanical by treated samples with 20% degree of deformation, from austenitic temperature 1000˚C-A1 980˚C-A2, 900˚C-A3, A4-850˚C, respectively 800˚C-A5*

Fig.2. *Variation of reverse martensitic transformation critical points for the samples subjected to thermomechanical treatment*

Fig.3. *Reverse martensitic transformation kinetic curves for samples deformed with the same degree of deformation at different temperatures*

The Reaction Mechanism of the reversible martensitic transformation alloy thermo-mechanically treated at different temperatures follows the model of deformation Jhonson-Mehl-Avram (JMA). Most of them have the classical sine transform both direct and reverse martensitic transformation at cooling and heating. Figures 3 and 4 are the kinetic curves for samples deformed with a deformation degree of 20% at temperatures ranging from 1000˚C to 800˚C.

With one exception represented by alloys deformed under low temperature condition, other curves are grouped in the range of phase transformation temperatures in the range of 100˚C to 170˚C. Ausforming alloy after the same degree of deformation of 1000˚C to 850˚C shows a sine curve and emphasizes the processes of nucleation and growth.

The sample deformed at 850˚C has a linear transformation which no longer fits with Avrami exponent determined by kinetic type used for analysis. The first stage is a linear increase followed by an inflection point at which the slope decreases. The kinetic plot curves for the transformed volume fraction highlight that for the sample deformed at 850˚C the slope is the largest achieved.
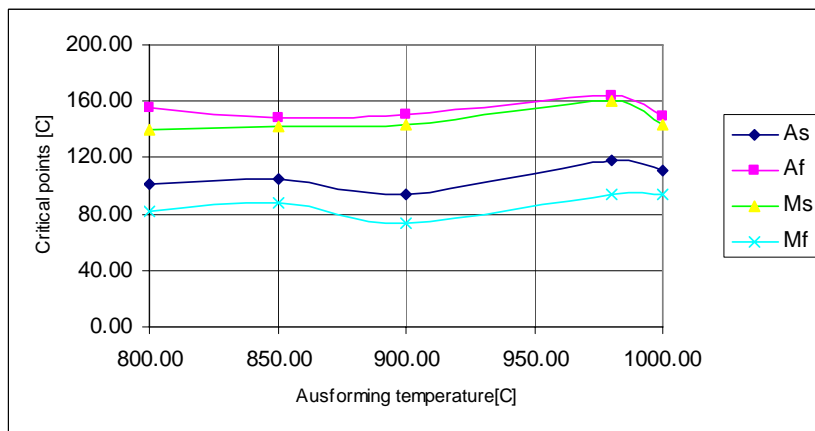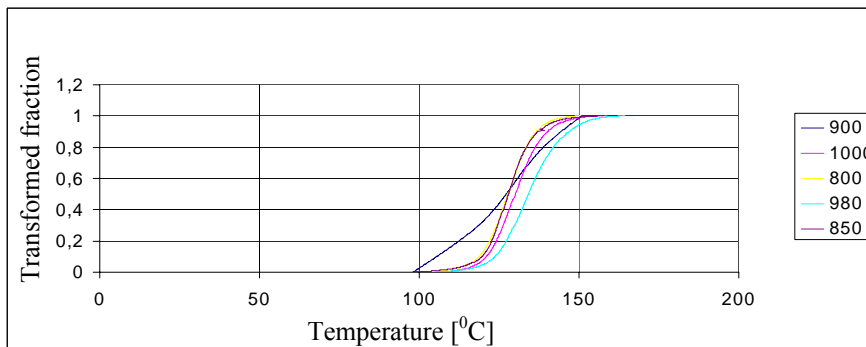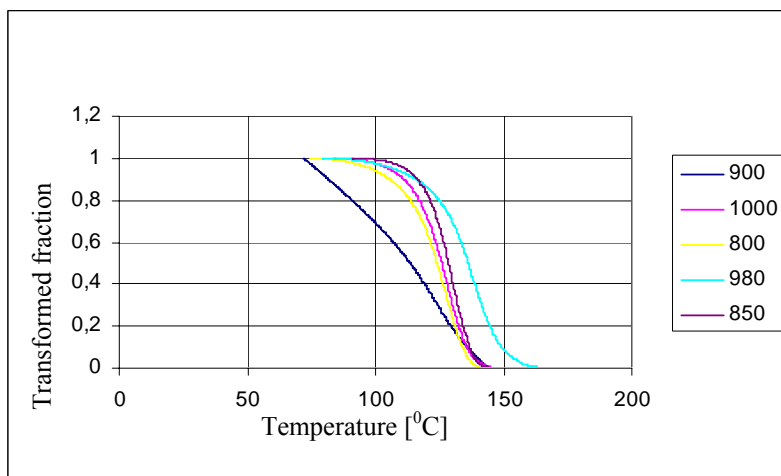

Fig.4. *Forward martensitic transformation kinetic curves for samples deformed with the same degree of deformation at different temperatures*

JMA fits with constant kinetic parameter n, E_a and k_0 is only applicable for the extreme cases where pure continues nucleation or pure site saturation prevails. Reversible martensitic transformation is considered site saturation because of the number of supercritical nuclei which occurs in the first moment of transformation (t=0) and does not change during the transformation [6, 7, 10, 11]. The martensite crystals is growing up instantaneous, probably the germination are based on statistical composition fluctuation and crystal defects especially dislocation introduced by ausforming in initial phase.

Thermo mechanical treatments applied in emperature interval 1000˚C and 850˚C allows for transformation analysis based on JMA model with minimum error. Fig.5 shows plot $\ln(-\ln(1/1-y))$ vs. $\ln(dt)$ using the data for transformed volume fraction between 15%-85% at different rolling temperatures. A slight deviation from linearity is provided by interactive double nucleation $\beta_1{}'$ monoclinic type martensite (18R) and type $\gamma_1{}'$ orthorhombic (2H) coexisting in CuAlNi alloys.
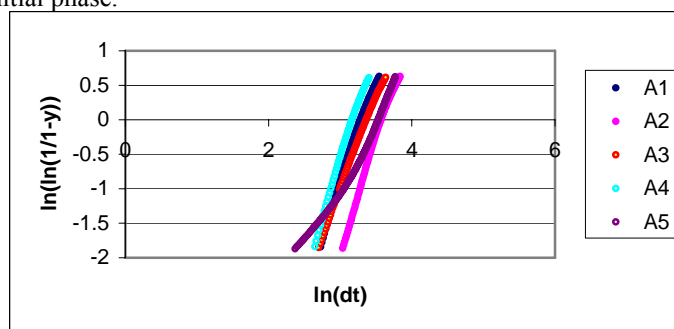
Fig.5. *Isochronal JMA plots of forward martensitic transformation of thermo mechanical treated $CuAl_{13}Ni_4$ samples at different rolling temperature and 20%deformatin degree*

The simultaneous nucleation and their mutual interaction affected complete forward martensitic transformation [6-7]. Ausforming from 800°C does not respect the condition of pure site saturation being an intermediate case and JMA model fits in much higher error.

3.2 Microstructural analysis of thermo-mechanically treated CuAlNi samples

As it is well known, CuAlNi alloys exhibit by quenching or stress-induced, a first-order diffusionless martensitic reverse transformation such as:

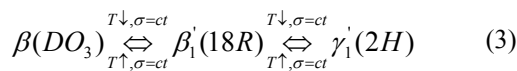$$\beta(DO_3) \underset{T\uparrow,\sigma=ct}{\overset{T\downarrow,\sigma=ct}{\Leftrightarrow}} \beta_1'(18R) \underset{T\uparrow,\sigma=ct}{\overset{T\downarrow,\sigma=ct}{\Leftrightarrow}} \gamma_1'(2H) \qquad (3)$$

The starting point of most direct martensitic transformation is the initial phase (austenite) a solid solution generally denoted β. Elementary cell of this phase for Cu Al Ni obtained by annealing treatment has cubic symmetry, DO3 type. Complex ordering DO3 structure is initially obtained by substituting atom in the center of basic cell and then increasing the degree of ordering by replacing two atoms of two parallel sides of the cube which are on opposite corners of it, but not parallel diagonal. Thus the atoms of a species are isolated among them and raise very different packing possibilities.

The initial phase β, a solid solution based on the electronic component Cu_3Al by rapid cooling undergoes a martensitic transformation. The β_1 martensite has a monoclinic structure with packing orders 18R. It is a typical structure of martensite with a coarse needle zigzag occuring even after plastic deformation by hot extrusion. On this martensite germinate orthorhombic orders, 2H packing. Orthorhombic martensite plate looks thick alternating with thin plates. For this particular alloy composition the presence of the both martensitic phases is simultaneous.

The main purpose of these experiments is to obtain fine structure by thermo mechanical treatments applied to designing sensors and actuators with this shape memory alloy family. Variation of thermo mechanical treatment parameters, temperature - degree of deformation leads to specific structures reversible martensitic transformation with different grain size and two types martensitic structure coexisting in different proportion.

Optical microscopy of samples after quenching reveals two types of martensite reverse, namely β_1, monoclinic type of martensite (18R) and type γ_1' orthorhombic (2H). Monoclinic martensite morphology is a typical zigzag and the orthorhombic type martensite is laths.

The hot plastic deformation morphology of the two types of thermoelastic martensite is enriched with forms described as:
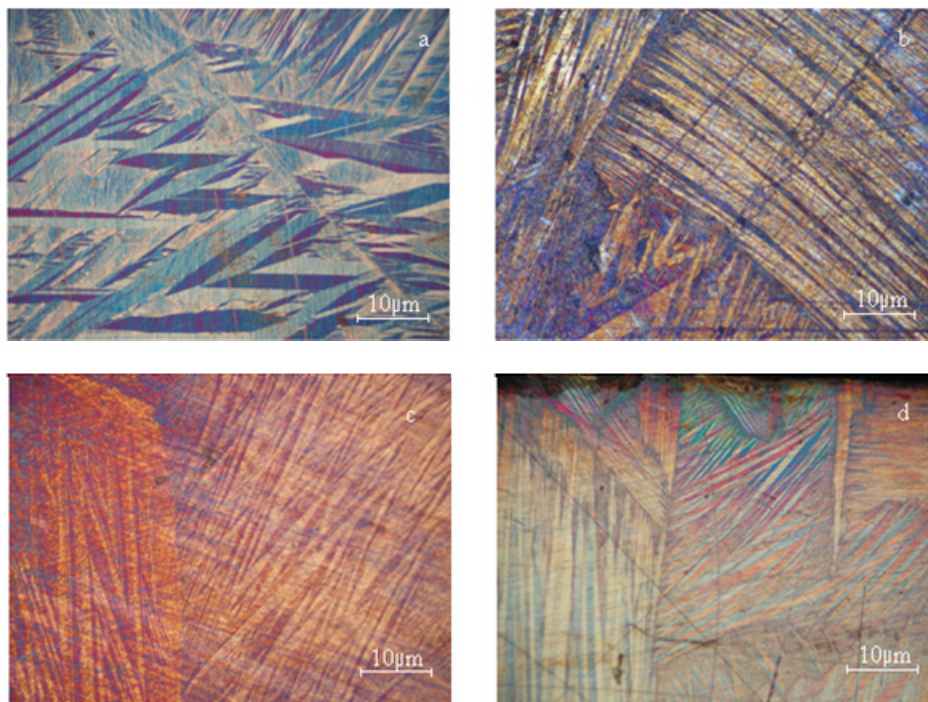• Parallel plates
• Saw
• Small arrow
• Large arrow

Fig. 6. *Optical microstructures $CuAl_{13}Ni_4$ alloy after ausforming with 20% deformation degree, from temperature: a-1000˚C, b. 980˚C, c 850˚C, d 800˚C. Metallographic Attack Klemm's III.*

The parameter that was varied in the thermo mechanical treatment was the rolling temperature which had values between 1000˚C and 800˚C. The metallographic structure, highlights the finishing of the initial grain shape and the martensitic needles are oriented to a perpendicular direction to rolling direction. This aspect is more evident with the decrease in the deformation temperature. The proportion of monoclinic martensite (fig.6.a) decreases with decreasing temperature as a share of the rolling condition. Specific fine structure of lath martensite typical orthorhombic accompanied by numerous packing defects is found in cold-rolled samples (fig.6.c). Metallographic observation for samples after rolling at 1000˚C temperature and 20% degree of deformation shows specific martensite shapes: small arrowhead, arrowhead large, parallel plates and saws. Long-range order structure is maintained. The initial grain size is rough. Specific to the degree of deformation in the boundary grain is occurring of very fine structures and short needles that make the transition to the next seed grain martensitic phase which germinated. Grain boundaries are polygonal, have smooth and regular shape. Decreasing temperature leads to a decrease in grain size. The martensitic microstructure morphology highlights mostly small arrowheads and those become finer. The grain boundaries of the initial phase lose their smoothness and start to fringes, packing more obvious defects.

Plastic deformation achieved at low temperatures (800^0C and 850^0C) leads to untypical curved martensite grown on the perpendicular rolling direction (fig.7). Explaining the formation of very fine martensite curves is attributed to how the germination and growth of martensitic crystals take place. The previous experiments highlighted that although two-dimensional centres of crystallization are formed in the nodes of the dislocations they are not growing. Martensitic curved plate growth occurs between individual dislocations and dislocations networks. Their expansion is hampered by the grain boundary and sometimes by sub grain boundary [4]. At low temperature of deformation a fine scale martensite originates. The size is limited by the dimension of the deformed initial grain. Grain boundaries are never crossed by martensite needles or curved plate, but sub boundaries are. Thermo mechanically treated samples at 850^0C with 20% deformation degree show fine primer cracks.

The monoclinic to orthorhombic interacting nucleation had been carefully observed by the forward study only for quenched and stress induced martensitic transformation [7]. Due to this interaction, the martensitic nucleation is strongly affected throughout the cooling process, leading to very different crystal microstructures.

The result observed in both cases in thermal and stress induced MT concludes that proportion of monoclinic and orthorhombic martensite strongly depends on very local nucleation conditions.

Fig. 7. *Optical microstructures $CuAl_{13}Ni_4$ alloy after ausforming with 20% deformation degree, from 800˚C. Curved martensite*

It was ascertained lack of reproducibility of any crystal property throughout the transformation process. Some authors take for granted that aging in the parent phase favors the formation of $\gamma_1^{'}$ phases [8]. In this study of ausforming a β cooper based alloy through the process introduced a high default density before transformation. Ausforming at selected temperatures did not change the bulk nature of the martensitic reaction. The changes in the deformation temperature have been linked to the slight evolution of the critical martensitic transformation points, different fraction of monoclinic and orthorhombic martensites and grain size. At this amount of deformation a martensite reorientation takes place, based on massive network dislocation introduced in initial phase that maintains a state of tension more pronounced as the deformation temperature approaches the instability of austenite.

From microstructure observation, it is seen that $\beta_1^{'}$ (18R) and $\gamma_1^{'}$ (2H) martensite phases coexist at different fractions also in the thermo mechanical state at different temperatures rolling. The most obvious effect of the dropping deformation temperatures are the increasing fraction of orthorhombic martensite. According to a recent study this result indicates that the conditions of ausforming cause changes between two types martensite coexisting in alloy, and additional transformation $\beta_1^{'}$ to $\gamma_1^{'}$ occurs during the ausforming at temperatures lower than 900˚C[7,9].

4. Conclusions

1. The JMA model can be valid in isochronal reverse martensitic transformation kinetics showing that nucleation is completed before the beginning of the reaction.

2. Kinetic curves plotted for the alloys studied are specific to the JMA model; curves have the classical sine wave.

3. Points of shape memory alloy transformation $CuAl_{13}Ni_4$ and kinetic curves have been determined with minimum error using JMA model.

4. Transformation points (M_f, M_s, A_s, A_f) vary depending on the parameters studied of thermo mechanical treatments applied.

5. Kinetic curves of ausforming samples at the same degree of deformation are grouped with critical temperatures approximately constant.

6. The mechanism of reversible martensitic transformation follow the Jhonson –Mehl- Avrami model also for thermo-mechanically treated alloy not only for quenched samples.

7. $\beta_1^{'}$ (18R) and $\gamma_1^{'}$ (2H) martensite phases coexist at different fraction also in the thermo mechanical state at different rolling temperatures. The most obvious effect of the dropping deformation temperatures is the increasing fraction of orthorhombic martensite. Additional transformation $\beta_1^{'}$ to $\gamma_1^{'}$ occurs during the ausforming at temperatures lower than $900^\circ C$

8. Ausformed samples after the same degree of deformation rolled at $1000^\circ C$ to $850^\circ C$ show sine curves and emphasize the processes of nucleation and growth.

9. The interval phase transformation temperature ranges between $67^\circ C$ to $170^\circ C$ for thermo-mechanically treated alloy that is an important point in choosing and designing sensor and actuators from this SMA_s family.

10. The sample deformed at $850^\circ C$ is a linear transformation which no longer meets Avrami type kinetics.

References

[1]. Otsuka K, Wayman CM, editors - *Shape memory materials,* Cambidge University Press, 1998

[2]. Miodrag Čolića, Rebeka Rudolfb, Dragoslav Stamenkovićc, Ivan Anželb, Dragana Vučevića, Monika Jenkod, Vojkan Lazićc and Gorazd Lojenb - *Relationship between microstructure, cytoplasticity and corrosion properties of a Cu-Al-Ni shape memory alloy,* Acta Biomateriallia, Volume 6, Issue 1, January 2010, Pages 308-317

[3]. Erhard Hornbogen - *A comparative study of ausforming of shape memory alloys with A2 and B2 structures,* Materials Science and Engineering A273–275 (1999) 630–633

[4]. M. Franz, E. Hornbogen - *Martensitic transformation of a CuZnAl-shape memory alloy strengthened by hot-rolling,* Materials Science and Engineering A252 (1998) 157–165

[5]. H.C. Kou, J.Wang, B. Tang, X.F. Gu, J.S.Li, L. Zhou - Effect of kinetic model on parameter distorsions in non- isothermal transformations, Journal of alloys and compounds, 479, (2009), p. 122-125

[6]. J. Rodriguez, I Ruiz Larrea, M.L. No, A. Lopez Echari, J. San Juan - Kinetic effects in the mixed β to β'₃, +γ'₃ martensitic transformation in a Cu-Al-Ni shape memory alloy, Acta materialia, 2009

[7]. J. Rodríguez-Aseguinolaza, I. Ruiz-Larrea, M.L. Nó, A. López-Echarri, J. San Juan - *Kinetic effects in the mixed β to martensitic transformation in a Cu–Al–Ni shape memory alloy,* Acta Materialia, Volume 58, Issue 2, January 2010, Pages 692-701

[8]. C.Picornell, *Two way shape memory effect in Cu-Al-Ni single crystal,* Materials Science and Engineering, Volume A273-275 (1999), 605-609

[9]. U. Sari, T.Kirindi - *Effectsof deformation on microstructure and mechanical properties of a Cu-Al-Ni shape memory,* Materials Characterisation, 59 (2008), 920-929

[10]. F.Liu, G.C. Yang, J.N. Liu - Comparison between an analytical model and JMA kinetics for isothermally and isochronically conducted transformations, Thermochimica acta 438 (2005) p. 83-89

[11]. Yan Zhi jie, Dang Shu-e, Wang Xiang-hui, Lian Pei-xia - Applicability of Johonson-Mehl-Avrami model crystallization kinetics of $Zr_{60}Al_{15}Ni_{25}$ bulk amorphous alloy, Trans.Nonf. Met. Soc. China, (2008), 138-144

SOME RESEARCHES ON THE CUTTING PROCESS USING A STAMPING DEVICE

Nicolae CANANAU, Ovidiu DIMA, Dinel TANASE
Dunărea de Jos University of Galati
email: ncananau@ugal.ro

ABSTRACT

The cutting process of the parts from the plates and strips consists in the action of two active elements of the stamping machine: device punch and active plate. The main actors on which the cutting process depends are the thickness and the mechanical characteristics of the material to be cut, the state of the edges of the active elements and the clearance between the active elements. This paper presents the results of the research on the variation of the stamping force depending on the thickness and the stamp clearance for the maximum cutting force.

KEYWORDS: cutting process, stamping force

1. Introduction

Stamp cutting stamping is a deformation process of the sheets and strips used to obtain various parts by a cutting operation: cutting out, perforation, cutting off, notching etc. (fig.1).
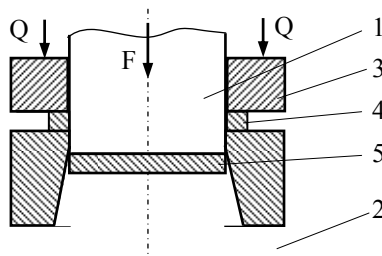

Fig. 1. *Scheme of the stamp cutting process:*
1-punch, 2-active plate, 3-restraint plate,
4-initial material (band), 5-cut out part

Under the action of the force F applied on the punch 1, between the edges of the punch and the active plate 2 a shearing stress and strain states are developed. As an effect, a cutting process is developed and the cut out part 5 is separated from the initial band 4.

In the case of the precise cutting out process, a restraint plate 3 may be used on which fastening force is applied. This way, the precision of the worked part is better.

The character of the stress state during the cutting process is described in Figure 2. The stages of the cutting are: the first stage is the elasto-plastic behavior of the material (Fig.2.a). The sharpened

edges are cutting effectively the material fibres. In this stage the force increases reaching a maximum value and then rapidly decreases to zero.

At the moment of maximum value of the force in the edge of the punch and of the active plate, the cracks are developed (fig.2b).

(a)   (b)
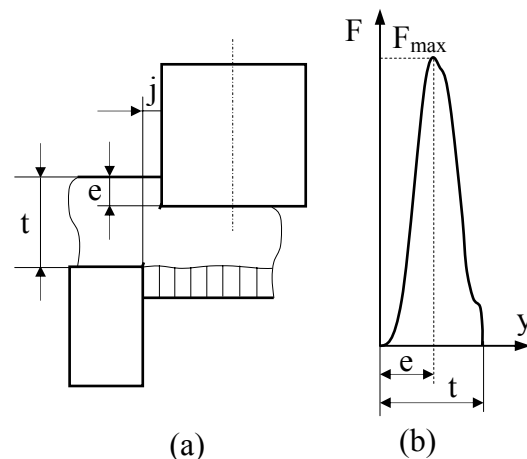
Fig. 2. *Cutting stage of the stamping process: (a) the scheme of the cracks appearance, (b) force variation at the cutting process*

Under optimum conditions, the directions of the cracks coincide. In this case the maximum force value will be minimum. This happens when the value of the stamp clearance is optimum.

Also, for optimum value of the clearance between the punch and the active plate, the precision of the dimension and quality of the cut border is better.

2. Experimental conditions

The experiments made with a stamping device are rendered in the Figure 3.
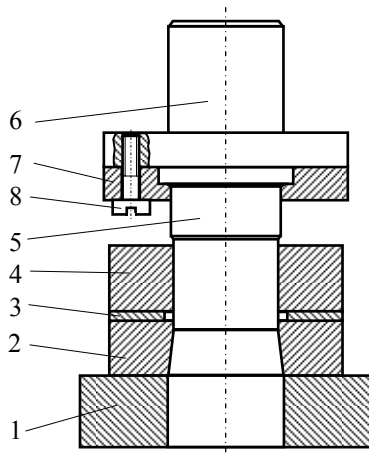
Fig. 3. *Stamping device:*
1-support plate, 2-active plate, 3- guiding rules,
4-guiding plate, 5-punch, 6-centering spigot
7-port-punch plate, 8-screw.

The dimensions of the active elements of the stamping device are rendered in Table 1.

Table 1. *Dimensions of the active elements*

Diameter of active plate hole, [mm]	25	25	25	25
Diameter of punchess, [mm]	24.95	24.8	24.6	24.4
Clearance, [mm]	0.05	0.2	0.4	0.6

The samples were prepared in low carbon steel strips (1.26x30x600 mm); the chemical composition of the steel is rendered in Table 2 and its mechanical characteristics in Table 3.

Table 2. *Chemical composition of the steel*

Chemical composition, %					
C	Mn	Si	P	S	Al
0.142	0.531	0.246	0.021	0.019	0.023

Table 3. *Mechanical characteristics of the steel*

| Rp0.2 [MPa]	Rm [MPa]	A_{10} [%]	Z [%]
224.7	354.5	32.4	53.7

The experimental stand was a hydraulic press of 300 kN maximum pressing force, equipped with a data acquisition system type Spider 8 usable in the dynamic pressing processes.

The experiments focused on the influence of the stamp clearance on the value of the force and on the precision and quality of the samples.

3. Results and analysis

The variation of the force during the cutting process is rendered in Table 4 and is represented in graphic form in Figure 4.

Table 4. *Experimental values of the cutting force*

| Clearance j, mm	Relative clearance j/t	Move-ment y, mm	Relative movement y/t	Force, F, $\times 10^3$,[N]
0.05	0,040	0.315	0.250	15.05
		0.472	0.375	20.01
		0.630	0.050	23.52
		1.165	0.625	27.15
		0.964	0.755	28.71
0.20	0.159	0.315	0.250	12.82
		0.472	0.375	18.05
		0.630	0.050	22.02
		1.165	0.625	25.44
		0.964	0.755	27.29
0.40	0.318	0.315	0.250	12.04
		0.472	0.375	16.83
		0.630	0.050	20.51
		1.165	0.625	23.31
		0.964	0.755	24.29
0.60	0.476	0.315	0.250	14.25
		0.472	0.375	18.24
		0.630	0.050	22.43
		1.165	0.625	25.05
		0.964	0.755	26.51
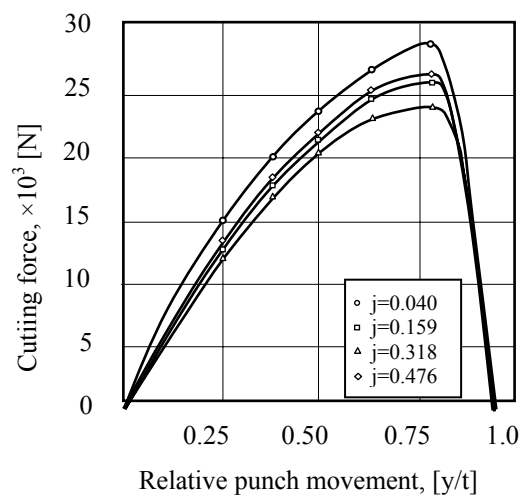
Fig. 4. *Force variation during the cutting process*

The maximum force is developed for a 0.755 relative value of the punch movement.

The dependence of the maximum force on function of the stamp clearance is represented in Figure 5.
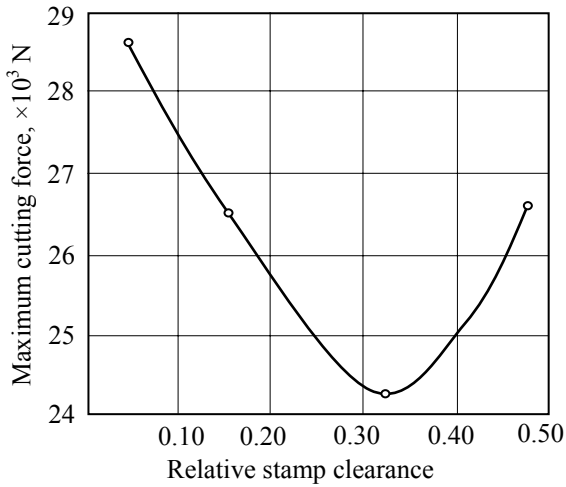

Fig. 5. *Variation of the maximum cutting force with therelative clearance*

For small values of the relative stamp clearance the cutting force has great values. When the relative stamp clearance is increased, the maximum value of the force decreases until the minimum value which corresponds to the 0.318 value of the relative stamp clearance. When the relative stamp clearance increases the value of the cutting force increases.

It is clear that the optimum value of the stamp clearance during the cutting process is 0.318.

The stamp clearance has influence on the precision of the cut part. The dimensions of the cut part were measured with a micrometer the precision of which is 0.001 mm.

The results are rendered in the table 5.

Table 5. *Effective deviation during the cutting process*

j	j/t	D_p	D_0	$\Delta=D_p-D_0$
0.05	0,040	25.014	25.0	+0.014
0.20	0.159	25.005	25.0	+0.008
0.40	0.318	24.993	25.0	-0.007
0.60	0.476	24.976	25.0	-0.024

The precision of the cut parts is showed in figure 6.

4. Microstructure in the cutting zone

Specific cut stress and strain states develop in the cutting zone causing the crystalline grains to be deformed by rotation, elongation and fragmentation.

At the beginning of the cutting process the grains are deformed in the proximity of the punch edge and the deformation is transmitted into the thickness of the part (Fig.7).

Fig. 6. *Precision of the cut part*
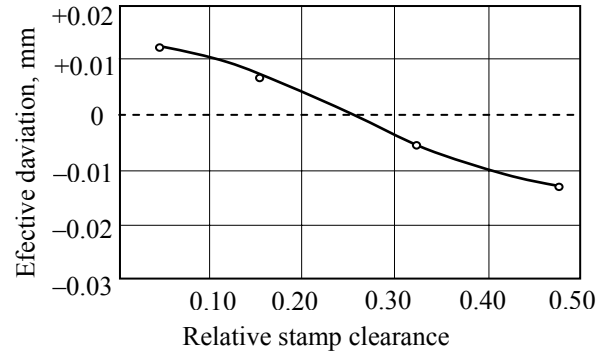

Fig. 7. *Microstructure in the cutting zone at the beginning of the cutting process (Nital 2%, ×200)*

At a later stage of the cutting process (Fig.8) the intensity of the grains deformation degree is very great, especially in the proximity of the punch edge.
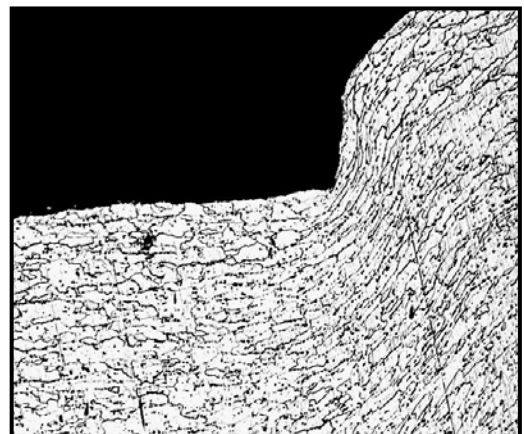

Fig. 8. *Microstructure in the cutting zone at an advanced stage of the cutting process (Nital 2%, ×200)*

For the final cutting process, in the proximity of the maximum level of the cutting force, the grains are very intensely deformed (Fig.9).

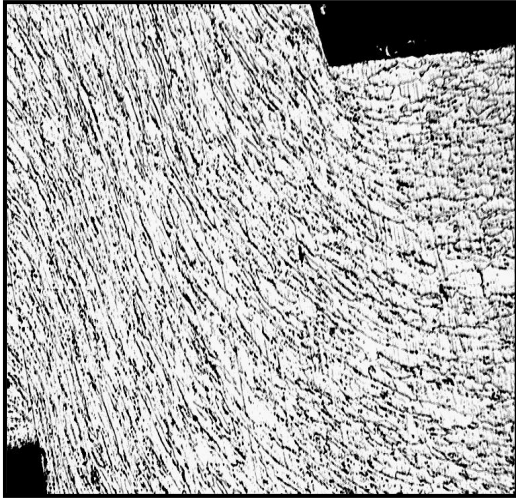The deformation hardness is very intense and conditions for crack appearance are created.

Fig. 9. Microstructure in the cutting zone at the final stage of the cutting process (Nital 2%, ×200)

Obviously, at the border of the cut part, the hardness, greater than the initial one, corresponds to the hardness of the material in the volume of the part, at a greater distance from the cut border.

This is the reason why we must be careful when the deforming process continues and the cut border of the part is intensely deformed during the following deforming operations.

4. Conclusions

The cutting process is characterized by complex and intense stress and strain states.

The force increases during the cutting process, reaches a maximum value and then decreases rapidly to zero. At the moment of the maximum value of the cutting force, in the proximity of the punch and of the plate edge, cracks are generated. Afterwards, the cutting process is developed by propagation of the cracks. The relative movement of the punch at the maximum value of the cutting force was 0.76, which corresponds to the great plasticity of the part material.

The minimum value of the maximum force corresponds to the 0.318 value of the stamp clearance.

The maximum precision of the part correspond at the 0.27 value of the relative stamp clearance.

The microstructure in the cutting zone is very strongly deformed and consequently the deformation hardening of the deformed material increases. As a result, the deformation behavior of the border of the cut part is reduced and the following deformation operation becomes more difficult.

References

[1]. **Teodorescu, M.** – *Elemente de proiectare a stantelor si matritelor*, EDP, Bucuresti, 1977.
[2]. **Roamnovski, V.P.** – *Stantarea si matritarea la rece*, Ed. Tehnica, bucuresti, 1970.
[3]. **Lazarescu, I., Stetiu G.** – *Proiectarea stantelor si matritelor*, EDP, Bucuresti, 1973.
[4]. **Merchant, E.M.** – *Mechanics of the metal cutting proces*, Journal of applied physics, M.C. Shaw, 2004
[5]. **Jaspers, S.** – *Material behaviour in conditions similar to metal cutting flow stress in the primary zone*, Journal of Material Processing Technology, vol. 122, issues 2-3, march 2002, pp.322-330
[6]. **Nagît, Gh., Braha, V.** – *Bazele prelucrarii prin deformare plastica*, Ed. Tehnica, Chisinau, 2002.
[7].*** ASM, Metal Handbook, vol. 4, Ohio, 1969.

THE EXPERIMENTAL ANALYSIS REGARDING THE EVOLUTION OF SOME MECHANICAL CHARACTERISTICS FOR A STEEL USED IN CONSTRUCTIONS OF CONDUITS FOR STEAM TRANSFER

[1]**Dumitru MIHAI,** [2]**Silviu MACUTA**

[1]"Gh. Asachi" Technical University of Iasi, Faculty of Mechanical Engineering,
Strength of Materials Department
[2]"Dunarea de Jos" University of Galati, Faculty of Mechanical Engineering,
email: silviu.macuta@ugal.ro

ABSTRACT

The metallographic analysis [4], revealed that the initial ferrite-pearlite structure of the steel under study shows slight tendencies for coalescence, decarburation and carbide precipitation. The precipitating carbides maintained their globular shape being located on the grain boundaries. Due to the metallurgical degradation, the mechanical degradation occurs as a consequence of both cavities and microcracks formation processes. Based on the values determined for the mechanical characteristics of the pipe under study it has been concluded that the material is suitable for continuing the service and has marked resistance reserves. These reserves have been explained by the absence of the marked processes of grain boundary decarburation and the carbide network formation.

KEYWORDS: low alloy steel, metallurgical degradation, irreversible structural phenomena

1. Introduction

The present paper aims to derive the influence of both the functioning time and the service temperature on the mechanic and elastic characteristics of 15123-CSN steel. Likewise, the structural changes are analyzed in the above steel when used in the steam pipes of the kettles from thermal power stations.

Based on the test results, it will be found out if whether the structural changes as well as those produced in the mechanic and elastic characteristics still allow or not for the piping to be kept in service.

2. Experimental part

The specimens were taken from longitudinal and transversal sections of 15123-CSN steel pipes that initially had the same dimensions and served under the same service temperatures and pressures as already reported [1].

The specimens have been analysed in initial state and after two different functioning periods namely 35789 and 58371 functioning hours, respectively. The experiments consisted in mechanical tests and metallographic analyses.

The mechanical tests comprised tensile, toughness and hardness tests and were performed in accordance with the Romanian norms for special equipment ISCIR C29-67. Both the entire procedure and the test temperature have been mentioned in the previous study [1].

The metallographic analysis has been performed by means of an optical microscope at magnifications ranging from 100:1 to 1000:1. The specimens have been carefully prepared, without damaging the inner and outer edges of the wall thickness and etched with a solution of 2 % HNO_3 in alcohol.

3. Results and discussion

The standard and the experimental values of the ultimate stress are listed in Table 1.

Table 1. *The standard and experimental values of the ultimate stress, Rm, [MPa]*

Functioning hours	Source of data	Posi-tion	Test temperature, (°C)						
			20	510	540	560	565	570	
	S	T	450-460	180 at 500°C		150 at 550°C		82 at 575°C	580
		L	450-460						
0	E	T	671.9	485	438.8	425.6	418.2	411.2	410.3
		L	704	533.9	496.7	481.2	469.2	460.1	459.5
35789	E	T	451.8	221.2	195.6	190.8	175.3	174.4	155.4
		L	461.3	235.8	201.5	195.6	183.2	178.2	168.7
58371	E	T	541.2	325.8	219.3	201.6	199.3	190.5	155.6
		L	560.8	356.4	301.7	241.2	236.2	201.6	196.8

The standard and the experimental values of the yield stress, under the same conditions regarding the functioning periods and the test temperatures are listed in Table 2. Finally the standard and experimental values of Brinell hardness are shown in Table 3.

Table 2. *The standard and experimental values of the yield stress Rp0.2, [MPa]*

Functioning hours	Source of data	Posi-tion	Test temperature, (°C)						
			20	510	540	560	565	570	580
	S	T	min 300	95 la 500°C		80 la 550°C			75
		L	min 300						
0	E	T	526.2	392.1	362.5	335.6	320.7	318.3	315.8
		L	575.3	419.9	392.5	390.2	391.9	385.3	369.2
35789	E	T	311.3	210.6	209.8	183.2	180.6	179.2	169.5
		L	315.7	217.8	218.9	191.5	190.5	181.4	175.3
58371	E	T	361.3	268.9	231.2	214.5	211.3	209.5	201.4
		L	381.4	305.6	248.3	235.9	226.4	218.3	215.6

Table 3. *The experimental values of the Brinell hardness, HB*

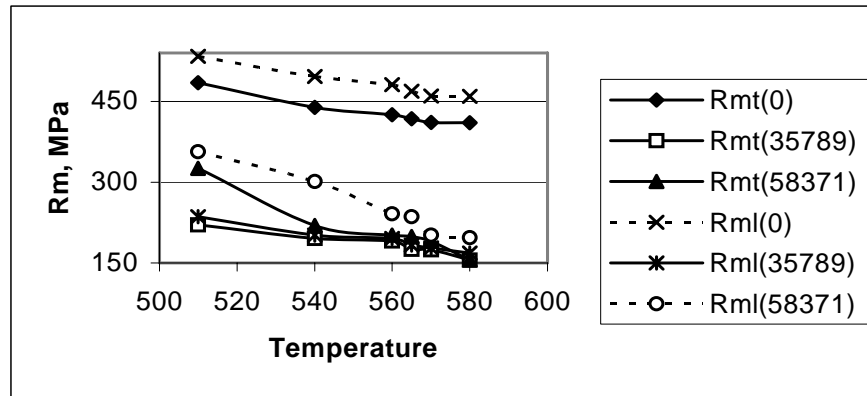| Functioning hours	Source of data	Posi-tion	Test temperature, (°C)						
			20	510	540	560	565	570	580
	S	T	1350-1830						
		L	1350-1830						
0	E	T	2107	1997	1901	1895	1826	1799	1631
		L	2127	1997	1905	1898	1826	1805	1683
35789	E	T	1385	1187	1113	1106	997	905	889
		L	1397	1200	1117	1115	1095	985	908.7
58371	E	T	1365	1201	1195	996.8	991.5	875.4	796.2
		L	1385	1209	1201	1110	999.8	998.5	865.9

Fig.1. Evolution tendency of the ultimate stress with test temperature and functioning period

As noticeable, no standard hardness values have been found for elevated temperatures [2]. In the tables the symbols specify if the values are taken from standards (S) or are experimentally determined (E) and if the specimens were taken from longitudinal (L) or transversal (T) sections.
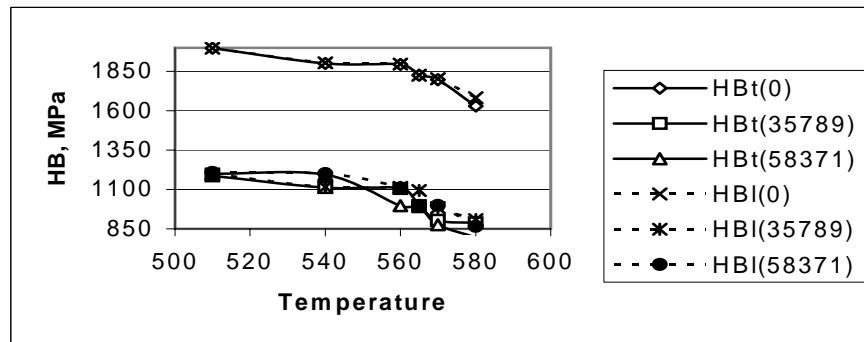

Fig.2. Evolution tendency of the yield stress with test temperature and functioning period

The metallographic analysis revealed that 15123-CSN steel had a prevalent ferrite structure that includes up to 10 % pearlite [3]. The ferrite grains have rather uniform shapes and sizes along the wall thickness section. The grain sizes have been determined as 6-7, 7-8 and 8-9 according to the Romanian standard STAS 5490-80. In the area located at the interior of the wall thickness a coalescence process is noticed at the ferrite grains that reach a grain size of 5. At the magnification of 100:1 no carbide precipitation has been noticed.

The decarburation process is metallographically noticeable on both sides of the wall thickness reaching a 0.3-mm depth in certain areas. No corrosion has been observed since the pipe shows an inner oxide layer with variable thickness that obviously differentiates from the rest of the structure. On the micrographs recorded at the magnifications 500:1 the same uniform structure has been observed that shows however some coalescence areas.

The carbides have mostly globular shape and are located on the grain boundaries. Yet in some areas the tendency to form a carbide pellicle has been observed. In the coalescence zones the carbide formation process is intensified but the carbides maintain their globular form and their intergranular preferred distribution. The same aspects have been observed at the magnification of 1000:1 regarding both the globular carbide distribution along the ferrite grain boundaries and the intensification of the carbide formation process in the coalescence zones.

The results of the mechanical tests are summarized in Figures 1, 2 and 3 that show the evolution of ultimate stress (R_m), yield stress ($R_{p0.2}$) and Brinell hardness (HB), respectively with the test temperature and the functioning period. The curves have been plotted by the interpolation of the data found in the above three tables [4]. Here again the symbols t and l designate transversal and longitudinal sections, respectively.

The study of the variations of the mechanical properties with temperature emphasizes that, as compared to the data found in standards, the material has a large reserve regarding the ultimate stress R_m.

4. Conclusions

1. In the case of the pipe under study it has been concluded that the material is suitable for continuing the service and has marked resistance reserves. These reserves are explained by the absence of both the grain boundary decarburation process and the carbide network.

2. The interpolated variation tendencies of the mechanical characteristics R_m, $R_{p0,2}$ and HB as a function of temperature, allowed to predict the functioning time under safe service conditions, of the pipe under study. A fair precision level has been attained for the functioning time prediction, due to the low values of maximum deviation of the interpolated curves as compared to the experimental ones.

3. The metallurgical degradation has been caused generally by the structural degradation and particularly by the fluctuations of the precipitates and the alloying elements within the metal matrix. These degradation processes lead to intergranular erosion by cavitation that causes the fragile failure of the steels at elevated temperatures. The mechanical degradation occurs as a consequence of both cavities and microcracks formation processes.

References

[1]. Mihai, D. - *The metallurgical degradation of the 12H1MF steel*, to be pulished in Bul.Inst.Polit. Iasi, t. XLVI (L), 2000
[2]. Chesa, I., Lascu, N. et al. – *Steel grades and products* (in Romanian), Editura Tehnica, Bucuresti, 1989;
[3]. Ailincai, G. et al. – *Studies on the structural transformation stage of the steam piping materials of the kettles from thermal power stations* (in Romanian), Research contract no. 21316-74. Beneficiary: CIPEET Bucuresti;
[4]. Ailincai, G. and Mihai, D. – *Studies on the structural transformation stage of the steam piping materials of the kettles from thermal power stations* (in Romanian), Research contract no. 264-85. Beneficiary: ICEMENERG Bucuresti.

SULPHATE REDUCING BACTERIA IN BIOFILMS ON THERMOSETTING POLYMERS/Zn COMPOSITE LAYERS

[1]Alina CIUBOTARIU, [1]Lidia BENEA, [2]Wolfgang SAND

[1]Dunarea de Jos University of Galati, Competences Center Interfaces –
Tribocorrosion and Electrochemical Systems (CC-ITES),
[2]University of Duisburg Essen, Biofilm Centre, Aquatic Biotechnology, Germany
email: Alina.Ciubotariu@ugal.ro

ABSTRACT

Bacterial adhesion to surfaces is the first step in the formation of a biofilm and has been studied extensively over the past decades in many diverse applications. Sulphate Reducing Bacteria (SRB) is a group of phylogenetically diverse anaerobic microorganisms that were first discovered by Beijerinck in 1895. This work investigates the attachment of Sulphate Reducing Bacteria and the modification of roughness before and after the attachments on the surfaces of zinc and thermosetting polymers/zinc composite layers obtained by electro co-deposition. There were used two types of thermosetting polymers: phenol – formaldehyde resin (type NOVOLAC) and epoxi resin. For investigations of the surfaces were used atomic force and epifluorescence microscopy methods (AFM and EFM, respectively). Sessile bacteria on coupons were stained with 4', 6-diamidino-2-phenylindol (DAPI) and visualized by EFM as well as AFM. The best imaging conditions for AFM were assessed.

KEYWORDS: biofilm, composite layers, Sulphate Reducing Bacteria, Atomic Force Microscopy, Epifluorescence Microscopy, roughness

1. Introduction

Bacterial adhesion mechanism is complex and many factors affect cell adhesion [1]. Some bacteria have been reported to accelerate the corrosion of metals, while others influence the corrosion behavior in a beneficial way. Desulfovibrio desulfuricans, Pseudomonas sp. and Bacillus sp. can accelerate corrosion. On the other hand, Bacillus subtilis has been shown to inhibit the corrosion of aluminum 2024 by secreting polyglutamate and polyaspartate [2, 3], while Pseudomonas flava inhibits corrosion by forming a phosphate film [4].

Central to the phenomenon of microbially induced corrosion is the formation of biofilm on the metal surface. The biofims are formed by microbial aggregates and extracellular polymeric substances (EPS). The EPS creates a microenvironment for sessile bacteria and allow for the development of synergistic relationship. Their main components are not only polysaccharides, but also proteins, lipids and nucleic acids in minor proportion [5].

Sulphate Reducing Bacteria (SRB) is a group of phylogenetically diverse anaerobic microorganisms that were first discovered by Beijerinck, in 1895. At

present, 14 genera have been identified, the two most established genera of SRB being Desulfovibrio and Desulfotomaculum [6, 7]. The biofilms are involved in both beneficial and detrimental effects: one beneficial aspect is their potential use as biosurfactancts in tertiary oil production and their capacity to trap heavy metals; as detrimental effect, biofouling increases friction resistance and produces changes in metallic surface properties (hydrophobicity, roughness, color, etc.); finally, biofilms participate in biocorrosion by bind with metal ions [8].

The atomic force microscope is a mechanical imaging device that requires minimal sample preparation and creates three-dimensional images with high spatial resolution. By combining AFM and EFM, two techniques with complementary strengths and weaknesses are joined to yield a powerful tool for the investigation of biological samples [9 - 12]. Using this methods, it was reported the attachment of SRB on different type of materials: 316 stainless steel [13 - 14], D36 carbon steel [15], C1018 carbon steel [16], alloy 625 and austenitic stainless steel [17], Q235 steel [18], heat resistant steel 1Cr18Ni9Ti [19], ASTM grade 2 titanium [20], cerium-doped TiO$_2$ film

on 304 stainless steel [21], polyurethane foam Ringlace® and lava rock [22], polyurethane foam (PU), vegetal carbon (VC), low-density polyethylene (PE) and alumina-based ceramics (CE) [23].

The literature is penurious referring to attachment of SRB on metal and especially on composite layers. For this reason, in the present study the work was focus on performing AFM coupled with EFM studies in order to observe the influence of materials structure (pure zinc, PF resin/Zn composite layers and epoxi resin/Zn composite layers prepared by electro co-deposition) on SRB attachment.

2. Materials and methods

2.1 Substratum and biofilm formation

Three types of surfaces were prepared by electro co - deposition: pure zinc, PF resin/Zn composite layers and epoxi resin/Zn composite layers. They were electrochemically deposited from a bath with the following composition: 310g/L $ZnSO_4$ · $7H_2O$; 75g/L Na_2SO_4 · $10H_2O$; 30g/L $Al_2(SO_4)_3$ · $18H_2O$. The pH of the solution was 3.8.

These layers were electrodeposited on DC04 steel as substrate. Suspension for electro co - deposition of composite layers was prepared by adding phenol formaldehyde resin particles, respectively epoxi resin particles (mean diameter 6 – 10μm) to the solution to give a concentration of 10g/L in the zinc electrolyte plating bath. Electro co - deposition took place in the bath at a temperature of 25^0C, current density of $4A/dm^2$, time for electrodeposition 30min. The suspension bath was stirred by a mechanical stirrer at a constant rotational speed of 800rpm.

In this investigation, SRB from the University of Duisburg Essen Biofilm Centre, Aquatic Biotechnology were used for bacterial adhesion tests. The pH of solution with cells suspension was 6.2. The attachment of cells was made in the following steps: putting a drop from the prepared solution cells on the tested surfaces; waiting to dry (15-20min); next, coupons were incubated in bacterial suspension of SRB (1 ppb organic matter 10^9cells/mL) for 24h to allow for the attachment and biofilm formation with 2, 5% glutaraldehyde.

2.2. Instrumentation

Biofilm and attached cells on pure zinc, PF resin/Zn composite layers and epoxi resin/Zn composite layers were investigated with combined AFM and EFM methods. Subsequently, they were stained with 0.01% (wt/vol) DAPI for 10min and visualized at the epifluorescence microscope.

A NanoWizardII atomic force microscope (JPK Instruments, Germany) and an upright epifluorescence microscope (AxioImager A1m; Zeiss, Germany) were combined using the BioMaterialWorkstation (JPK Instruments). Throughout the present study the prototype of this new system was used. The key feature of the BioMaterialWorkstation was a shuttle stage that carried the actual sample precisely fixed on a glass slide. This shuttle stage could be transferred between the atomic force microscope and the epifluorescence microscope, giving a precise positioning of the stage on both microscopes.

For AFM images, silicon cantilever CSC37 A (Mikromasch, Estonia) with the following features was used: typical length, 250 μm; width, 35 μm; thickness, 2 μm; resonance frequency, 41 kHz; and nominal force/spring constant, 0.65 N/m. Each AFM image consists of 512 by 512 pixels. AFM images were performed by contact mode in air.

3. Results and discussion

The surface structure of pure zinc layer and thermosetting polymers/Zn composite layers under atomic force microscope are presented in Figs. 1 – 3. It can be observed that the surface of zinc is made up of regular crystals.
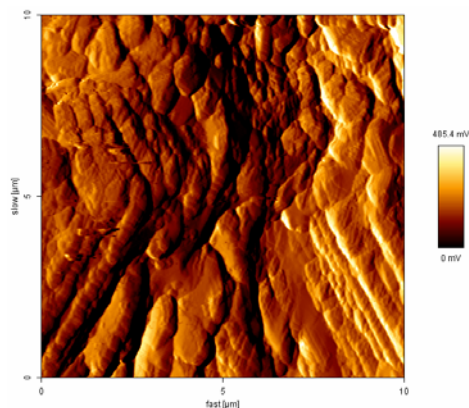

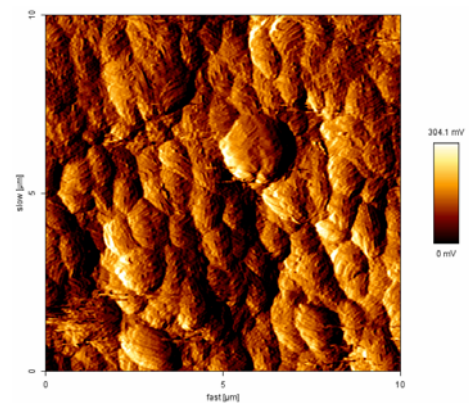**Fig. 1**. *2D - AFM image of untreated pure zinc surface*

Fig. 2. *2D - AFM image of untreated surface PF resin/Zn composite layer*

The thermosetting polymers particles co - deposited with zinc disorder the regular crystal structure and the structure of the zinc matrix becomes finely crystalline.

The pure zinc layers have a rather regular surface, whereas the composite layer surfaces have finer grains structure with particles of resin uniform by distributed on the surfaces. The thermosetting polymer could have an inhibition effect of zinc crystals growth and a catalytic effect in increasing nucleation sites.
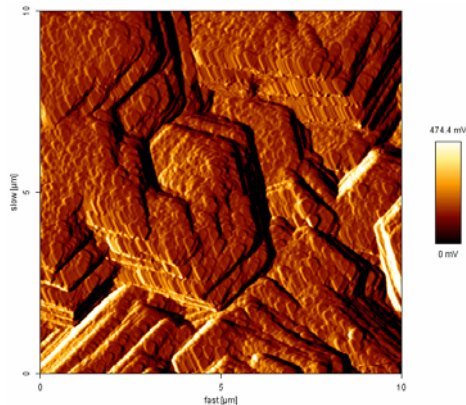

Fig. 3. 2D - AFM image of untreated surface epoxi resin/Zn composite layer

Epifluorescence microscopy (EFM) images of a DAPI – stained biofilm sample of SRB on the surface of zinc and thermosetting polymers/Zn composite layers are presented in Figs. 4 – 6.
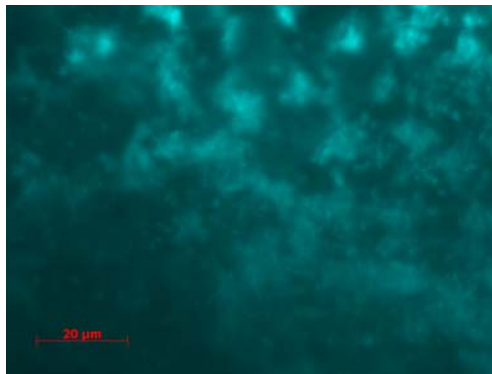

Fig. 4. EFM image of the SRB attachment and EPS formed on pure zinc surface
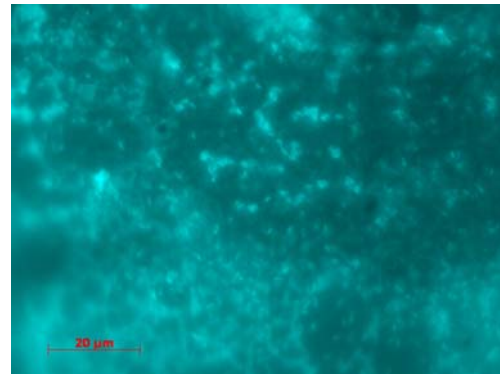
Fig.5. EFM image of the SRB attachment and EPS formed on PF resin/Zn composite layers surface
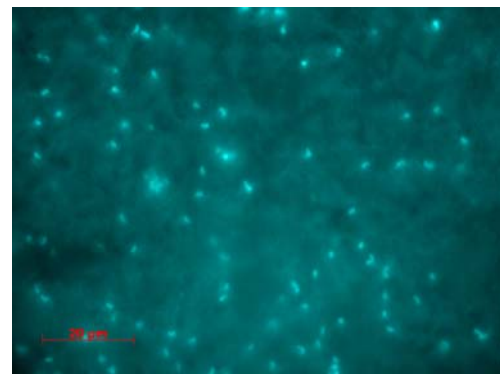
Fig.6. EFM image of the SRB attachment and EPS formed on epoxi resin/Zn composite layers surface

From the EFM images, it was observed that the attachment of SRB on thermosetting polymers/Zn composite layers surface is lesser than on pure zinc surface. Those facts indicated that the thermosetting polymers/Zn composite layers are more resistant to the attack of microorganisms like SRB.

Figs. 7 – 9 show the 3D images of the AFM scan acquired by contact mode in air on pure zinc layers and thermosetting polymers/Zn composite surfaces untreated and after SRB attachment with biofilm and EPS formation.
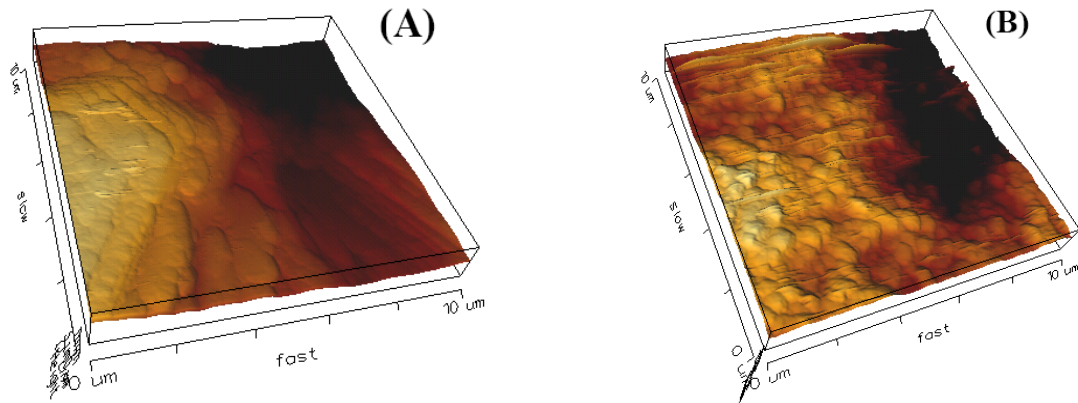
Fig. 7. 3D **-** *AFM images of pure zinc surface: (A) - untreated; (B) - with SRB bacteria*
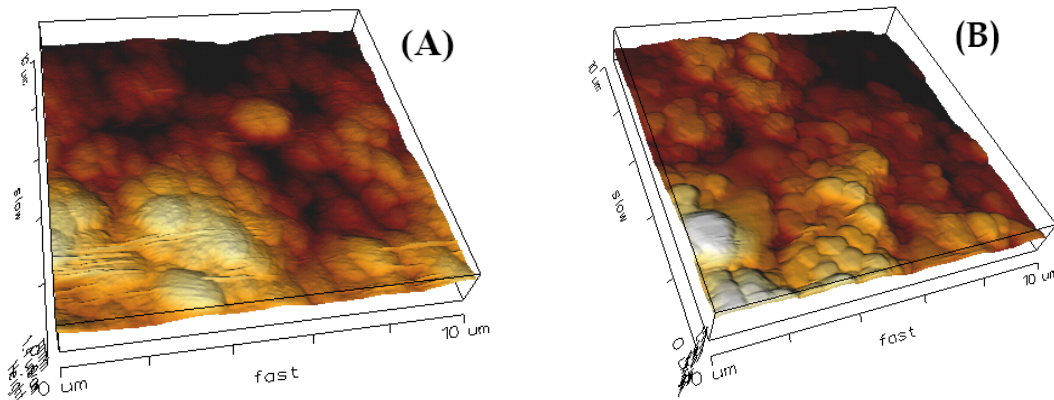
Fig. 8. 3D **-** *AFM images of PF resin/Zn composite layer surface*
(A) - untreated; (B) - with SRB bacteria
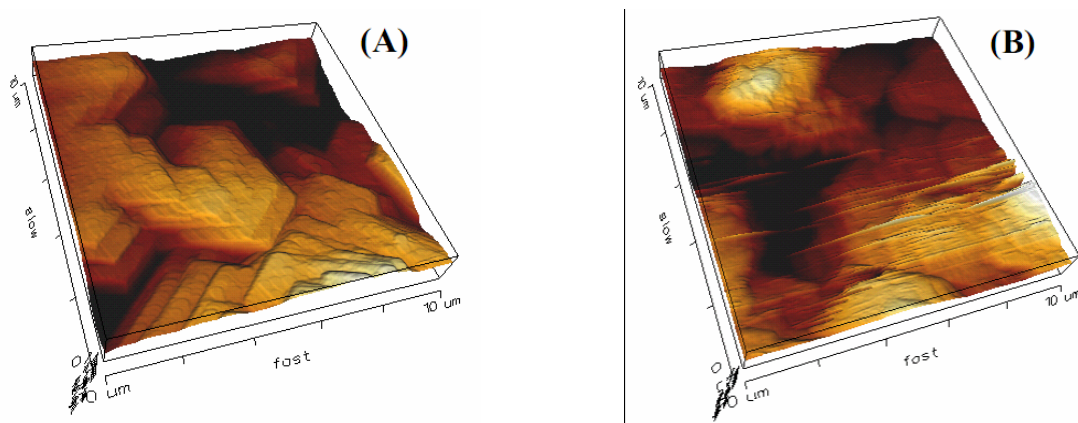
Fig. 9. 3D **-** *AFM images of epoxi resin/Zn composite layer surface*
(A) - untreated; (B) - with SRB bacteria

The differences between untreated surfaces and treated with SRB are visible, representing the attached cells of Sulfate Reducing Bacteria on the surfaces, biofilm and EPS formation. EFM – AFM images indicate an adherence process of the microorganisms on the tested surfaces. The use of microscopy to count adhered cells on surfaces is a viable technique, since, on a microscopic scale, surfaces can be found to have cracks and crevices, quite unlike the macroscopic appearance. These surface imperfections protect the microorganisms against removal by swab or rinse. The histograms of the scanned surfaces before and after the attachment of SRB are presented in Fig.10 - 12.
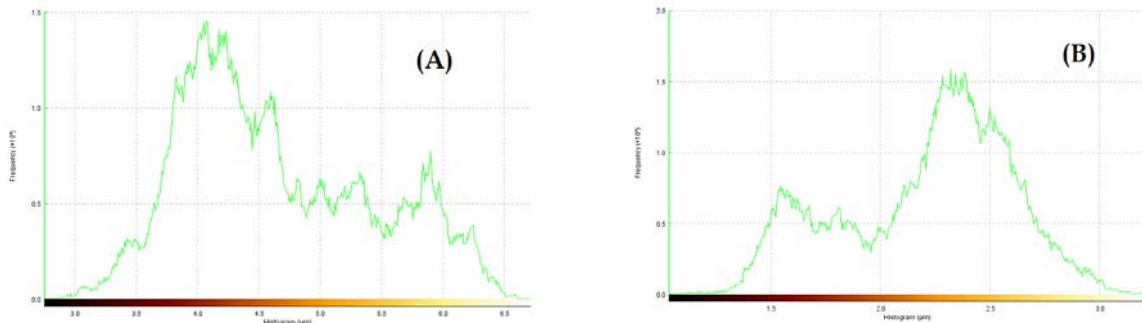
Fig. 10. Histograms of the scanned surfaces for pure zinc before (A) and after the SRB attachment (B)
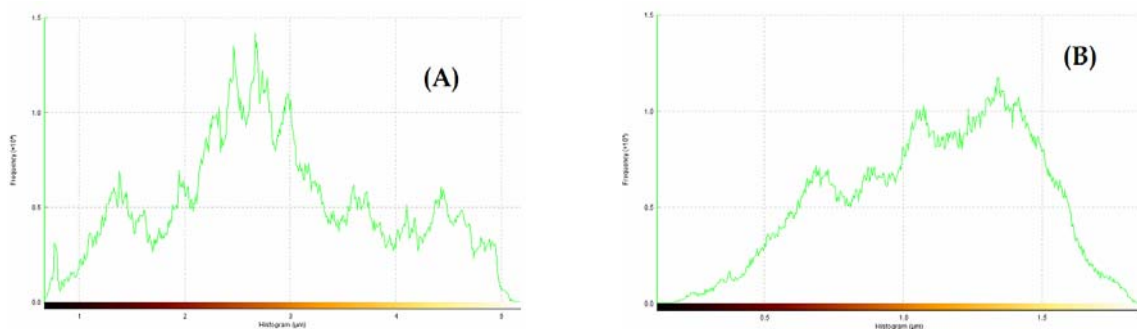
Fig. 11. Histograms of the scanned surfaces for PF resin/Zn composite layers before (A) and after the SRB attachment (B)
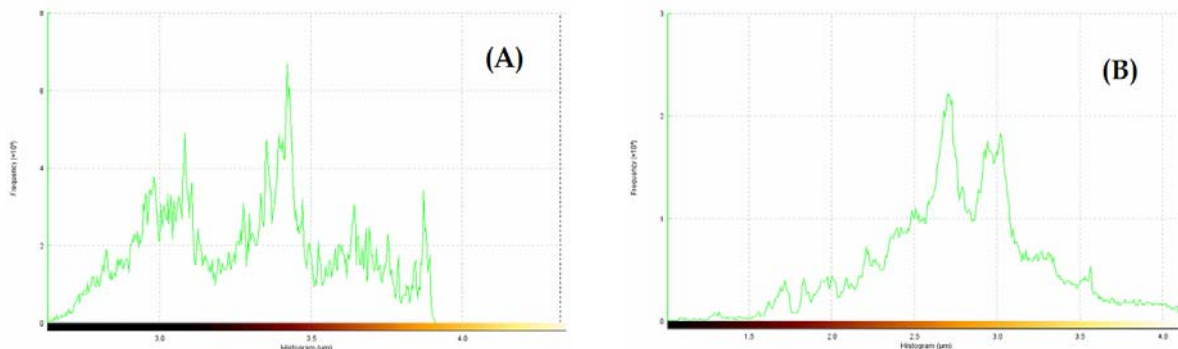
Fig. 12. Histograms of the scanned surfaces for epoxi resin/Zn composite layers before (A) and after the SRB attachment (B)

These histograms were used to calculate the roughness of the tested surfaces before and after the attachment of SRB, biofilm and EPS formation.

Roughness is a measure of the texture of a surface and plays an important role in determing how a real system will interact with the environment.

It is quantified by the vertical deviations of a real surface from its ideal form. If these deviations are large, the surface is rough; if they are small the surface is smooth.

The variation of the surfaces roughness for pure zinc and thermosetting polymers/Zn composite layers before and after attachment of SRB is shown in Fig. 13.

Fig.13. Variation of roughness surfaces of pure zinc and thermosetting polymers/Zn composite layers before (a) and after the attachment of SRB (b)

It could be observed that the values of roughness for composite layers without bacteria are smaller than the roughness of pure zinc.

The thermosetting polymer type PF resin and epoxy resin act as reducing the crystals size of electrodeposited zinc during co-deposition. For all systems tested the surfaces roughness decreases after the attachments of bacteria. That could indicate an increase of the uniformity for all tested surfaces after the attachments of SRB, biofilm and EPS formation.

From the EFM images and the values of the roughness it was observed that the attachment of SRB on thermosetting polymers/Zn composite layers is more reduced than on pure zinc surface. For pure zinc surfaces, the difference between the value of roughness for untreated and surface with SRB is bigger than other tested surfaces. That indicates a lot of bacteria attached on this surface, creating biofilm, EPS and corrosion product conducting to a smooth surface. Those f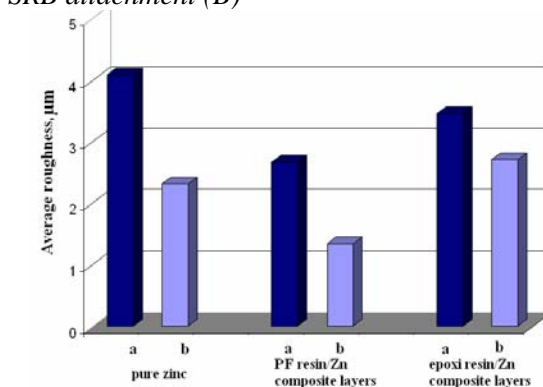acts indicated that the thermosetting polymers/Zn composite layers are more resistant to the attack of microorganisms like SRB.

4. Conclusions

The Sulfate Reducing Bacteria were attached on the pure zinc and thermosetting polymers/Zn composite layers.

Bacterial attachment on the surfaces is a complicated process that is affected by material surface (pure metal or composite layers).

From the epifluorescence microscopy and atomic force microscopy images it could be observed that the thermosetting polymers/Zn composite layers are more resistant to the attack of the Sulphate Reducing Bacteria than pure zinc layers.

The surface roughness decreases after the attachments of bacteria, biofilm and EPS formation.

The new system for combining imaging of AFM and EFM on pure zinc and thermosetting polymers/Zn composite layers is feasible for the application to study the biofilm formation by Sulfate Reducing Bacteria on these surfaces.

References

[1]. Q. Zhao, C. Wang, Y. Liu, S. Wang, *Bacterial Adhesion on the Metal- Polymer Composite Coatings*, International Journal of Adhesion and Adhesives, vol. 27, issue 2, p.85- 91, 2007

[2]. D. Ornek, T.K. Wood, C.H. Hsu, Z. Sun, F. Mansfeld, *Pitting Corrosion Control of Aluminum 2024 Using Protective Biofilms That Secrete Corrosion Inhibitors*, Corrosion, vol. 58, issue 9, p. 761 – 768, 2002

[3]. F. Mansfeld, H. Hsu, D. Ornek, T.K. Wood, B.C. Syrett, *Corrosion Control Using Regenerative Biofilms on Aluminum 2024 and Brass in Different Media*, Journal of the Electrochemical Society, vol. 149, issue 4, p. B130 –B138, 2002

[4]. G. Gunasekaran, S. Chongdar, S.N. Gaonkar, P. Kumar, *Influence of bacteria on film formation inhibiting corrosion*, Corrosion Science, vol. 46, issue 8, p. 1953-1967, 2004

[5]. I. B. Beech, J. A. Sunner, K. Hiraoka, *Microbe-surface interactions in biofouling and biocorrosion processes,* International Microbiology, vol. 8, issue 3, p. 157 - 168, 2005

[6]. L. L. Barton, *Sulphate-reducing bacteria*, Plenum Press, New York, 1995

[7]. R. Javaherdashti, *A review of some characteristics of MIC caused by sulfate-reducing bacteria: past, present and future,* Anti – Corrosion Method and Materials, vol. 46, issue 3, p. 173 – 180, 1999

[8]. H. C. Flemming and J. Wingender, *Relevance of microbial extracellular polymeric substances (EPSs) - Part II: Technical aspects,* Water Science Technology, vol. 43, issue 6, p. 9 – 16, 2001

[9]. W. Zhang, A. G. Stack, Y. Chen, *Interaction force measurement between E. coli cells and nanoparticles immobilized surfaces by using AFM*, Colloids and Surfaces B: Biointerfaces, vol. 82, issue 2, p.316-324, 2011

[10]. L. Kailas, E.C. Ratcliffe, E.J. Hayhurst, M.G. Walker, S.J. Foster, J.K. Hobbs, *Immobilizing live bacteria for AFM imaging of cellular processes*, Ultramicroscopy, vol. 109, issue 7, p. 775-780, 2009

[11]. J. Li, J. Li, W. Yuan, Y. Du, *Biocorrosion characteristics of the copper alloys BFe30-1-1 and HSn70-1AB by SRB using Atomic Force Microscopy and Scanning Electron Microscopy*, International Biodeterioration & Biodegradation, vol. 64, issue 5, p. 363-370, 2010

[12]. X. Sheng, Y. P. Ting, S. O. Pehkonen, *The influence of sulphate-reducing bacteria biofilm on the corrosion of stainless steel AISI 316*, Corrosion Science, vol. 49, issue 5, p. 2159-2176, 2007

[13]. C. Xua, Y. Zhanga, G. Chenga, W. Zhu, *Pitting corrosion behavior of 316L stainless steel in the media of sulphate-reducing and iron-oxidizing bacteria*, Materials Characterization, vol. 59, issue 3, p. 245 – 255, 2008

[14]. F. Kuang, J. Wang, L. Yana, D. Zhang, *Effects of sulfate-reducing bacteria on the corrosion behavior of carbon steel,* Electrochimica Acta, vol. 52, issue 10, p. 6084 – 6088, 2007

[15]. Jie Wen, Kaili Zhao, Tingyue Gu, Issam I. Raad, *A green biocide enhancer for the treatment of sulfate-reducing bacteria (SRB) biofilms on carbon steel surfaces using glutaraldehyde*, International Biodeterioration & Biodegradation, vol. 63, issue 8, p. 1102 – 1106, 2009

[16]. D. G. Enos and S. R. Taylor, *Influence of Sulfate-Reducing Bacteria on Alloy 625 and Austenitic Stainless Steel Weldments*, Corrosion, vol.52, issue 11, p. 831 – 843, 1996

[17]. Y. Wan, D. Zhang, H. Liu, Y. Li and B. Hou, *Influence of sulphate-reducing bacteria on environmental parameters and marine corrosion behavior of Q235 steel in aerobic conditions*, Electrochimica Acta, vol. 55, issue 5, p. 1528 – 1534, 2010

[18]. J. Liu, X. Liang and S. Li, *Effect of sulphate-reducing bacteria on the electrochemical impedance spectroscopy characteristics of 1Cr18Ni9Ti*, Journal of University of Science and Technology Beijing, vol. 14, issue 5, p. 425 – 430, 2007

[19]. T.S. Rao, Aruna Jyothi Kora, B. Anupkumar, S.V. Narasimhan, R. Feser, *Pitting corrosion of titanium by a freshwater strain of sulphate reducing bacteria (Desulfovibrio vulgaris)*, Corrosion Science, vol. 47, issue 5, p.1071–1084, 2005

[20]. H. Wanga, Z. Wang, H. Honga, Y. Yina, *Preparation of cerium-doped TiO₂ film on 304 stainless steel and its bactericidal effect in the presence of sulfate-reducing bacteria (SRB)*, Materials Chemistry and Physics, vol. 124, issue 1, p. 791–794, 2010

[21]. O. Basu; S. A. Baldwin, *Attachment and Growth of Sulphate-Reducing Bacteria on Different Support Materials,* Environmental Technology, vol. 21, issue 11, p. 1293 – 1300, 2000

[22]. A.J. Silva, J.S. Hirasawa, M.B. Varesche, E. Foresti, M. Zaiat, *Evaluation of support materials for the immobilization of sulfate-reducing bacteria and methanogenic archaea*, Anaerobe, vol. 12, issue 2, p. 93–98, 2006

RESEARCH REGARDING THE OBTAINING OF SOME COMPOSITE MATERIALS WITH METALLIC MATRIX FROM ALUMINIUM AND FeTi (32% Ti) REFRACTORY PARTICLES

Vasile BASLIU, Potecasu FLORENTINA
"Dunarea de Jos" University of Galati
email: vbasliu@ugal.ro

ABSTRACT

The aim of the paper is to create a composite material by a mechanical mixing method to be used in the field of steels elaboration in the deoxidizing and alloying stage.

KEYWORDS: composite material, Vortex method, ferroalloy

1. Introduction

The research objective was to find a method for the valorization of granular ferroalloy (FeTi32). Current ISO 5445/1995 standards require a grain with the lower limit of 3.5 mm for use in the development stage of deoxidation and alloying of steel.

The reintroduction in the steel making process of ferroalloy particle FeTi32 granular and powdery steelmakers reduces losses by the use of the particles.

Newly created composite materials have the intermediary densities the two initial density = 2.7 [g/cm^3][1] and FeTi32 bulk = 6.2 [g/cm^3][2]. This specific density is favorable for deoxidation process because the new material does not float in the slag area in the upper part ($\rho \sim 3$ g/cm^3) but descends in the metal bath of steel ($\rho \sim 6.9$ g/cm^3).

The combined deoxidation of steels has the advantages of placing in the same time a number of chemical elements in the metallic bath of steel; in our case are aluminum and titanium. [4]

2. Experimental procedure

The mechanical homogenization method used in the literature is called Vortex method.[5][6] This method consists of placing a pallet in the molten alloy. The blade rotates with a certain speed of rotation for a period of time designated by the experimental procedure [7].

Designing and making the experiment aimed to highlight the inclusion in different particle size classes of ferroalloy in aluminum metal matrix. So we varied the ferroalloy particle sizes (FeTi32) maintaining constant parameters: temperature, steering rate and chemical composition of particles. In one experiment we varied the mixing time and the mass.

***Table 1.** Experimental data*

No.	Load composition			Ratio Al/FeTi32	Temperature	Mixing time	Steering rate
	Al	FeTi32					
		mass	grain				
	[g]		[mm]	[%]	[^{o}C]	[min.]	[rpm]
1	200	25	0.8	12.5	700	15	170
2	200	50	0.8	25	700	30	170
3	200	50	0.4	25	700	30	170
4	200	50	0.056	25	700	30	170

3. Results and discussions

The mechanical mixing process implies the movement of the particles in liquid aluminum. In the first part of the particle wetting occurs.

If the particles are not wetted by the melt they will not be embedded and will form a distinct phase which comprises partially wetted particles covered with a film of aluminum, particles located on the outside of the melt.

To better observe the behavior of the particle, they were being sorted by rank. Of all the particle size classes, were chosen three classes: 0.8 mm, 0.4 mm, 0.056 mm. These classes are representative particle size covering the entire spectrum of sizes from the finest to the coarsest.

The behavior of particles in contact with molten aluminum to form clusters is increasing this sense of their wetting time.

The behavior of particles in contact with molten aluminum is to form clusters, increasing the wetting time.

The mechanical mixing process is done in the furnace atmosphere that is composed of 78% nitrogen and 21% volume percent, the rest is composed of other gases.

The liquid aluminum contact with air quickly forms a film of Al_2O_3 which also slows the wetting process of assimilation of metal particles in the bath.

Another factor that competes in the dispersion of particles in molten aluminum mass is the mass transport of particles and energy from the molten aluminum and vice versa.

In the case of energy transport there are two phases of different natures, they will have different properties and thermal conductivity.[3]

Table 2. *Thermal conductivity coefficients*

No	Chemical composition	Thermal conductivity
	[%]	[W/m K]
1	Al	237
2	FeTi with 32% Ti	0.6

Therefore after the introduction of molten metal particles, there will be a slight initial decrease in the melting temperature. Aluminum cooling effect will be observed by increasing the dynamic viscosity of aluminum.

Mass transfer occurs by diffusion process between the two phases of liquid aluminum particles FeTi.

The interface matrix - particle diffusion process takes place. But as the mixing process continues over a relatively short distance, diffusion takes place locally. To emphasize the diffusion, we can analyze the chemical composition. For particle sizes of 0.8 mm elaborated at 15 min and 30 minutes are found different chemical compositions.

For the probes obtained, we have the following determinations:

a. Chemical analysis

We use X-rays fluorescence spectrometer (XRF) Innov-x system Alpha Series. The X-ray spectrometer has a 10 mm aperture size which represents the X-ray window and the analysis is done by bombarding the surface with X-rays and their detection on the surface.

Spectrometer computer calculates an average of all points on the sample and gives the result. So the stirring time increases the contact time between aluminum particles and thus increases the interface and surface diffusion.

Table 3. *Chemical composition*

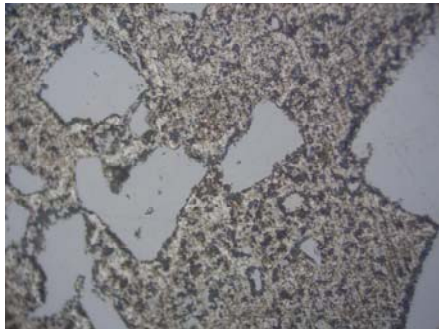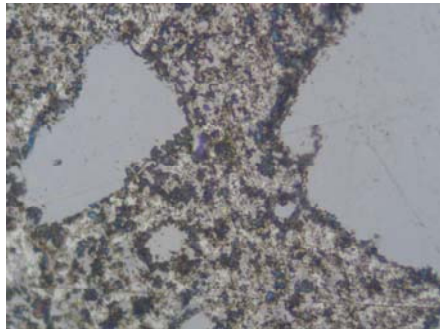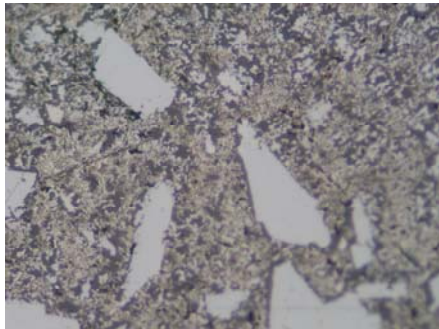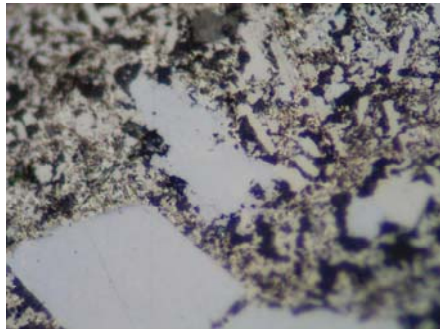| No.	Grain	Chemical analysis		
		Al	Fe	Ti
	[mm]	[%]		
1	0.8	91.22	5.53	3.25
2	0.8	77,51	13,64	8.82
3	0.4	79.36	13.08	7.56
4	0.056	76.71	13.54	9.75

b.Metallographic analysis
For this, we collected samples of the composite material Al/FeTi with 32% Ti and we have prepared it by grinding and by polishing the samples.

Fig. 1. *Microstructures of Al/FeTi32*

No.	Ferroalloy particle diameter, FeTi32	Process time	Microstructures	
			un-attacked	
	[mm]	[min]		
1	0.800	30	X400	X1000
2	0.056	30	X400	X1000

Upon implementation of metallographic analysis we can make the following observations:
- for 0.8 mm particle size:
- good adhesion between matrix and particles;
- at the interface liquid - particle not formed a counter-diffusion zone;
- particles shows the layout predominantly polygonal and they are dispersed in the matrix relatively homogeneous;
- 0.056 mm particle size:
- good adhesion between matrix and particles;
- at higher magnification we see the interface and any casting defects (micro porosity).

Metallographic appearance reveals very different sizes which would lead to the conclusion that it was not finished size ranked the ferroalloys. This would explain the fact that the shape of the particles is what makes platform break is sometimes great, sometimes through the booklet to be slanted and appear almost acicular issues.

Metallographic aspects have sometimes shadows at the particle-matrix interface and that suggests an incorporation of non-compliant but this is because at the processing of samples FeTi32 particles remain slightly raised from the aluminum matrix and the incident rays from lens of the microscope can create this optical illusion.

4. Conclusion

Mechanical mixing is the main factor in obtaining a composite material Al/FeTi32. Mechanical mixing process was done by the literature method called Vortex. Mixing time is to allow each particle to come into contact with liquid aluminum.

Demonstrated by the different chemical composition at 15 min and 30 min. Microscopic analysis showed the appearance of the interface Al/FeTi32. Here he could find that the diffusion zone is very limited.

References

[1]. **I. Tripsa, F. Oprea, I. Dragomir** - B*azele teoretice ale metalurgiei extractive*, Editura Tehnica Bucuresti 1967.
[2]. http://www.shieldalloy.com/table1page.html

[3]. **I.N. Zegalo, Yu. N. Grishchenko, A.P. Stovpchenko, S.I. Zigalo** - *Thermophysical properties of certain ferroalloy and graphite powders.* Powder metallurgy and Metal Ceramics, vol. 35. nos. 1 – 2, 1996.
[4]. **Iosif Tripsa, Constantin Pumnea** Dezoxidarea otelurilor Editura Tehnica 1981**.**
[5]. **Florin Stefanescu, Gigel Neagu, Alexandrina Mihai** – *Materialele viitorului se fabrica azi. Materiale compozite.* Editura Didactica si Pedagogica 1996.
[6]. **Ioan Carcea** – *Materiale compozite. Fenomene la interfata.* 2008
[7]. **Vasile Basliu** - *Development of a new installation of elaboration-casting in order to obtain composite materials with metallic matrix*, Artcast 2010, p.375 – 379.

INVESTIGATION OF ELASTIC CONSTANTS AND MODULI OF BINARY ALLOYS BY STATISTICAL MOMENT METHOD

Thi Hoa NGUYEN

Faculty of Fundamental Science
University of Transport and Communications, Hanoi, Vietnam
email: hoanguyen_1974@yahoo.com

ABSTRACT

The moment method in statistical dynamics is used to study the dynamical elastic constants (C_{11}, C_{12}, C_{44}), Young's modulus (E), bulk modulus (K), and shear modulus (G) of binary alloys. Lattice mechanical properties of disorder alloys are calculated as a function of the temperature. In most cases there is a good agreement between the present and the experiment.

KEYWORDS: Lattice mechanical properties, elastic constants, elastic moduli, binary alloys, statistical moment method

1. Introduction

Elastic deformation is one of the most important considerations in structural applications of solid materials. In recent years, there has been considerable interest in elastic-plastic deformation of materials. Some of these studies are listed in Refs. 1 and 2.

Various theoretical studies have been used to study the dynamical elastic properties of simple metals and alloys. Phonon spectrum and lattice mechanical properties of metals have been calculated using *ab-initio* theory [2, 3]. Recently, a pseudo potential model depending on the effective core radius is used to study the interatomic interactions, dynamical elastic constants (C_{11}, C_{12}, C_{44}) and Young's modulus (E), the behavior of phonon frequencies, etc., for simple metals and alloys [4]. Rare-earth and actinide elements such as La, Yb, Ce, Th... also have been considered by the same method [5].

In this paper we have calculated dynamical elastic constants (C_{11}, C_{12}, C_{44}), Young's modulus (E), bulk modulus (K), and shear modulus (G) by using the statistical moment method (SMM) [6,7]. In Sec. 2, the analytic expressions for elastic moduli (E, K, G) and dynamical elastic constants are given. In Sec. 3, the SMM calculations are performed by using effective pair potentials for Cu-Zn, Cu-Ni, Ni-Cr, Al-Cu, Al-Mg, Pd-Ag…alloys with various concentrations and compared to the experimental results.

2. Theory

2.1. Free energy and the nearest neighbor distance of binary alloy

We consider a binary alloy consisting of two components A and B neglecting vacancies and interstitials with face-centered cubic structure (f.c.c) and body-centered cubic structure (b.c.c). C_A, C_B are the concentration of atoms A, B, respectively. The atoms chosen as base are atom α located in lattice point β. This system is called effective systems (α, β). The free energy of the system may be determined by the combination of the free energy of these effective system (α, β) as:

$$\Psi = \left(\upsilon_a p_A^a \Psi_A^a + \upsilon_b p_A^b \Psi_A^b + \upsilon_a p_B^a \Psi_B^a + \upsilon_b p_B^b \Psi_B^b \right)$$

$$- TS_c \quad = \sum_{\alpha,\beta} \upsilon_\beta p_\alpha^\beta \Psi_\alpha^\beta - TS_c, \quad (1)$$

where υ_a, υ_b the concentration of the lattice points of type a, b. p_α^a, p_α^b (α = A, B) are the probability of atom α located in the lattice points a, b, respectively. Probabilities p_α^β (β = a, b) satisfy the following relations:

$$p_A^a + p_B^a = 1; \; p_A^b + p_B^b = 1; \; \upsilon_a p_A^a + \upsilon_b p_A^b = C_A;$$

$$\upsilon_a p_B^a + \upsilon_b p_B^b = C_B;$$

Ψ_α^β is the free energy of the effective system (α, β) and S_c is the entropy of mixing.

$$S_c = k \ln \left[\frac{(N_A + N_B)!}{N_A! N_B!} \right] \qquad (2)$$

with: k is the Boltzmann constant.

In order to define Ψ_α^β we use the statistical moment method (SMM) described in [6, 7]. The free energy of the effective system (α, β) will have the form of the free energy of the systems of N harmonic oscillator [7]

$$\Psi_\alpha^\beta = 3N \left\{ \frac{u_{o\alpha}^\beta}{6} + \theta \left[x_\alpha^\beta + \ln(1 - e^{-2x_\alpha^\beta}) \right] \right\} \quad (3)$$

with:

$$x_\alpha^\beta = \frac{\hbar \omega_\alpha^\beta}{2\theta} = \frac{\hbar}{2\theta} \sqrt{k_\alpha^\beta / m^*}, \qquad (4)$$

where: $m^* = C_A m_A + C_B m_B$; m_A, m_B are the mass of atoms A and B, and the sum of the effective pair interaction energies of the effective system (α, β), $u_{o\alpha}^\beta$, and the second - order vibrational constant, k_α^β, are given as:

$$u_{o\alpha}^\beta = \sum_i \varphi_{\alpha i}^\beta \left(|a_i| \right)$$

$$k_\alpha^\beta = \frac{1}{2} \sum_i \left(\frac{\partial^2 \varphi_{\alpha i}^\beta}{\partial u_{ix}^2} \right)_{eq} \equiv m^* \left(\omega_\alpha^\beta \right)^2 ; \qquad (5)$$

here: $\varphi_{\alpha i}^\beta (|a_i|)$ is the potential energy of interaction between particle i-th and the base particle, a_i is the vector determining the equilibrium position of particle i, u_i the displacement of i-th particle from its equilibrium position.

In the case of disorder alloys AB, we have [6]:

$$\Psi_A^a = \Psi_A^b = \Psi_A^*, \quad \Psi_B^a = \Psi_B^b = \Psi_B^*, \quad (6)$$

where: Ψ_α^* / N is the free energy of atom α $(\alpha, \alpha' = A, B)$ surrounded by $J_{1\alpha} = n_1 p_{\alpha\alpha'} / C_\alpha$ of

atoms α' and $(n_1 - J_{1\alpha})$ of atoms α on the first coordination sphere and $J_{2\alpha} = n_2 p_\alpha^\beta, = n_2 C_{\alpha'}$ of atoms α' (and $(n_2 - J_{2\alpha})$ of atoms α on the second coordination sphere; n_1, n_2 is the number of the atoms on the first and second spheres.

Then, we can find the expression of the free energy of disorder alloy with $C_B \ll C_A$:

$$\Psi_{AB} \approx C_A \Psi_A + C_B \Psi_B - TS_c, \qquad (7)$$

where: ψ_α is the free energy of the effective metal α.

In order to define the nearest neighbor distance, we can use some different ways. In this paper, the nearest neighbor distance is determined by minimizing the free energy with respect to the volume of the system and we obtain the expression of the nearest neighbor distance of disorder binary alloy [8]:

$$a \cong C_A a_A \frac{B_{T,A}}{\overline{B_T}} + C_B a_B \frac{B_{T,B}}{\overline{B_T}} \qquad (8)$$

where:
$$\overline{B_T} = C_A B_{T,A} + C_B B_{T,B},$$

$$B_{T,\alpha} = \left(\frac{\partial^2 \Psi_\alpha}{\partial a_\alpha^2} \right)_{T,p,N}$$

$$= \frac{1}{2} \left(\frac{\partial^2 u_{o\alpha}}{\partial a_\alpha^2} \right)_{T,p,N} +$$

$$\frac{3\hbar \omega_\alpha}{4k_\alpha} \left[\left(\frac{\partial^2 k_\alpha}{\partial a^2} \right)_{T,p,N} - \frac{1}{2k_\alpha} \left(\frac{\partial k_\alpha}{\partial a} \right)_{T,p,N}^2 \right],$$

$$(9)$$

with: a_α is the nearest neighbor distance at temperature T of the effective metal α.

2.2. Dynamical elastic constants and moduli

If Ψ_{AB} is the Helmholtz free energy for a volume element of the considered system in the case without external force p, Ψ_{AB}^P is the one in the case of external force P, ε is the elastic strain, σ is the stress, the relation of these quantities can be written in the approximation form [9]:

$$\Psi_{AB}^P = \Psi_{AB} + \frac{E \varepsilon^2}{2} . \qquad (10)$$

In the above expression, the term $\dfrac{E\,\varepsilon^2}{2}$ is the deformation energy for a volume element of the system, E is the Young's modulus.

From the definition of the elastic strain ε, we have:

$$\varepsilon = \frac{\Delta a_{AB}}{a_{AB}} = \frac{a_{AB}^P - a_{AB}}{a_{AB}} \qquad (11)$$

here: a_{AB}, a_{AB}^P is the nearest neighbor distance of the system in the case without and with external force P, respectively, and has the form

$$a_{AB} = a_{0AB} + y_0 \,, \quad a_{AB}^P = a_{0AB}^P + y \,, \qquad (12)$$

where: a_{0AB} and a_{0AB}^P is the nearest neighbor distance of the system in the case without external force P and in the case of external force P at zero temperature, respectively; y is the displacement of atom in the case of external force P [7]

$$y = y_0 + A_{1AB}\,P + A_{2AB}\,P^2 \qquad (13)$$

here: y_0 is the displacement of atom in the case without external force P.

In the case of elastic deformation, when $\Delta a_{0AB} = a_{0AB}^P - a_{0AB} \approx 0$, from Eq. (11), (12) and (13), we have:

$$\varepsilon \approx \frac{y - y_0}{a_{AB}} \approx \frac{y_0 + A_{1AB}P - y_0}{a_{AB}} = \frac{A_{1AB}P}{a_{AB}} \,. \qquad (14)$$

Using the relation of the stress σ and the strain ε for the Hookean deformation, so we have $\dfrac{\partial \sigma}{\partial \varepsilon} = E$, and Eqs. (10) and (14), we obtain the expression of the Young's modulus E:

$$E = \frac{\sigma a_{AB}}{A_{1AB}P} = \frac{1}{\pi a_{AB} A_{1AB}} \,. \qquad (15)$$

Because a_{AB} and A_{1AB} depend on temperature [8], so Eq. (15) is the expression of the Young's modulus at various temperatures.

Using the relation of the Young's modulus E with bulk modulus K and shear modulus G [10], we obtain the analytic expressions for elastic moduli:

$$K \approx \frac{E}{3(1-2\upsilon)} \,, \quad G = \frac{E}{2(1+\upsilon)} \qquad (16)$$

with υ is the Poisson's ratio.

It is known that for cubic crystals, the elastic constants are [11]

$$C_{11} = \frac{E(1-\upsilon)}{(1+\upsilon)(1-2\upsilon)} \,,$$

$$C_{12} = \frac{E\upsilon}{(1+\upsilon)(1-2\upsilon)} \,, \quad C_{44} = \frac{E}{2(1+\upsilon)} \,. \qquad (17)$$

3. Results and discussion

In order to check the validity of the analytical expressions of the elastic properties of the metallic systems described herein, we performed calculations for some disorder binary alloys. For simplicity, we take the effective pair interaction potential in the systems as the power law, similar to the Lennard-Jones pair interaction potential:

$$\varphi(r) = \frac{D}{n-m}\left[m\left(\frac{r_0}{r}\right)^n - n\left(\frac{r_0}{r}\right)^m \right], \quad (18)$$

where the potential parameters such as D and r_0 are determined to fit experimental data (e.g., cohesive energy and elastic modulus). Using the experimental data of the potential parameters D, r_0 and the Poisson's ratio υ (Tab. 1) and the expressions obtained in Sec. 2, we calculated the values of the elastic constants and moduli at temperature T and the zero pressure for Cu-Zn, Cu-Ni, Al-Cu,… alloys with various concentrations. The calculated results are presented in Tabs. 2-5.

In Tab. 2, we show the calculated values of the nearest neighbor distance a_{AB} of Fe_xCu_{1-x} alloys at 0K. In Tabs.3 and 4, we show our calculated and experimental results of the elastic moduli at various temperatures. The accuracy of the elastic moduli is remarkably good. The elastic moduli of Pd-80Ag (at T=293K) and Al-4.5Cu (at T=300K) alloys are in excellent agreement with the experimental results.

Using Eqs. (17), we calculate the values of the elastic constants at temperature T and zero pressure for Ag-Mg, Ag-Pd, Cu-Zn, … alloys. Our calculated and experimental results of C_{11} at 300K are presented in Tab. 5. The present SMM calculations of the elastic constants agree well with the experimental values. All of the case are in excellent agreement with the experimental results, within ~0.9% for Ag-7.33Mg, Cu-4.59 Zn,… alloys.

The decrease of the elastic moduli and constants with increasing temperature arises from the thermal lattice expansion and the inharmonic effects of the vibrational. These results are presented in Fig. 1 and Fig. 2. The SMM calculations are performed by using the effective pair potential for Cu-Zn, Cu-Ni, Ni-Cr, Al-Cu, Al-Mg, Pd-Ag… alloys. In general, we have obtained good agreement in the elastic constants and moduli between our theoretical calculations and experimental values.

Tab.1. *Potential parameters D, r_o, m, n and the Poisson's ratio υ determined by the experiment [12]*

Metals	m	n	r_0 (A^o)	D (10^{-16} erg)	υ
Ag	5.5	11.5	2.8760	4589.328	0.38
Al	5.5	11.0	2.8541	4133.928	0.34
Ni	8.0	9.0	2.4780	5971.536	0.30
Cu	5.5	11.0	2.5487	4693.518	0.37
Pt	5.0	9.2	2.7689	9914.196	0.40
Pd	5.0	9.0	2.7432	7559.778	0.38
Ir	5.0	11.0	2.8847	11750.148	0.26
Fe	7.0	11.5	2.4775	6416.448	0.26
Mg	4.5	14.0	3.1882	2069.034	0.30
Zn	5.5	10.0	2.7622	2320.47	0.35
Cr	6.0	15.5	2.4950	6612.960	0.33

Tab.2. *SMM calculations of the nearest neighbor distance a_{AB} of Fe_xCu_{1-x} alloys at 0K and ab-initio results [13]*

		Fe-10.0Cu	Fe-25.0Cu	Cu-25.0Fe
a_{AB}(A^0)	SMM	2.404	2.410	2.458
	ab-initio	2.494	2.494	2.490

Tab.3. *SMM calculations and Expt. results of Young's modulus E (in 10^{10} Pa) at T=586K for alloys*

Alloys	Cu-5.0Zn	Cu-10.0Zn	Cu-20.0Zn	Cu-30.0Ni	Ni-20.0Cr
SMM	11.11	10.71	9.92	13.81	20.00
Expt. [14]	11.70	11.70	11.00	15.20	21.00

Tab.4. *SMM calculations and Expt. results of Young's modulus E (in 10^{10} Pa) at T=293K, T=300K for alloys (Expt.^{a} [12]; Expt.^{b} [14])*

		T= 293^{0}K		T=300^{0}K			
	Alloys	Pd-80.0Ag	Pt-10.0Ir	Al-4.5Cu	Al-3.8Mg	Al-8.0Mg	Al-10.0Mg
E	SMM	9.0	16.6	7.26	6.82	6.59	6.48
	Expt.	9.0^a	15.0^a	7.10^b	7.10^b	7.10^b	7.10^b
G	SMM			2.67	2.51	2.42	2.38
	Expt.			2.65^b	2.65^b	2.65^b	2.65^b

Tab.5. *SMM calculations and Expt. results of elastic constant C_{11} (in 10^{11} Pa) at T=300K for alloys (Expt. [14])*

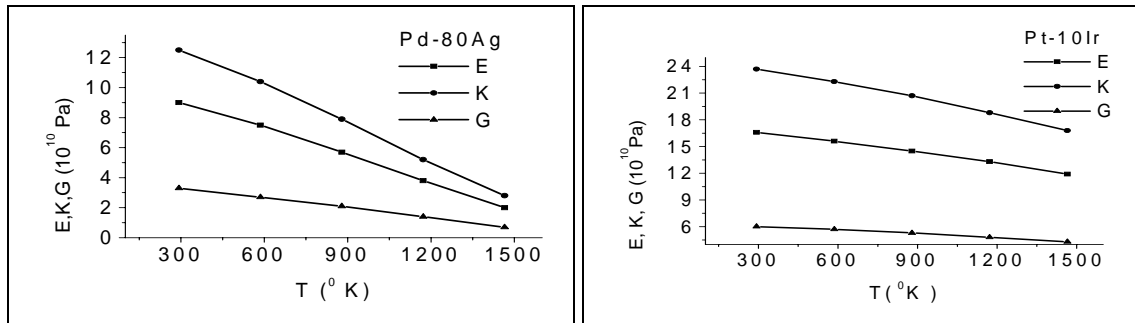| Alloys	Ag-3.07Mg	Ag-7.33Mg	Ag-6.22Pd	Ag-2.4Zn	Ag-3.53Zn
SMM	1.209	1.162	1.296	1.222	1.211
Expt.	1.198	1.159	1.277	1.209	1.230
Alloys	Cu-4.1Zn	Cu-4.59Zn	Cu-9.1Zn	Cu-17.1Zn	Cu-4.81Al
SMM	1.651	1.644	1.587	1.482	1.678
Expt.	1.633	1.634	1.571	1.499	1.658

Fig. 1. *The dependence of the Elastic moduli on the temperatures*
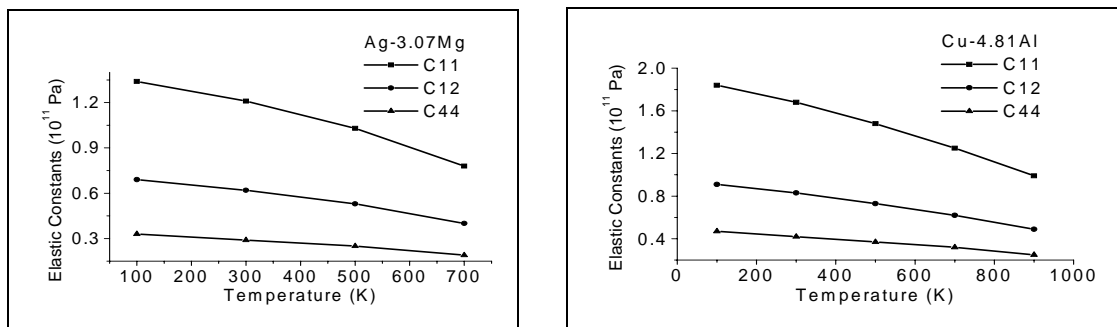*for Pd-80Ag and Pt-10Ir alloys*

Fig. 2. *The dependence of the Elastic constants on the temperatures for*
Ag-3.07Mg and Cu-4.81Al alloys

References

[1]. V. Heine et al. - *Solid state physics* (Academic Press, NY), 24 (1970).

[2]. R. E. Cohen, M. J. Mehl, and D.A. Papaconstantopoulos - *Phys. Rev*. B50, 14694 (1994).

[3]. M.J. Mehl and D.A. Papaconstantopoulos, *Phys. Rev*. B54, 4519 (1996).

[4]. W. A. Harrison - *Pseudopotential in the theory of metals* (W.A. Benjamin, Inc., New York, 1966).

[5]. J.K. Baria and A. R. Jani - *Pramana-J. Phys*. Vol.60, No.6, 1235 (2003).

[6]. Tang N., Tam P. D. and Hung V. V.- *Comm. in Phys*, 7(3), 47 (1997).

[7]. Tang N. and Hung V. V.,- *Phys. Stat. Sol* (b), 149, 511(1988); 161, 165(1990); 162, 371(1990).

[8]. Nguyen Van Quang - Master Thesis, *HUE*., (1997).

[9].V. V. Hung and P. T. M. Hanh - *J. Sci. HUE*., 1, 40 (2002).

[10]. Hung V.V., Hai N. T.- *Comp. Mater. Sci*., 14, pp. 261-266 (1999).

[11]. L.V. Tikhonov, V.A. Kononenko, G.I. Prokopenko, V.A. Raphalovxki. - *Mechanical properties of metals and alloys*, Kiev Naukova Dumka (1986) (in Russian).

[12]. Mazomendov M. N J. - Fiz. *Khimic*, 61, 1003 (1987).

[13]. Gong. H. R. et al. - *Phys. Rev*., B 69, 054203 (2004).

[14]. Dwight E. Gray. - *American Institute of Physics Handbook*, 2nd Ed., McGraw-Hill book Company, New York Toronto London (1961).

MANUSCRISELE, CĂRŢILE ŞI REVISTELE PENTRU SCHIMB, PRECUM ŞI ORICE CORESPONDENŢE SE VOR TRIMITE PE ADRESA:

MANUSCRIPTS, REVIEWS AND BOOKS FOR EXCHANGE COOPERATION, AS WELL AS ANY CORRESPONDANCE WILL BE MAILED TO:

LES MANUSCRIPTS, LES REVUES ET LES LIVRES POUR L'ECHANGE, TOUT AUSSI QUE LA CORRESPONDANCE SERONT ENVOYES A L'ADRESSE:

MANUSCKRIPTEN, ZIETSCHRITFTEN UND BUCHER FUR AUSTAUCH SOWIE DIE KORRESPONDENZ SID AN FOLGENDE ANSCHRIFT ZU SEDEN:

After the latest evaluation of the journals achieved by National Center for the Science and Scientometry Politics (**CENAPOSS**), as recognition of its quality and impact at national level, the journal is included in B^+ category, 215 code (http://www.cncsis.ro/2006_evaluare_rev.php).
The journal is indexed in Cambridge Scientific Abstract
http://www.cncsis.ro/userfiles/file/CENAPOSS/B+feb_2011(9).pdf
The papers published in this journal can be visualized on the "Dunarea de Jos" University of Galati site, the Faculty of Metallurgy, Material Science and Environment, page: www.fmsm.ugal.ro.

AFFILIATED WITH:

- *ROMANIAN SOCIETY FOR METALLURGY*
- *ROMANIAN SOCIETY FOR CHEMISTRY*
- *ROMANIAN SOCIETY FOR BIOMATERIALS*
- *ROMANIAN TECHNICAL FOUNDRY SOCIETY*
- *THE MATERIALS INFORMATION SOCIETY (ASM INTERNATIONAL)*

Annual subscription (4 issues per year)

**Edited under the care of
Faculty of
METALLURGY, MATERIALS SCIENCE AND
ENVIRONMENT**

Edited date: 30.03.2011
Issues number: 200
Printed by
Galati University Press
accredited CNCSIS
47 Domneasc Street, 800036
Galati, Romania